Università degli Studi di Napoli “Federico II”

SCUOLA POLITECNICA E DELLE SCIENZE DI BASE
DIPARTIMENTO DI INGEGNERIA INDUSTRIALE

TESI DI LAUREA IN INGEGNERIA AEROSPAZIALE

CLASSE DELLE LAUREE MAGISTRALI IN INGEGNERIA AEROSPAZIALE E ASTRONAUTICA
(LM 20)

Aerodynamic characterization of a commuter seaplane through wind tunnel testing

Relatore:
Prof. Fabrizio Nicolosi

Correlatori:
Prof. Pierluigi Della Vecchia
Ing. Gennaro Zolfo

Candidati:
Andrea Pezzulo
Matr. M53001892
Italo Tartaglione
Matr. M53001863

ANNO ACCADEMICO 2024 – 2025

Abstract

This thesis presents a comprehensive experimental campaign aimed at evaluating the aerodynamic performance and stability characteristics of an innovative seaplane design. Aerodynamic testing was conducted in the University of Naples "Federico II" subsonic wind tunnel facility, by means of a sophisticated six-component strain-gauge balance. A significant portion of the work is focused on the experimental setup and the data acquisition process. This includes a rigorous calibration and taring procedure to account for weight and interference effects. The raw data underwent extensive post-processing, involving scaling and wall interference corrections. The experimental campaign allowed the determination of the aerodynamic coefficients and the extraction of critical longitudinal and lateral-directional stability and control derivatives. The results demonstrate the aerodynamic viability of the proposed design and provide a high-fidelity database for future flight dynamics modeling and advanced numerical simulations.

Contents

List of Figures

List of Tables

Chapter 1

Introduction

The work presented in this thesis is a critical part of the complex experimental campaign required for the successful design and development of an aircraft, specifically a seaplane. This research focuses on the aerodynamic characterization of a seaplane within the framework of the "Colossus" project carried out through wind tunnel testing. The study includes an overview of the specific category of seaplanes, the main objectives of the project and facility, model and instrumentation characteristics. Furthermore, data treatment methodologies and test setup, as well as evaluation of the results and future developments are analyzed.

1.1 Features of a seaplane

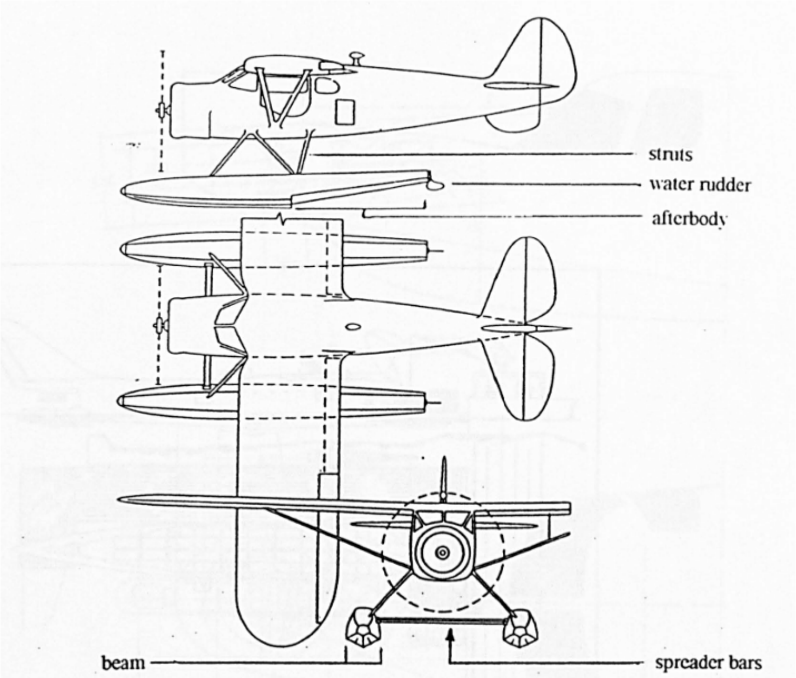

Figure 1.1: *Floatplane terminology*

Seaplanes represent a particular kind of aircraft, suitable for take-off and landing on water. This ability identifies at least four types of seaplane, as mentioned in [8]:

- Floatplanes
- Amphibious floatplanes

- Flyingboats
- Amphibious flyingboats

The floatplane is a kind of aircraft which is only capable of landing on and taking-off from the water surface, granting its buoyancy with discrete floats. A flyingboat on the other hand, derives its flotation from a hydrodynamic fuselage, which serves as a hull during water maneuvers. Amphibious types, from greek ἀμϕίβιος (literally "dual life"), are additionally able to operate on land, expanding the suitable operational scenarios but with a higher empty weight due to the simultaneous mounting of landing gears and floats, the latter also increasing parasite drag compared to the first.

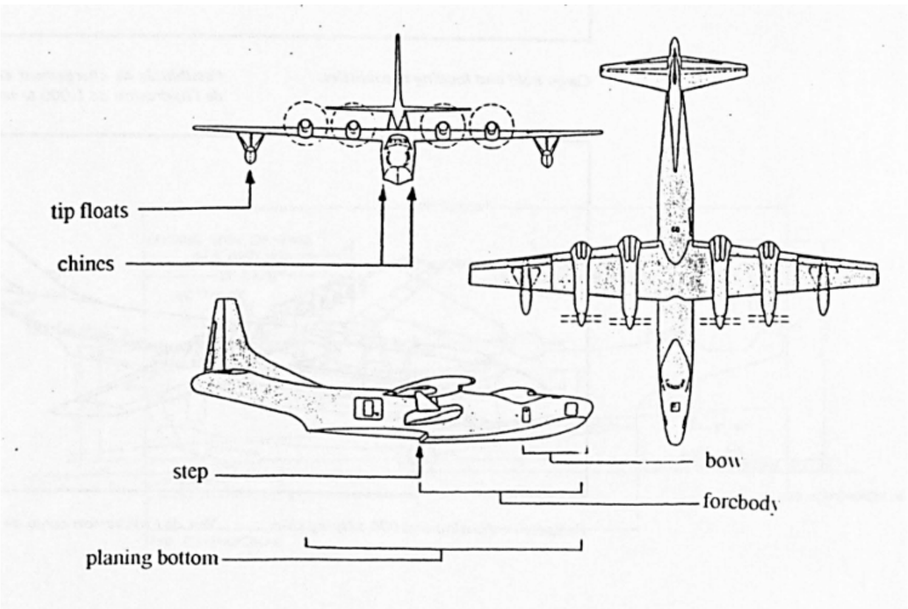

Figure 1.2: *Flyingboat terminology*

This section mainly focuses on the amphibious flyingboat configuration. The fields of application are remarkable as flyingboats are suited for:

- **Military operations**: a demanding sector, which requires promptness of deployment, with the highest aerodynamic, hydrodynamic, structural and propulsive performance. This is related to the dangerous situations in which the aircraft is involved, as transportation of heavy payloads or search and rescue operations in complex scenarios.
- **Commercial transportation**: operating as a commercial aircraft, a flyingboat is able to expand the list of available routes, allowing fast and direct connections to locations with geographical constraints for the construction of airports, or minimizing the distance from/to the airport. Safety and environmental factors such as noise reduction, protection of the local flora and fauna and pollution have to be considered

while outlining project feasibility, as well as water-linked maintenance costs and increased fuel consumption due to drag.

- **Aerial firefighting**: one of the most notorious applications for this kind of aircraft, it contributes to safety during firefighting operations. A flyingboat discharges water or foams directly onto fire zones from above, with the ability to intervene even in inner areas of wildfires where ground operations would be impossible. The main advantage, when compared to a standard aircraft, is the scooping, the high-speed water loading while hydroplaning on its surface, without the need to land, greatly reducing turnaround time. Since helicopters are also available for the purpose, the seaplane design focuses on larger storing volumes, higher range and speed to increase flow rate.

The aircraft design clearly depends on many factors, for example the topology of the territory on which it operates. Two firefighting seaplanes can be considered: the notorious Canadair CL-415 and the Beriev Be-200. The first is propeller powered, and one of the main reasons is the proximity of water basins to the areas most affected by fires, which allow limited dash speed; the latter, active in Russia, has to cover larger distances during firefighting operations, and jet engines are required to grant a competitive turnaround time.

Figure 1.3: *Canadair CL415, operative within the Italian Firefighters Department*

The overall design is dictated by a challenging compromise between aerodynamics and hydrodynamics. At equal speed, air and water behave very differently, mainly because of their density and viscosity. In fact, at 20°C, water is almost a thousand times denser and a hundred times more viscous than air, leading to a Reynolds number at least an order of magnitude higher in water. Furthermore, the Froude number[1] is particularly relevant in water as the fluid density is higher and gravitational effects are not negligible. This non-dimensional number is strongly related to wave drag (not shock-waves), a form of resistance generating from the energy spent to displace vertically a fluid, which is clearly large in water, especially during operations as a displacement craft, whereas in classical aviation problems is negligible due to the lack of a free surface. The structural integrity of the flyingboat also requires particular attention, since the wings and fuselage encounter significant stresses when impacting with water, because of the great forces involved.

Furthermore, the whole aircraft architecture is designed to avoid spray: the engines are high-mounted to avoid water ingestion which would corrode internal surfaces and alter the thermodynamic cycle; just like the propellers, control surfaces are positioned as far from water as possible, since high-speed spray can erode the materials and damage moving components.

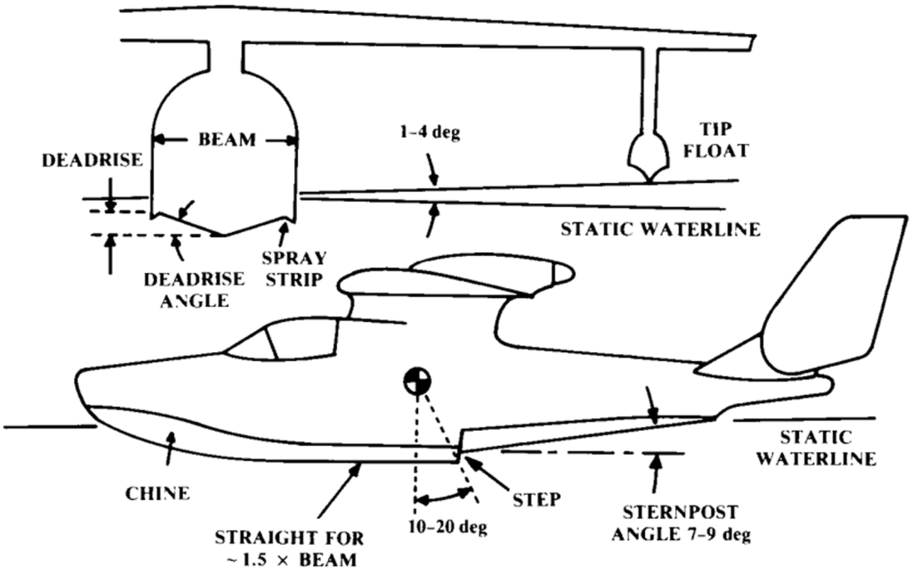

Figure 1.4: *Design features of a flyingboat*

The lower part of the fuselage is designed as a hull, implementing many nautical features. The deadrise angle, for example, is the angle between the hull surface and the horizontal, measured in front view, critical to manage landing and impacts of waves as well as effectively displace water and ensure flotation. The chine is a sharp edge located laterally between the hull and the upper fuselage, which has the same function as the step, a transverse discontinuity. These edges avoid the suction effect due to high-speed water moving along the fuselage, which would increase the lift required to take-off. The sharp edge presents a very small curvature and large velocity gradients would be required to follow it, so water, which does not have sufficient energy close to the surface, separates,

---

[1] $Fr = \frac{V}{\sqrt{gL}}$, where V is the flow velocity, g is the gravitational acceleration and L is the characteristic length of the body

avoiding low pressure peaks and allowing air to infiltrate the gap and ventilate the area, reducing drag. Additionally, the step is effectively positioned close to the center of gravity to improve pitch control during planing, limiting the interactions with water to the forward portion of the hull where the changes in moment are more controllable due to smaller arms. These hydrodynamic solutions have some drawbacks when the aircraft is completely detached from water, since also air is not able to follow these edges and separation occurs, increasing drag during flight. The sternpost angle is needed to grant the required take-off performance: low values would cause a pitch-down tendency due to water pressure and physically prevent rotation while also increasing drag, whereas high values would cause excessive separation during flight, and possibly porpoising while landing due to the lack of an aft contact point on the hull. The bow angle and chines are critical features to increase water penetration abilities of the seaplane, but care should be taken when designing this section, since it integrates the nose which is of uttermost importance for flow control and drag reduction during flight. To grant lateral stability on water, a pair of floats can be implemented under the wing, which are useful to limit the rolling motion of the aircraft due to waves or weight shifts. Their structure has to be carefully designed to transfer both static and dynamic loads through the struts to the wing without damaging it, while being hydrodynamic during landing and take-off. Floats present a sternpost angle, useful to avoid the aft part touching water during pitch-up due to the elevator, which would increase drag and take-off distance. Materials can not be left aside when designing an aircraft that has to operate largely on water. As in standard aviation, metals are a known and solid technology, with predictable isotropic characteristics, opposing to composite materials as carbon, glass or aramid fibers, which require larger design margins and have more complex mechanical properties. On the other hand, composites allow easier production of intricate shapes, need less fasteners, minimizing water leakage, are lighter and can be customized for the specific application. Metals have to be subjected to anodizing to avoid corrosion and must undergo frequent maintenance to preserve the structure, whereas resins can be damaged by UV exposure and non-destructive testing is necessary to verify their integrity and bonding.

1.2 Colossus Project

The **Colossus** (Collaborative SoS Exploration of Aviation Products, Services and Business Models) is a European research project which aims to develop innovative approaches for the design of new products and services in the aviation industry. The activity is included in the Horizon Europe program which promotes solutions to achieve climate neutrality, encouraging sustainable air mobility. Colossus project implements a framework with "System of systems" logic, in which the design is not limited to the product but extends its boundaries to the whole environment related to the aircraft, including the business model and optimization of the operations. This holistic approach is implemented for the design of a multi-role seaplane suitable for both passenger transport and firefighting purposes. The idea is to achieve the highest level of commonality between the two configurations while maintaining the required performance to accomplish the designed missions. The **System of systems** is defined as a traditional system, however, its elements consist of different systems, characterized by independence in management, operations, development and distribution[19]. This innovative concept allows the integration of the aircraft with the environment, simulating the operational scenario in which it is involved, considering fleet, infrastructure and business model. The design of the aircraft is performed simultaneously with the optimization of the operational concept, obtainable by the heterogeneity of the population within the environment: stakeholders, fleets, passengers and infrastructures. The connection and integration of different domains denotes the highly multi-disciplinary spirit of the framework. The design of the aircraft is performed operating in two main scenarios:

- **Sustainable inter-modal mobility**;
- **Aerial wildfire fighting**.

These are used for the definition of the initial requirements and the optimization of the operations parameters and fleet number. The first involves the introduction of aircraft transport in regional and European routes, with the integration of innovative systems for sustainable mobility. Specific routes are selected for the definition of the mission requirements, like the areas of the Baltic and Aegean sea and Balearic islands. The second involves rapid response for fire containment in complex forest environments, as Greece and the Pyrenees. The two scenarios are interacting through an optimization loop based on two fundamental features:

1. **Agent based simulations**: the fundamental methodology that enables the evaluation of the effectiveness. The simulation involves the interaction between multiple "agents", representing aircraft, passengers or wildfire clusters, evaluating the effect produced by their integration in the environment. This methodology allows the definition of optimal fleet solutions for proposed operations and defines design parameters for the aircraft based on the requirements of the scenario. Agent based simulation is operated both for sustainable air mobility and wildfire fighting. For the first case, the simulation integrates the aircraft and the passengers, simulating routes and developing operational strategies. The firefighting simulation involves the modeling of wildfire clusters and their propagation, simulating the seaplane operation and firefighting strategy for the determination of the aircraft requirements necessary for mission accomplishment;

2. **Product Push/Pull paradigms**: the idea is to operate in the two scenarios through different concepts: a "product push" approach for inter-modal air mobility and a "product pull" for firefighting. With the first, a number of aircraft configurations are proposed and "pushed" in the simulation, evaluating the one with best performance and individuating the optimal strategy to operate them in the environment, defining ticket prices, fleet number and best routes. For the "product pull" paradigm, the aircraft requirements are defined within the design space by analyzing the scenario and operational needs. The two paradigms are linked within the design cycle: the first defines the design space for the pull paradigm, which on the other hand defines the requirements necessary for the generation of aircraft configurations in the following loop. The final "Top Level Aircraft Requirements (TLARs)" defined in the optimization loop are presented in table 1.1

	Value
MTOM (Cs.23)	8618 *kg*
Payload	1592 *kg*
Take-off distance	564 *m*
Cruise speed (TAS)	296 *km/h* at 3048 *m* altitude
Ceiling	7620 *m*
Block Range	350 *km* at max payload
N.pax	18
Capacity	2732 *l*

Table 1.1: *Colossus seaplane Top Level Aircraft Requirements*

The features previously described allow the development of a product capable of operating in different scenarios, integrating innovative technologies for sustainable flight, such as hybrid powertrain like electric-turboprop and piston-electric, achieving the reduction of the emissions. The holistic approach integrated with simulations achieved a high level of commonality between the configurations related to inter-modal mobility and firefighting. The seaplane baseline characteristics are presented in table 1.2:

	Value
MTOM	5992.70 kg
Payload	1730.40 kg
Length	14.6 m
Wing span	19.0m
Wing surface	40 m^2
Propulsion	Electric + reciprocating Electric + turboprop
N.pax	18
Capacity	2732 l

Table 1.2: *Colossus baseline characteristics*

1.3 Purpose of the work

The very first objective of wind tunnel testing is the study of the aerodynamic behaviour of a scaled vehicle within a controlled environment, with easier measurement methods compared to real conditions. The aerodynamic characterization of the proposed seaplane is the main purpose of the work, including the assessment of longitudinal and lateral-directional stability and control performances. As an aircraft undergoes many different conditions during a typical flight envelope, fundamental quantities are necessary to evaluate if the design is adequate to the mission profile. This is even more critical when the same seaplane has to comply to such diverse purposes, requiring accurate trade-offs for each feature. First, the aerodynamic coefficients are determined, such as those of lift (C_L), drag (C_D), sideforce (C_Y), pitching moment ($C_{\mathcal{M}}$), yawing moment ($C_{\mathcal{N}}$), and rolling moment ($C_{\mathcal{L}}$). These are extracted for three main points of the flight envelope: take-off, cruise, and landing. A breakdown of the contribution of the various elements of the aircraft has to be carried out to investigate the effectiveness of specific components on these aspects as well as on the critical longitudinal and lateral-directional stability and control derivatives. As will be thoroughly explained in Chapter 3, the latter can be even more significant since, while the coefficients must undergo corrections due to the different circumstances compared to the real flight scenario, derivatives show trends, which are critical for the engineering practice of aircraft design and are usually not affected as much by testing conditions. These quantities are not only indices of the tendencies of the aircraft subjected to testing, but are also of utmost importance for the creation of a high-fidelity database for the correlation with flight tests, the modeling of its dynamic response to external outputs and control law development, as well as, paired with flow visualization data, the validation of aerodynamic modeling methodologies, from lifting line theory to RANS.

Chapter 2

Experimental setup

The wind tunnel test campaign is carried out in the Federico II University facility, based in Naples. This chapter presents the specifics of the facility, the characteristics of the scaled model and the measuring device, a six-component balance. The integration of these elements constitutes the framework through which data have been extracted and analyzed.

2.1 Wind tunnel facility of the University of Naples "Federico II"

Figure 2.1: *The wind tunnel facility at the Aircraft Design Laboratory*

The low turbulence subsonic wind tunnel is a closed loop, closed test chamber wind tunnel, with a maximum speed of 50 m/s.

Test section width (B)	2 m
Test section height (H)	1.4 m
Turbulence level	0.1 %
Maximum Reynolds Number per unit length (Re)	3 mil

Table 2.1: *Wind tunnel characteristics*

Among the others, the wind tunnel supports bi-dimensional tests, with surface and wake pressure distribution and the possibility of wall blowing to reduce the effect of the wall boundary layer, and three-dimensional tests with models of maximum 1.7 m span, in which pressure and forces are measured with pressure ports and balances. Tests on semi-models can also be carried-out to increase the Reynolds number; in this case the model is mounted on a wall support and balances are installed for force measurements. Other applications like oil, tufts and smoke visualization as well as PIV are supported. The low turbulence level is reached by a combination of multiple features to suppress fluctuations in the flow during the test activity:

- High contraction-ratio: helps reducing turbulence intensity and aligns the flow;
- Nets and honeycomb screens: decrease the longitudinal, transverse and vertical velocity fluctuations in the settling chamber;
- Corner turning vanes: reduce the pressure losses during turns around corners;
- Large settling chamber: maximizes the contraction ratio and limits the pressure losses.

These characteristics lead to high quality flow during tests, ensuring the turbulence intensity of 0.1%. The Federico II facility carried out different test campaigns for general aviation aircraft and TECNAM airplanes, but also for the business jet Piaggio P1XX and various non-aeronautical models, such as sails, wind turbines and race cars.

The accuracy of the wind tunnel measurement is also achieved by a refined measurement of the dynamic pressure in the test chamber thanks to the pressure loss calibration procedure. The dynamic pressure, in fact, is measured through a **Venturi channel**, in which the static pressure difference between the settling chamber (high pressure) and the test section (low pressure) is measured.

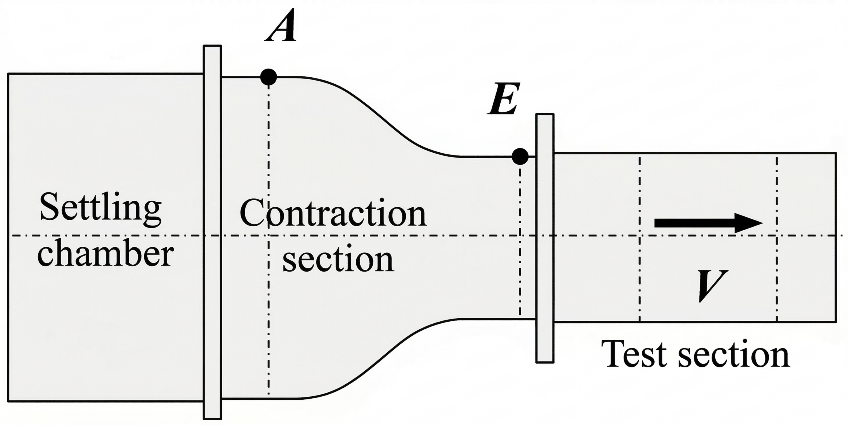

Figure 2.2: *Wind Tunnel calibration*

The calibration is necessary to estimate the pressure losses between the settling chamber and the test section, which would lead to a wrong measurement of the dynamic pressure acting on the model. The total pressure P_{0A} in the settling chamber is, for the continuity, equal to the total pressure P_{0E} in the test chamber plus the pressure losses:

$$P_{0A} = P_{0E} + (P_{0A} - P_{0E}) = p_E + q_E + (P_{0A} - P_{0E}) \tag{2.1}$$

Where in the settling chamber the dynamic pressure is zero. The **Pressure loss coefficient** can be expressed as:

$$C_1 = \frac{P_{0A} - P_{0E}}{q_E} \tag{2.2}$$

The equation (2.1) can be written as:

$$p_A - p_E = q_E + C_1 q_E - q_A \tag{2.3}$$

Then according to the continuity equation, that is

$$\rho_A V_A A_A = \rho_E V_E A_E \tag{2.4}$$

and assuming incompressible flow, hence ρ is constant, then squaring the previous equation and multiplying by $\frac{1}{2\rho}$, one gets:

$$q_A A_A^2 = q_E A_E^2 \tag{2.5}$$

It is possible to define the constant C_2:

$$C_2 = \left(\frac{A_E}{A_A}\right)^2 \tag{2.6}$$

finally obtaining :

$$p_A - p_E = (1 + C_1 - C_2)q_E = Cq_E \tag{2.7}$$

The constant C is derived by calibration and C_2 is calculated by measuring the cross sectional area of the settling chamber and the test section; the constant C_1 is then evaluated. The constant $k = \frac{1}{C}$ is called **Wind tunnel calibration constant** and is derived by plotting the pressure difference between the two sections versus the related dynamic pressure at different speeds in the empty test chamber. After interpolating the data, the curve slope k can be extracted.

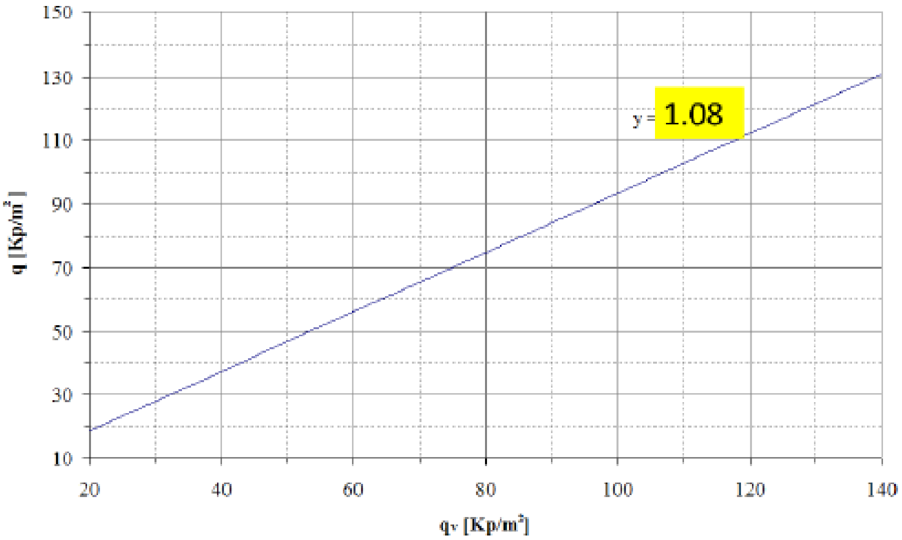

Figure 2.3: Wind tunnel calibration constant determination

The C coefficient for the Federico II wind tunnel is 0.92 and, knowing the cross sectional dimensions, C_2 and C_1 can be evaluated:

Test section area (A_E)	2.67 m^2
Settling chamber area (A_A)	7.84 m^2
Area constant (C_2)	0.116
Pressure loss coefficient (C_1)	0.035

Table 2.2: Wind tunnel calibration constants

2.2 Colossus test model

The study was performed using a **scaled model** (1:11.86), manufactured in **aluminum**, with a total length of 1.3 m, a wingspan of 1.6 m and a height of 0.4 m, from the bottom of the fuselage to the tip of the tail. The model is made of different parts that can be assembled to support the various tests in the wind tunnel: the wing and flaps, the fuselage, a T-tail, divided into horizontal and vertical stabilizers with their respective control surfaces, as well as two floats with their struts, 3D printed using PLA. Inside the fuselage, directly under the wing, there is an opening for the six-component balance and the sting which have been used to support the model and acquire forces and moments.

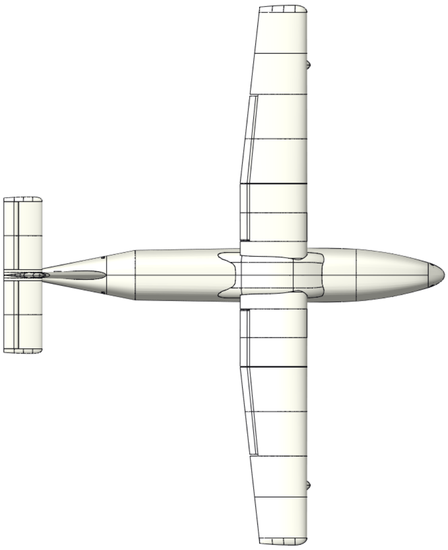

Figure 2.4: *Top view*

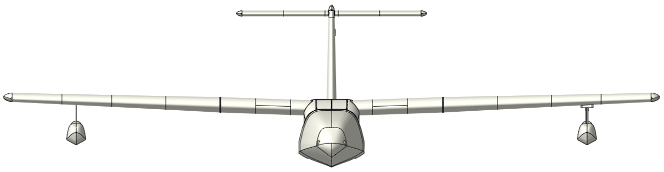

Figure 2.5: *Front view*

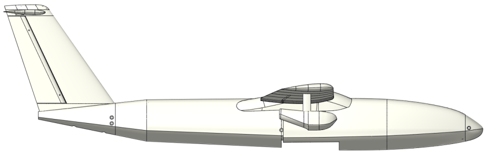

Figure 2.6: *Side view*

As illustrated in Fig. 2.7, the model encompasses multiple components. The fuselage has been machined as two symmetric **shells**, a choice that reduces weight and facilitates the assembly process. The **nose cone** is mounted on the fore, and the **tail cone** supports the stabilizers. An aluminum **interface plate** is positioned between the two shells, serving as a mounting point for both the wing and the **internal balance**. Below the first, a second steel plate connects directly to it, ensuring the adaptability of the model to different measurement systems. Above the plates, one last component allows the **left and right wings** to be mounted on the fuselage with the correct dihedral, and a 3D printed fairing is installed to reduce the interference drag. Each flap is linked to the wing through two small interchangeable brackets, as all the control surfaces, to adjust the deflection angle of the high lift device, whereas the **floats** and their **pylons** are screwed directly under the wing. The **vertical tail**, mounted on the aft cone, supports the horizontal stabilizer and ends with a 3D printed PLA cap.

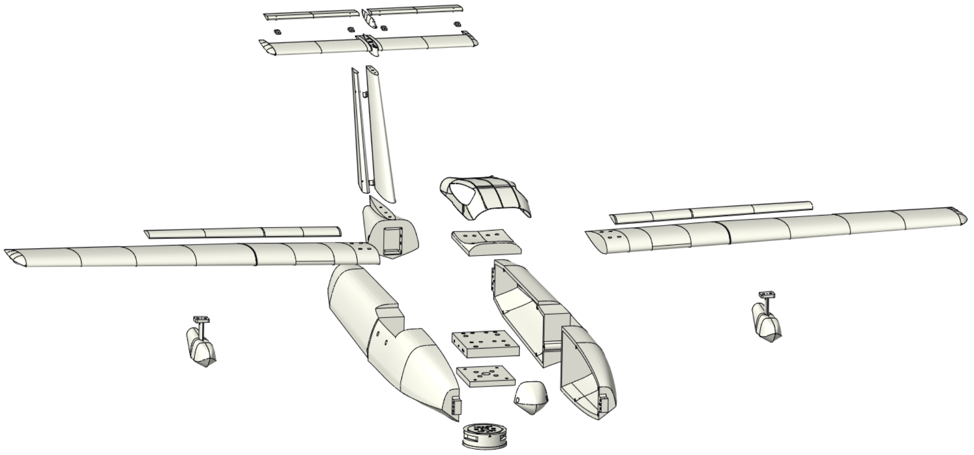

Figure 2.7: *Components of the test model*

2.2.1 Wing

Surface (S)	0.286 m^2
Span (b)	1.6 m
Root chord (c_r)	0.198 m
Tip chord (c_t)	0.139 m
Sweep angle at leading edge (Λ_{LE})	0 deg
Dihedral angle (Γ)	2 deg
Aspect ratio (AR)	8.953
Taper ratio (τ)	0.702

Table 2.3: *Characteristics of the wing*

The seaplane model is characterized by a **high wing**, tapered and with a **straight** leading edge. The high wing has a small **positive dihedral** while the **tapering** begins at the kink section, positioned at 33.9% of the semi-span. This section also separates the two sets of **Fowler flaps** with three configurations available: 0° for cruise, 20° for take-off, and 30° for landing.

Flap	c_f/c	η_i	η_o
Inner	0.3	0.125	0.338
Outer	0.3	0.341	0.670

Table 2.4: *Characteristics of the flaps*

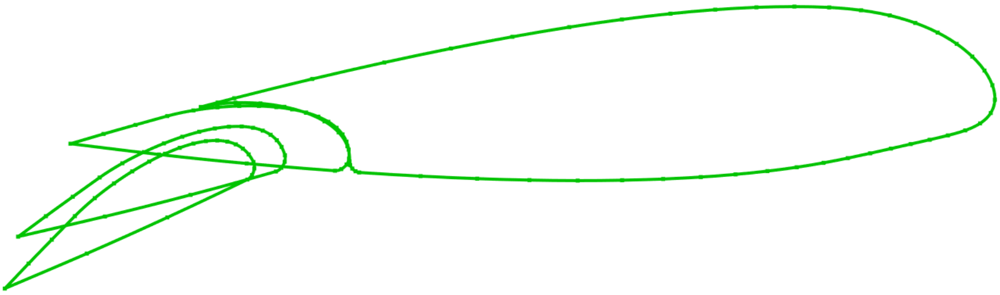

Figure 2.8: *Available deflections for the flaps*

The planform geometry, shown in figure 2.9, leads to a **mean aerodynamic chord** of 0.181 m, positioned along the semi-wingspan at 0.344 m. The two underwing **floats** have been installed to investigate their influence on stability and performance.

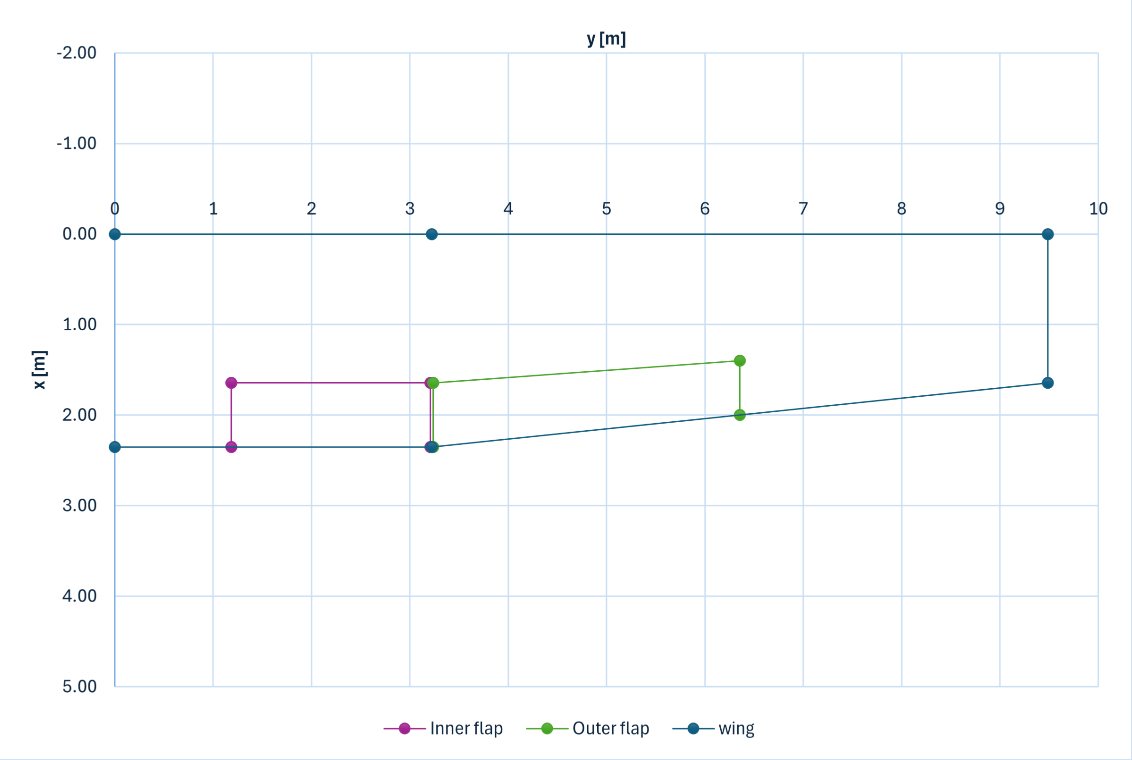

Figure 2.9: *Wing semi-span, plan view*

2.2.2 Tail

The adopted configuration is a large T-tail placed at a distance of 0.525 m from the point at $c/4$ on the **mean aerodynamic chord**.

Horizontal stabilizer and elevator

Surface (S)	0.050 m^2
Span (b)	0.46 m
Root chord (c_r)	0.11 m
Tip chord (c_t)	0.11 m
Sweep angle at leading edge (Λ_{LE})	0 deg
Aspect ratio (AR)	4.07
Taper ratio (τ)	1

Table 2.5: *Characteristics of the horizontal tail*

The horizontal stabilizer is embedded in the vertical tail, it is not **tapered** and presents a **straight** leading edge. With a **chord** of 0.11 m and a **surface** of 0.05 m^2 , the large surface is necessary to have higher control authority at low speeds. The **chord fraction** of the elevator is constant along the span and the possible deflections for the test model are: 0°, 10° and 20°.

	c_f/c	η_i	η_o
Elevator	0.38	0.07	0.95

Table 2.6: *Characteristics of the elevator*

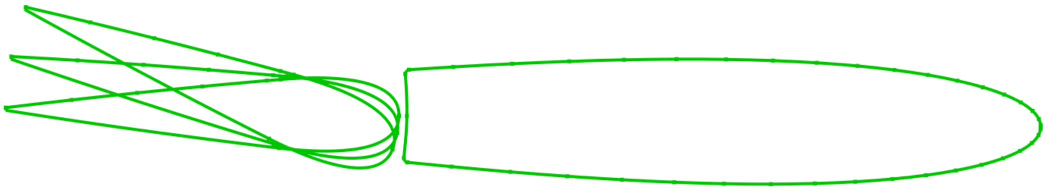

Figure 2.10: *Available deflections for the elevator*

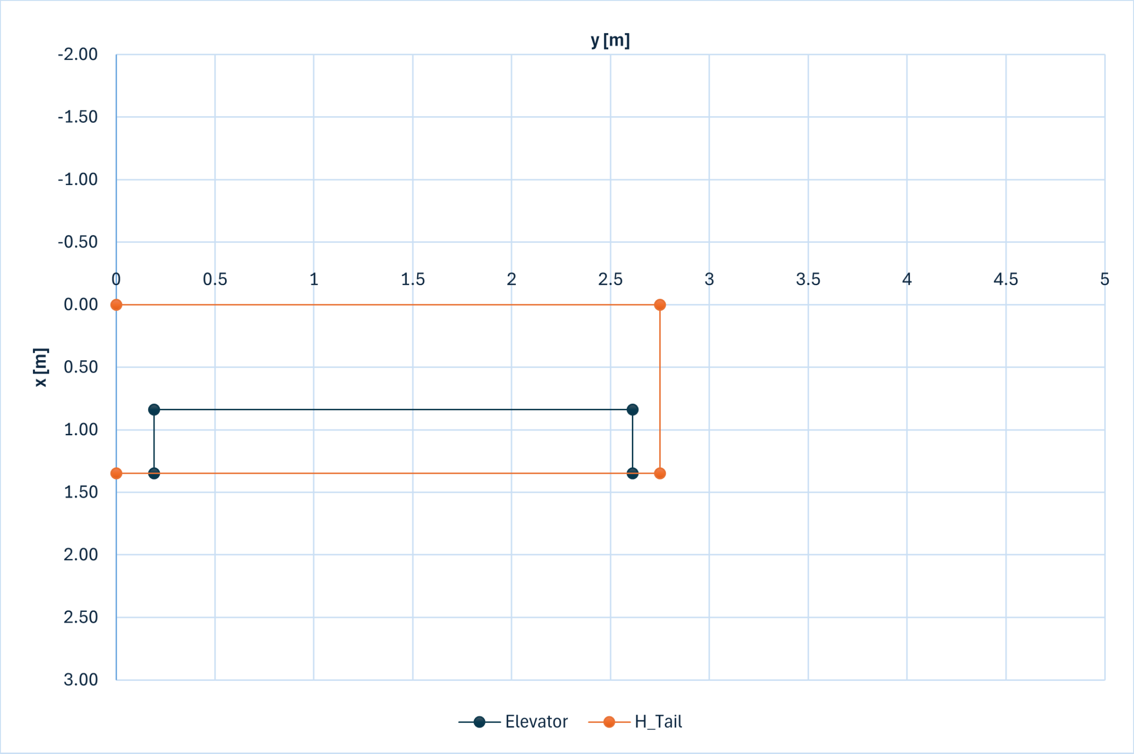

Figure 2.11: *Horizontal tail semi-span, plan view*

Vertical stabilizer and rudder

Surface (S)	0.050 m^2
Span (b)	0.299 m
Root chord (c_r)	0.22 m
Tip chord (c_t)	0.11 m
Sweep angle at leading edge (Λ_{LE})	35 deg
Aspect ratio (AR)	1.78
Taper ratio (τ)	0.51

Table 2.7: *Characteristics of the vertical tail*

The **span** is close to 0.30 m and is necessary to put the elevator in a higher position with respect to the wing as well as to grant high directional authority. The rudder extends from the 10% of the span to the 90%.

	c_f/c	η_i	η_o
Rudder	0.382	0.10	0.90

Table 2.8: *Characteristics of the rudder*

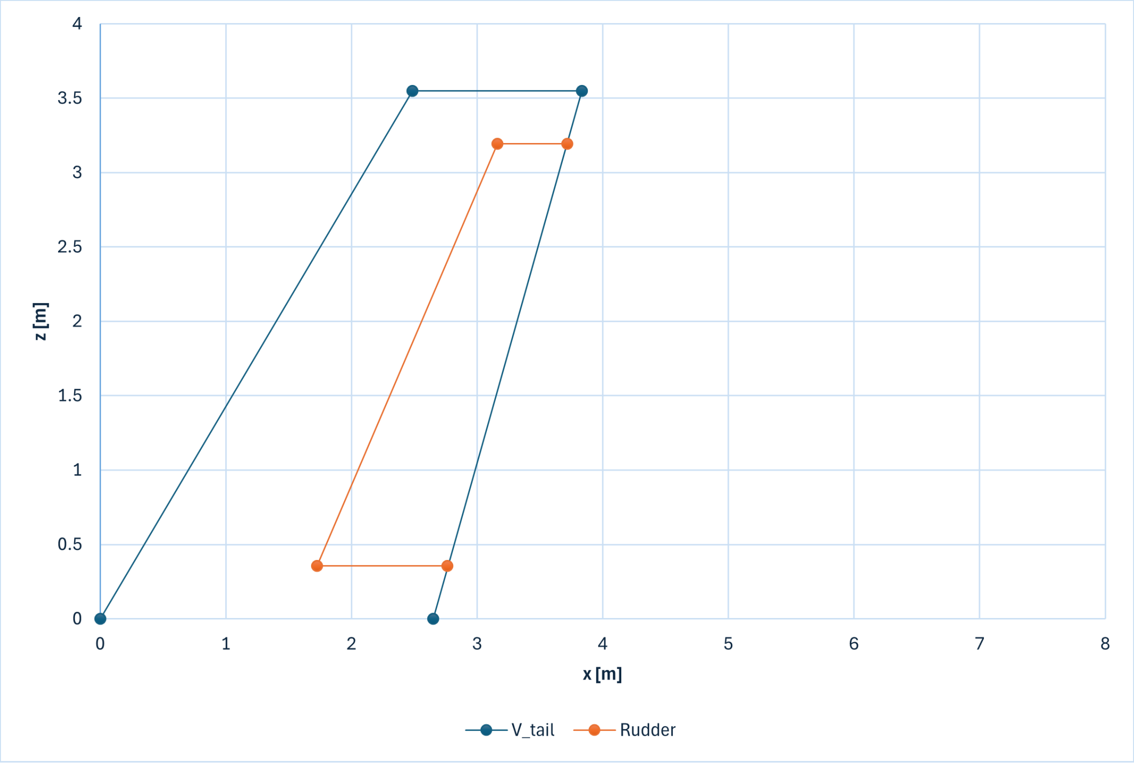

Figure 2.12: *Vertical tail, side view*

2.2.3 Fuselage

Length (L_f)	1.23 m
Max height ($z_{f_{max}}$)	0.14 m
Max width ($y_{f_{max}}$)	0.16 m
Fineness ratio (L_f/D_f)	8.2

Table 2.9: *Characteristics of the fuselage*

The fuselage is designed to meet the required performance during planing on water surface as well as to host the payload. The **hydrodynamic performances** in terms of buoyancy, stability, drag and water spray should meet the aerodynamic and structural requirements. These considerations lead to the introduction of the **hull**. The cross section, in fact, has a **maximum width** of 0.159 m and a **maximum height** of 0.141 m.

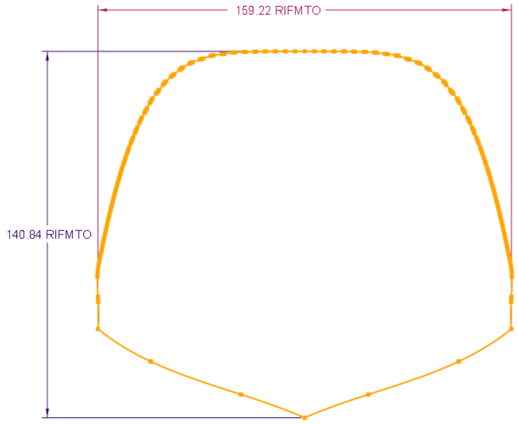

Figure 2.13: *Fuselage section*

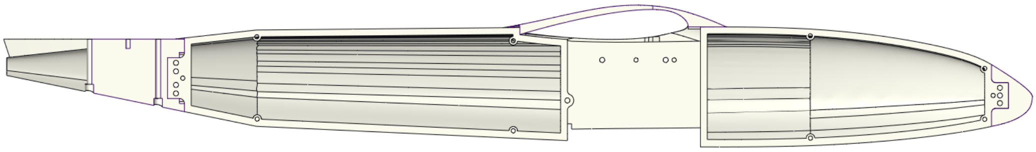

Figure 2.14: *Fuselage lateral geometry*

The fuselage model is characterized by the wing fairing on the upper surface and, in proximity of the center of gravity, by the housing for the balance system. The lower surface is then closed with a 3D printed cover to reduce interference with the flow.

2.3 ATI Delta balance

Wind tunnel tests of three-dimensional models require accurate measurements of forces and moments to estimate the aerodynamic coefficients and derivatives of different aircraft configurations and subsets. In order to acquire the data, the model must be held in position using wires or struts as supports. The applied loads can be obtained using either load cells or balances. The first solution can be cost-effective and has an easy calibration, but usually measures fewer components, mostly just one, with high precision; loading on a different axis than the measuring one can alter the signal, decreasing the effectiveness of the device. The balance allows for multi-component acquisition because of the more complex structure, which increases the cost; moreover, calibration is more elaborate, but avoids cross-talking between the axes. Both sensors rely on a component known as **strain gauge** to measure the applied loads.

The strain gauge is a semiconductor device which grants an accurate measurement of stationary forces and moments because of its physics. Knowing the mechanical characteristics of the component to which it is attached, the applied load can be derived from the strain $\epsilon = \frac{\Delta L}{L}$, where L is the original length of the gauge and ΔL is the increment. The strain itself is unknown, and it can be measured indirectly from the variation of the electric resistance, linked to it through the gauge factor $GF = \frac{\Delta R}{R}\frac{1}{\epsilon}$.

The resistance can be quantified with a Wheatstone bridge configuration circuit. Considering Figure 2.15, the unknown resistance R_g is obtained by regulating R_2 so that the bridge is balanced, hence the output voltage is zero. This happens when $\frac{R_1}{R_3} = \frac{R_2}{R_g}$, from which R_g can be evaluated.

When the wires connecting the strain gauge are too long with respect to the others in the bridge, their resistance modifies the balance. In fact, when balanced, $\frac{R_1}{R_3} = \frac{R_2}{R_g+2R_w}$. To avoid this condition, a three-wire configuration is used, where the output terminal is directly linked between one of the wires and the strain gauge so that R_w gives the same contribution to the upper and lower branches.

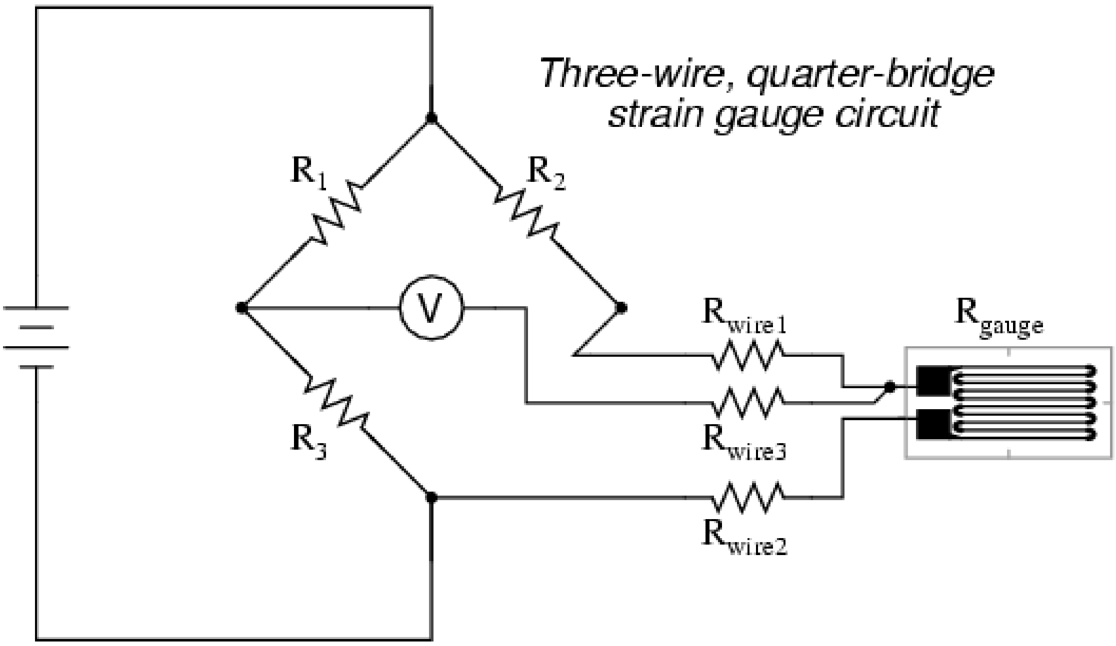

Figure 2.15: Three-wire Wheatstone bridge schematic

The change of the resistance is mainly caused by the loads, but variations due to temperature need to be considered. Usually a linear contribution is given by $\frac{\Delta R}{R} = \alpha\Delta T$, whereas an additional strain is caused by heat, $\frac{\Delta L}{L} = (\beta' - \beta'')\Delta T$, where β' and β'' depend on the materials used for the wire and the supporting component. Knowing these effects grants smooth acquisition and the correct measurement of applied loads.

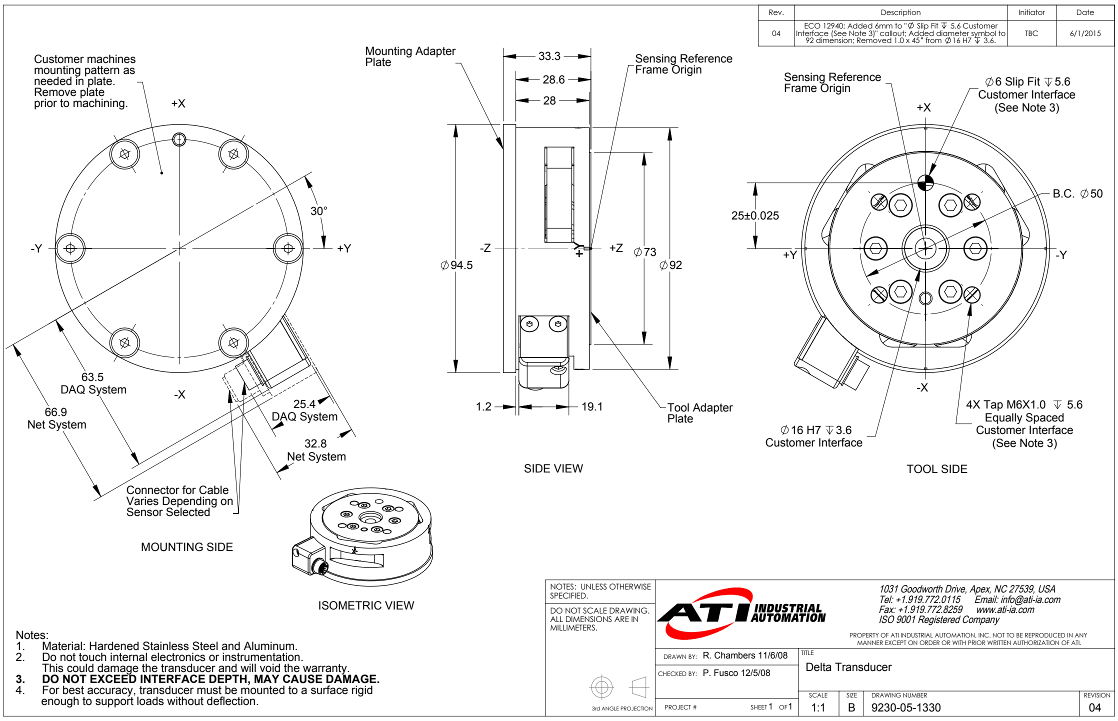

Figure 2.16: *ATI DELTA technical drawing*

The measurements on the Colossus model are conducted using an internal balance supported with a sting, housed inside the fuselage and connected to the interface plate under the wing. The balance used for the test is the ATI Delta. Machined from stainless steel but weighting only $0.913kg$ and with a maximum allowable single-axis overload at least 4.1 times higher than the rated capacities, the Delta transducer uses silicon strain gauges, which provide a signal 75 times stronger than conventional foil gauges. Amplifying this signal allows a near-zero noise distortion and a high signal-to-noise ratio.

Table 2.10: *ATI Delta sensor specifications*

	X/Y forces	**Z force**	**X/Y torques**	**Z torque**
Sensing range	$330N$	$990N$	$30Nm$	$30Nm$
Resolution	$\frac{1}{16}N$	$\frac{1}{8}N$	$\frac{5}{1333}Nm$	$\frac{5}{1333}Nm$
Single-axis overload	$3700N$	$10000N$	$280Nm$	$400Nm$
Stiffness	$3.6 \cdot 10^7 \frac{N}{m}$	$5.9 \cdot 10^7 \frac{N}{m}$	$5.2 \cdot 10^4 Nm/rad$	$9.1 \cdot 10^4 Nm/rad$
Resonant frequency	$1500Hz$	$1500Hz$	$1700Hz$	$1700Hz$

Chapter 3

Calibration and data treatment

In the preliminary design phase, conducting experimental tests under exact operating conditions is not possible due to the absence of a full-scale prototype model, since many design choices and characteristics are still under evaluation. In addition, flight tests are usually carried out during later design stages, as they require considerable financial, temporal, and logistic resources. These costs include hangar fees, transport (both for the prototype and staff, often spanning multiple days), and fuel. Furthermore, they involve complex management of time slots and personnel roles.

Laboratory tests, on the other hand, allow the evaluation of parameters of interest in a controlled environment. This effectively eliminates variations caused by factors independent of the model's characteristics. Additionally, they are:

- **More cost-effective**: the wind tunnel model usually requires a less complex structure, with less production effort and materials, compared to a full-scale aircraft. Reduced space and consumables are needed, which decrease storage and maintenance costs. Moreover, the laboratory is often located close to the headquarters, requiring only the activation of the test system and involving more affordable logistics.
- **Faster**: while the full aircraft is a complex system that may present issues across various components and cause delays (especially when implementing new technologies), wind tunnel testing focuses almost exclusively on specific subsystems, mainly involving external aerodynamics. The models usually present less complex active parts, which leads to fewer failures and technical checks.
- **More versatile**: in the case of parts requiring modification or substitution, performing such operations on a test model is more straightforward than doing so on a real prototype, which must be compliant with stricter technical and safety standards.

These characteristics make wind tunnel testing an effective evaluation method for obtaining a preliminary estimate of the aerodynamic properties of the designed model. However, these significant advantages introduce some non-negligible issues.

Wind tunnel facilities can often match only one parameter between Mach and Reynolds, making it necessary to select which effect, between compressibility and viscosity, is more relevant for the specific campaign.

In case of difficulty in reaching high velocities, tests can be carried out only in limited conditions of the flight envelope. The feasibility of simulating specific flight conditions, such as gusts and extreme weather conditions, is one of the most limitative aspects of wind tunnel testing. Some facilities offer the possibility of conducting such tests, but the higher costs need careful evaluation.

3.1 Wind tunnel corrections

In wind tunnel tests, models are situated inside a test chamber surrounded by walls, whereas standard conditions would involve unbounded space. Consequently, values obtained directly from the laboratory do not represent the actual performance of the aircraft and require specific corrections before being compared with real-world data. Moreover, even at the maximum testing speed, the Reynolds number $Re = \frac{\rho V L}{\mu}$ can differ from the one reached during flight, hence particular care should be paid to represent the correct behaviour of the boundary layer.
Wind tunnel wall corrections are related to the influence on the flow around the model and consist of:

- **Buoyancy drag**
- **Solid and wake blockage**
- **Upwash**
- **Streamline curvature**

These effects are evaluated by **semi-empirical equations** and can be applied directly during the acquisition phase through corrective coefficients for lift, drag, pitching moment and angle of attack.

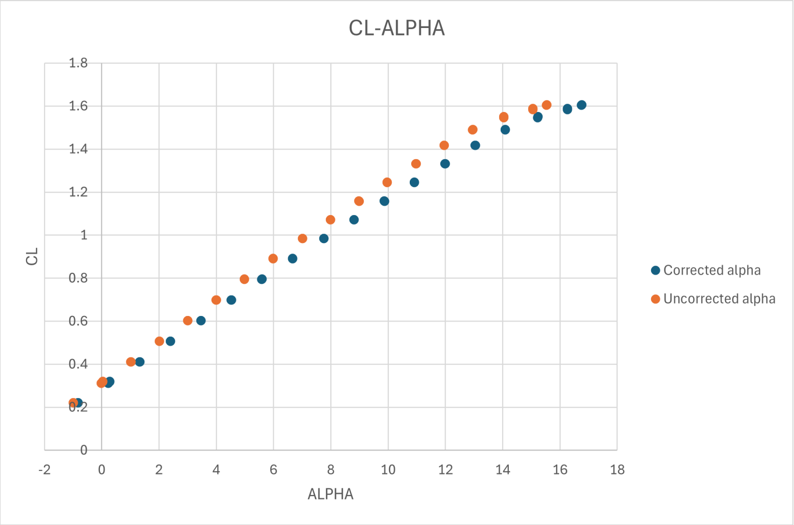

Figure 3.1: *Lift coefficient curves plotted with respect to corrected and uncorrected α (flaps retracted)*

3.1.1 Buoyancy drag correction

Buoyancy drag is an increment in the overall drag coefficient due to a longitudinal pressure gradient caused by the thickening of the boundary layer on the walls of the tunnel.

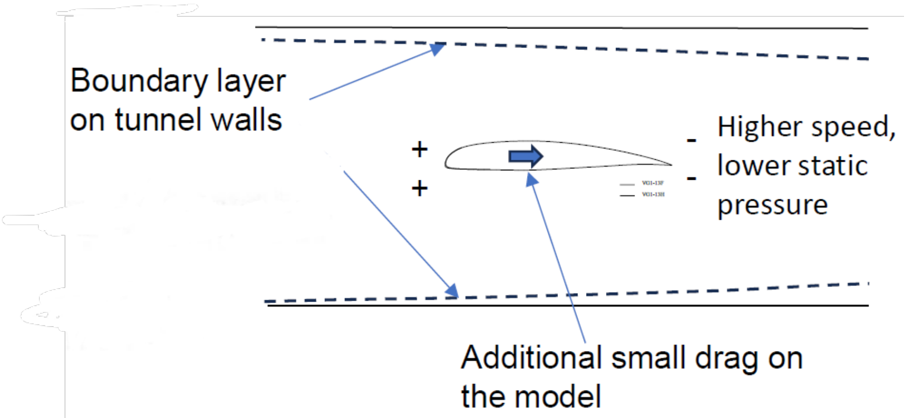

Figure 3.2: *Buoyacy drag*

The boundary layer, in fact, creates a converging duct that causes the difference in static pressure between the upstream and downstream sections of the test chamber. The effect is estimated through the following equations:

$$D_B = -\frac{\pi}{4}\lambda_3 t^3 \frac{dp}{dx} \tag{3.1}$$

Where λ is the body shape factor related to the fineness ratio of the tridimensional model [4], which for an aircraft is the fuselage, t is the max thickness of the fuselage in the lateral view.

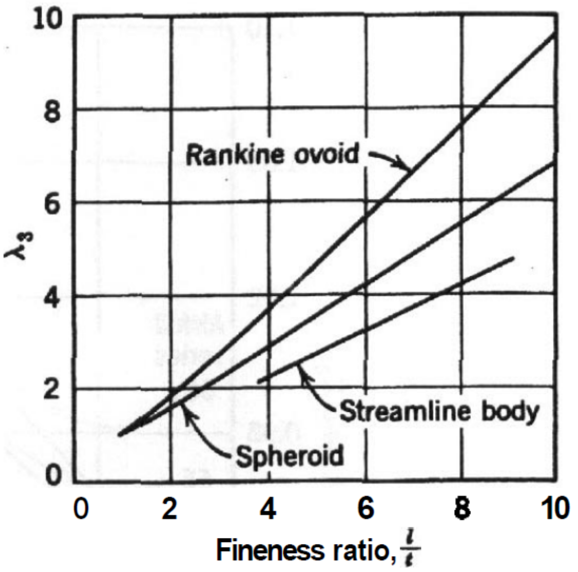

Figure 3.3: *λ_3 values*

The pressure gradient can be directly measured, without the model, in the wind tunnel by using two pressure probes located at the inlet and outlet of the test chamber. Otherwise, it can be estimated as follows:

$$\frac{dp}{dx} = -k\frac{(\rho/2)V^2}{B} \tag{3.2}$$

Where B is the tunnel jet width, ρ is the density of the flow and V the velocity measured. k is an experimental factor and his value is $0.016 - 0.04$ [4]. This value of the drag should be subtracted to the drag acquired during tests.

3.1.2 Blockage correction

Solid and wake blockage are due to the presence of the model in the test chamber. The volume and wake of the object, in fact, reduce the cross-sectional area in the test chamber, increasing the velocity of the flow compared to the airspeed detected from sensors, leading to higher dynamic pressure and forces which have to be subtracted from the measurement. The blockage correction has to be applied on the lift, moment and drag coefficients. The velocity increase is less than one-fourth of the one obtained by the direct reduction in cross-sectional area[4].

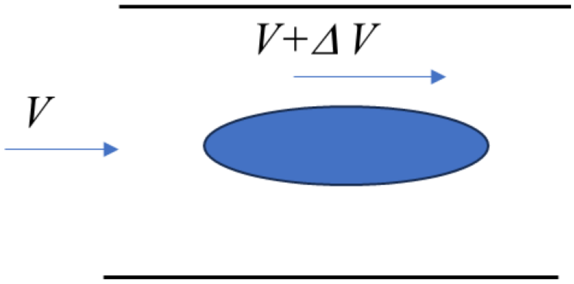

Figure 3.4: *Solid blockage*

The solid blockage coefficient ϵ_{sb} is estimated both for the lifting surfaces (wing, horizontal and vertical planes) and fuselage. The influence of the body on the flow is described by a doublet, representing the body, confined in an infinite series of vertical doublets of the same intensity. The mathematical model leads to the definition of the **solid blockage coefficient**:

$$\epsilon_{sb_{wing}} = \frac{K_1\tau_1}{C^{3/2}}.V_{wing} \tag{3.3}$$

$$\epsilon_{sb_{fus}} = \frac{K_3\tau_1}{C^{3/2}}.V_{fus} \tag{3.4}$$

Where C is the cross-sectional area of the test chamber, K_1 and K_3 are body and wing shape factors related to the **thickness ratio** (Fig.3.5), τ_1 is a coefficient related to the ratio between the model span and the tunnel breadth B and the ratio $\frac{B}{H}$, where H is the tunnel height (Fig.3.6). V is the volume of the given component.

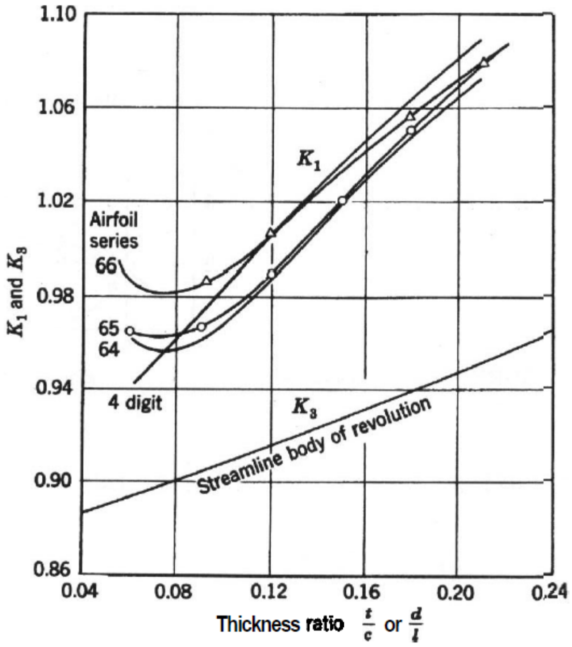

Figure 3.5: *K_1 and K_3 coefficients estimation graph*

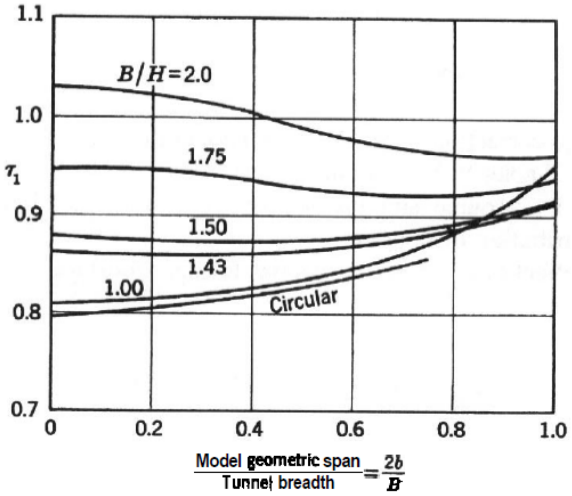

Figure 3.6: *τ_1 coefficient estimation graph*

The wake blockage, similarly to the solid blockage, is the increment of the velocity due to the wake. The effect is related to the uncorrected drag coefficient of the model and is derived using an infinite source-sink distribution spacing both tunnel height and tunnel width.

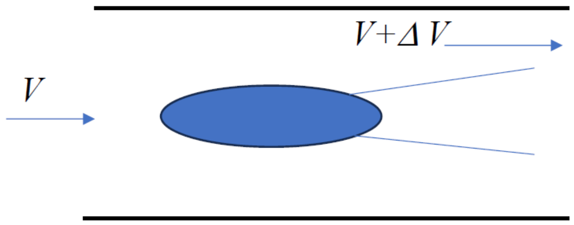

Figure 3.7: *Wake blockage*

The **wake blockage coefficient** is:

$$\epsilon_{wb} = \frac{S}{4C} C_{D0u} \tag{3.5}$$

where C_{D0u} is the uncorrected parasite drag coefficient, which can be evaluated with an iterative approach: a first estimate, with a semi-empirical method, is used to acquire the C_{D0}, then the latter is employed for the next test until convergence is reached.
The total blockage coefficient, ϵ is the sum of solid and wake blockages. The correction is directly applied to the dynamic pressure

$$\frac{q_c}{q} = \left(\frac{V}{V_u}\right)^2 = (1+\epsilon)^2 = 1 + \epsilon^2 + 2\epsilon \tag{3.6}$$

The term ϵ^2 can be neglected and

$$\frac{q}{q_c} = \frac{1}{(1+\epsilon)^2} \approx \frac{1}{1+2\epsilon} \approx 1 - 2\epsilon \tag{3.7}$$

For example, the correction due to wake blockage applied on lift coefficient is

$$C_{L_c} = C_L \frac{q}{q_c} = C_L \frac{1}{(1+\epsilon)^2} \approx C_L(1-2\epsilon) \tag{3.8}$$

3.1.3 Upwash correction

The side walls affect the model through the **upwash** effect, which can be explained via the method of images. Mathematically, the walls are modeled by mirrored vortices. The side vortices enforce the upwash field of the wing, increasing the actual angle of attack.

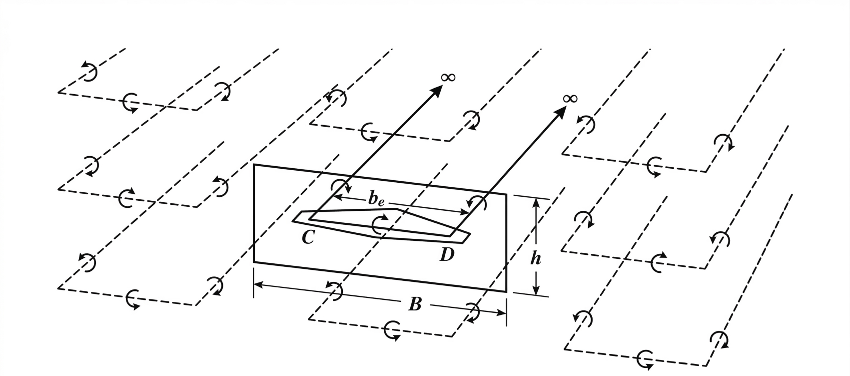

Figure 3.8: *System of image vortices*

This requires additional contributions to account for the tilting of the aerodynamic forces. Since the increase in drag is related to the projection of the lift, which is usually the larger force, the coefficient that is mainly affected is the C_D.

The upwash correction factor δ is related to the distance between the wingtips and the walls through the ratio $\dfrac{b_e}{B}$ where b_e is the effective span and B is the width of the test section.

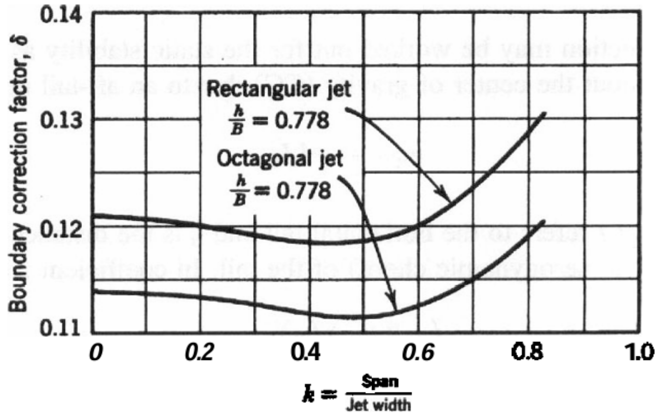

Figure 3.9: *δ estimation graph*

The effective span is defined as the mean between the geometric wingspan and the vortex span, the distance between the cores of the wingtip vortices. The latter can be estimated from semi-empirical relations linked to the geometric characteristics of the wing.

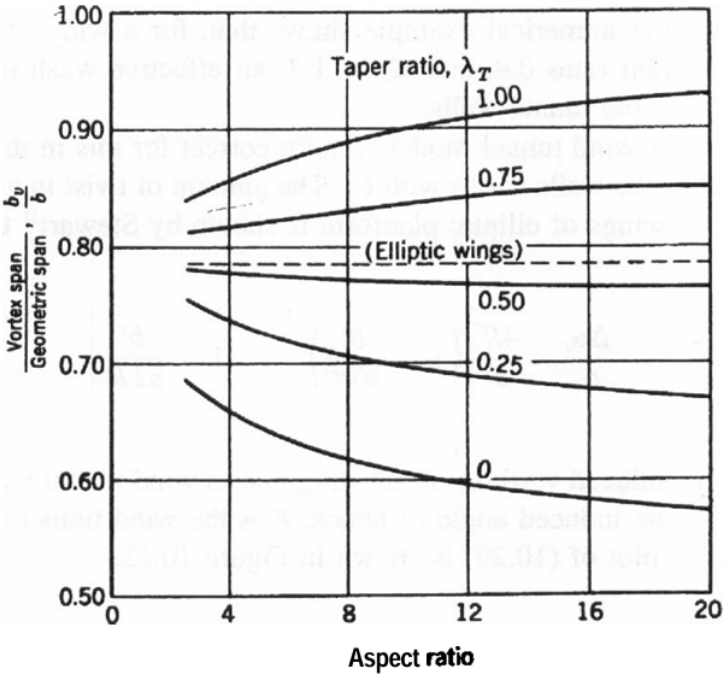

Figure 3.10: *b_v estimation graph*

Once δ is known, the angle of attack correction due to the upwash can be computed as:

$$\Delta\alpha_{up} = \delta \frac{S}{C} C_{L_w}, \tag{3.9}$$

leading to the following drag correction:

$$\Delta C_{D_{up}} = \delta \frac{S}{C} C_{L_w} C_L = \Delta \alpha_{up} C_L. \tag{3.10}$$

3.1.4 Streamline curvature correction

The **streamline curvature** effect relates to the behaviour of the air between the model and the horizontal walls of the test section. It is important to note that traditionally, for aircraft tests, this phenomenon is treated differently for the wing and the tail.

Normally, a lifting model would bend the streamlines around it proportionally to its wing circulation Γ. While the streamlines can diverge vertically in open air, inside the test section the walls prevent this outward deflection, forcing them to remain straight near the walls. Near the wing surface, this results in the streamlines being bent more downwards with respect to the unbounded condition. For an airfoil of given curvature, this is equivalent to being more cambered than it really is, since higher camber leads to stronger downwash. In fact, the acquired lift and moment will be higher than the unbounded values, as if the angle of attack was higher than the measured one. Usually, the required corrections are distributed between the angle of incidence and the lift coefficient, increasing the first and reducing the latter, then taking these corrections into account for the wing moment coefficient (equations 3.11, 3.12, 3.13) .

The angle correction can be related to $\Delta\alpha_{up}$ scaled by a factor τ_2, proportional to the aspect ratio of the test section $\frac{H}{B}$ and the ratio between the tail length and the test section width $\frac{l_t}{B}$. Regarding the wing, $l_t = 0.25\bar{c}$ (approximately the distance between the wing aerodynamic center and the center of gravity), for the tail $l_t = x_{ac_H} - x_{cg}$.

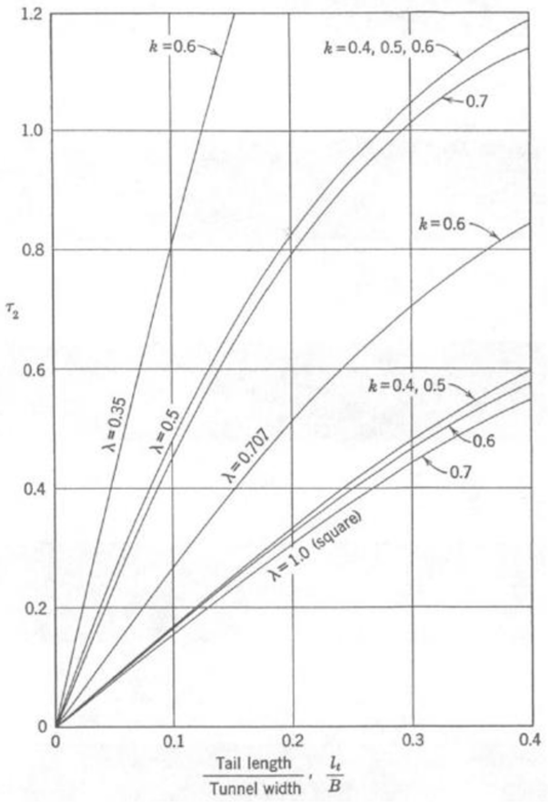

Figure 3.11: *τ_2 estimation graph*

As the tunnel width B decreases, the image vortices are brought closer to the physical model. The proximity induces a stronger upwash field along the tunnel centerline. Since the upper and lower walls constrain this intensified flow field, the resulting streamline curvature effect is magnified. Therefore, a lower value of B results in a stronger interaction between the model's circulation and the tunnel boundaries.
The angle correction can be written as

$$\Delta\alpha_{sc} = \tau_{2w}\delta(\frac{S}{C})C_{L_w} = \tau_{2w}\Delta\alpha_{up}. \tag{3.11}$$

which leads to a lift coefficient correction due to the streamline curvature effect

$$\Delta C_{L_{sc}} = \tau_{2w}\delta(\frac{S}{C})C_{L_w}C_{L_{\alpha_w}} = \tau_{2w}\Delta\alpha_{up}C_{L_{\alpha_w}} = \Delta\alpha_{sc}C_{L_{\alpha_w}}. \tag{3.12}$$

The lift correction is done considering the wing as the main lifting surface, hence it primarily affects the aircraft through this component.
Lastly, the wing moment coefficient is adjusted with

$$\Delta C_{\mathcal{M}_{wsc}} = 0.25\tau_{2w}\delta(\frac{S}{C})C_{L_w}C_{L_{\alpha_w}} = 0.25\tau_{2w}\Delta\alpha_{up}C_{L_{\alpha_w}} = 0.25\Delta\alpha_{sc}C_{L_{\alpha_w}} = 0.25\Delta C_{L_{sc}}. \tag{3.13}$$

Since the flow gets straightened by the horizontal walls, the tail usually works with a higher angle of attack than it would in the unbounded condition, resulting in a more stable aircraft. The total moment coefficient then requires an additional correction to take this into account:

$$\Delta C_{\mathcal{M}_{tsc}} = C_{\mathcal{M}_{\alpha_t}} \tau_{2t} \delta \frac{S}{C} C_L \tag{3.14}$$

In summary, the formulas for the corrected coefficients, in explicit form, can be written as:

$$C_{L_c} = C_L(1 - 2\epsilon) - \tau_{2w}\delta(\frac{S}{C})C_{L_w}C_{L_{\alpha w}} \tag{3.15}$$

$$C_{D_c} = C_D(1 - 2\epsilon) + \delta\frac{S}{C}C_{L_w}C_L + \frac{\pi}{2\rho V^2 S}\lambda_3 t^3 \frac{dp}{dx} \tag{3.16}$$

$$C_{\mathcal{M}_c} = C_{\mathcal{M}}(1 - 2\epsilon) - 0.25\tau_{2w}\delta(\frac{S}{C})C_{L_w}C_{L_{\alpha w}} - C_{\mathcal{M}_{\alpha_t}}\tau_{2t}\delta\frac{S}{C}C_L \tag{3.17}$$

3.1.5 Calculated parameters

Having investigated the theory behind the data treatment required for the uncorrected coefficients, it is necessary for the purpose of this thesis to present the parameters employed during the tests of the Colossus model for various test configurations, which will be explored in the next chapter.

Table 3.1: *Correction parameters for the cruise configuration*

	Wing-body	**Body-tail**	**Wing-body-vertical**	**Wing-body-tail**	**Wing-body-tail-pods**
Reference surface	0.286m	0.286m	0.286m	0.286m	0.286m
ϵ_{sb}	0.0038	0.0028	0.0040	0.0041	0.0042
C_{D0}	0.030	0.015	0.030	0.030	0.033
δ	0.116	0.114	0.116	0.116	0.116
C_{D_B}	0.0002	0.0002	0.0002	0.0002	0.0002
$\Delta C_{D_{wb}}$	$3.06 \cdot 10^{-5}$	$1.38 \cdot 10^{-5}$	$3.08 \cdot 10^{-5}$	$3.10 \cdot 10^{-5}$	$3.11 \cdot 10^{-5}$
τ_{2w}	0.063	0	0.063	0.063	0.063
τ_{2t}	0	0.81	0	0.81	0.81
$C_{\mathcal{M}_{\alpha_t}}$	0	−0.0398	0	−0.0398	−0.0398

3.1.6 Transition control

One of the most important parameters for wind tunnel tests is the Reynolds number, which measures the relative importance of the inertial effects compared to the viscous ones. To correctly represent the flow behaviour with respect to turbulence during a test, the Reynolds number should match the one of the flight condition under investigation. This is not always possible, as high testing speeds require powerful fans and higher costs. In fact, a given fan can work only within a specific range of $\Delta P - G$, where the first is the total pressure loss and the latter the volumetric flow rate, and the available operating conditions of the facility are given by the intersection of the characteristic curve of the wind tunnel itself and the band of the fan.

If the testing Reynolds is lower than the operating one, the boundary layer on the model will be laminar on a larger portion of the surfaces. This decreases the skin friction drag because in a laminar boundary layer profile the shear stress at the wall $\tau_w = \mu \frac{\delta u}{\delta y}|_w$ is lower compared to the turbulent condition, given the lower velocity derivative and viscosity. In the turbulent boundary layer, an additional viscosity can be used to model the flow behaviour, contributing to the growth of the shear stress. The latter is directly linked to friction drag through the integral of the skin friction coefficient $C_f = \frac{\tau}{\frac{1}{2}\rho_\infty u_\infty^2}$, thus if the laminar boundary layer insists for a longer distance, the local Reynolds number at which transition occurs increases, and the friction drag decreases, leading to a lower C_D compared to the operative scenario.

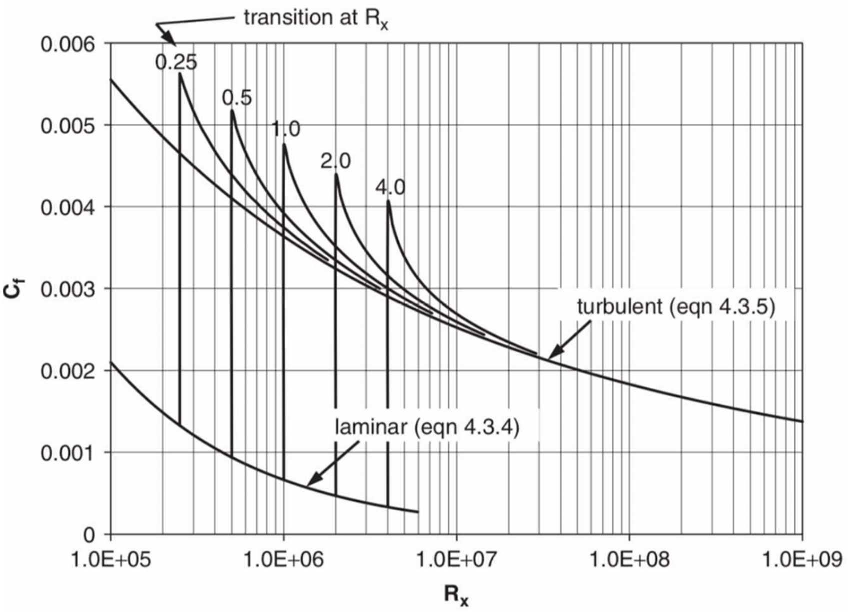

Figure 3.12: *Local skin friction coefficient for a flat plate, varying with local Reynolds number*

Furthermore, the laminar boundary layer is more sensitive to adverse pressure gradients and this leads to separation happening prematurely at lower angles of attack.

For a given streamwise pressure gradient and shear stress distribution, the flow undergoes stronger accelerations where u is small, thus the bottom of the boundary layer. Usually, both laminar and turbulent velocity profiles show negative $\frac{\partial \tau}{\partial y}$, resulting in a net viscous force that slows down the fluid. If the pressure gradient is adverse (positive), then a strong deceleration occurs close to the surface. Since in this condition the lower part of the boundary layer is slowed the most, $\frac{\partial \tau}{\partial y}$ changes sign, resulting in a viscous force that accelerates the fluid, causing a certain resistance to separation. Clearly, the larger the shear gradient, the more the flow will remain attached in an adverse pressure gradient. In a turbulent boundary layer, the shear stress can be modeled as $\tau = (\mu + \mu_t)\frac{\partial u}{\partial y}$ and by deriving it with respect to y, one gets $\frac{\partial \tau}{\partial y} = (\mu + \mu_t)\frac{\partial^2 u}{\partial y^2} + \frac{\partial \mu_t}{\partial y}\frac{\partial u}{\partial y}$. Since μ_t has a positive gradient at the bottom of the boundary layer the last term is also positive, increasing the viscous force contribution against the adverse pressure gradient compared to a laminar flow.

Because of this, when the Reynolds number is too low, separation can occur on strongly convex surfaces, such as the wing or the elevator, near the leading edge. In fact, after reaching the negative pressure peak, the laminar boundary layer can not resist the adverse pressure gradient on most airfoils. This leads to flow detachment but, if transition occurs at a reasonable distance from the separation line, the turbulent boundary layer may be able to reattach to the surface.[1] The limited separated region is called **laminar separation bubble**, which also alters the effective shape of the wing, hence pressure distribution and lift. In addition, as the angle of attack increases, the bubble can move forward and suddenly burst, which is called a "leading-edge stall", or expand downstream until flow is unable to reattach, identified as "thin-airfoil stall". Both behaviours can result in abrupt stalling of the wing and sudden increase of drag at a surprisingly low angle of attack. As said before, this happens at low Reynolds, which usually are not representative of the real flight conditions, and hence most of the time separation bubbles should be avoided. To grant a more realistic behaviour of the boundary layer, trip strips can be applied to the surface to increase the surface roughness and force a bypass transition at a certain location upstream of the one at which laminar separation occurs. This is also the main limitation of this solution, since in natural flows the separation occurs at different locations as the angle of attack increases, thus the optimal position for the strip moves along the chord. An important feature of the strip is the thickness, as it modifies the disturbance seen by the flow in the boundary layer. Trip strips should be sufficiently thick to effectively induce transition, but not so that they generate a wake inside the boundary layer, increasing the pressure drag and potentially leading to early flow detachment.

---

[1] If the Reynolds number evaluated with the displacement thickness is sufficiently high, transition occurs shortly after separation, usually resulting in reattachment [20]

Figure 3.13: *Oil flow visualization on the Colossus model for trip strip selection and positioning ($\alpha = 5°$, flaps cruise)*

In the figure above, visualization of the oil flow at a 5° angle of attack is shown. The first and third strips have a thickness of $0.25mm$, whereas the second and fourth of $0.50mm$, to select the correct height of the disturbance. At the sections where no strip was applied, it is evident that the flow has a laminar evolution until, at around 14% of the chord, separation occurs and a bubble forms, with a turbulent reattachment at $20 - 22\%$. Where the strips are located, no laminar bubble forms and transition is forced successfully, with the lower thickness being sufficient to ensure it while thicker strips generate a large oil build-up immediately downstream. As for the chordwise location at which the strips have to be positioned, visualizations at different angles have been carried out. Applying the strips upstream for high angles of attack, noticeably increased drag, since at lower angles a smaller part of the wing experienced laminar flow, but avoided laminar separation close to the stall, better representing the impact of turbulence in the nonlinear section of the C_L curve compared to the downstream positioning required for lower angles, which on the other hand granted a higher reliability of the drag curve and a more realistic behaviour in the linear section. As these preliminary tests focused on the stability and control derivatives and on global aerodynamic performance, the latter positioning was used.

3.2 Balance calibration and tare weight correction

3.2.1 Calibration

Balance calibration is the procedure that ensures proper acquisition of data during tests. Loads are measured by converting six voltage signals received by the strain gauges to six load components, three forces and three torques. The conversion is performed by a $6x6$ matrix, whose coefficients represent the contribution of each strain gauge tension to a specific component of the stress. The calibration consists in calculating the 36 components of the matrix. During this procedure, six tests are carried out, each characterized by a known force or moment applied on the balance; voltage values are collected and a linear system of six equations in 36 unknowns of the type

$$\{F\} = [C] \cdot \{V\} \tag{3.18}$$

can be written; on the right hand side there is the voltage vector measured multiplied by the unknown matrix of coefficients, and on the left hand side the applied forces. To obtain a correct evaluation of the calibration matrix, all six components should be applied, preferably one at a time; decoupling the solicitation, in fact, ensures an accurate estimation of the coefficients. It is also important to perform the procedure applying typical loads that are expected during the experiments to better tune the coefficients. The tests performed are:

1. F_X **test**;
2. F_Z **test**;
3. M_Y **test**;
4. M_X **test**;
5. F_Y **test**;
6. M_Z **test**;

The tests are carried out applying loads on the balance through a specific steel structure, consisting of an interface plate, which is connected to the balance, and four horizontal steel arms forming a cross in the $x - y$ plane; this type of structure allows the application of forces and moments as F_Z, M_X and M_Y. Additional vertical steel bars are placed at the tips to ensure the application of F_X, F_Y and M_Z.

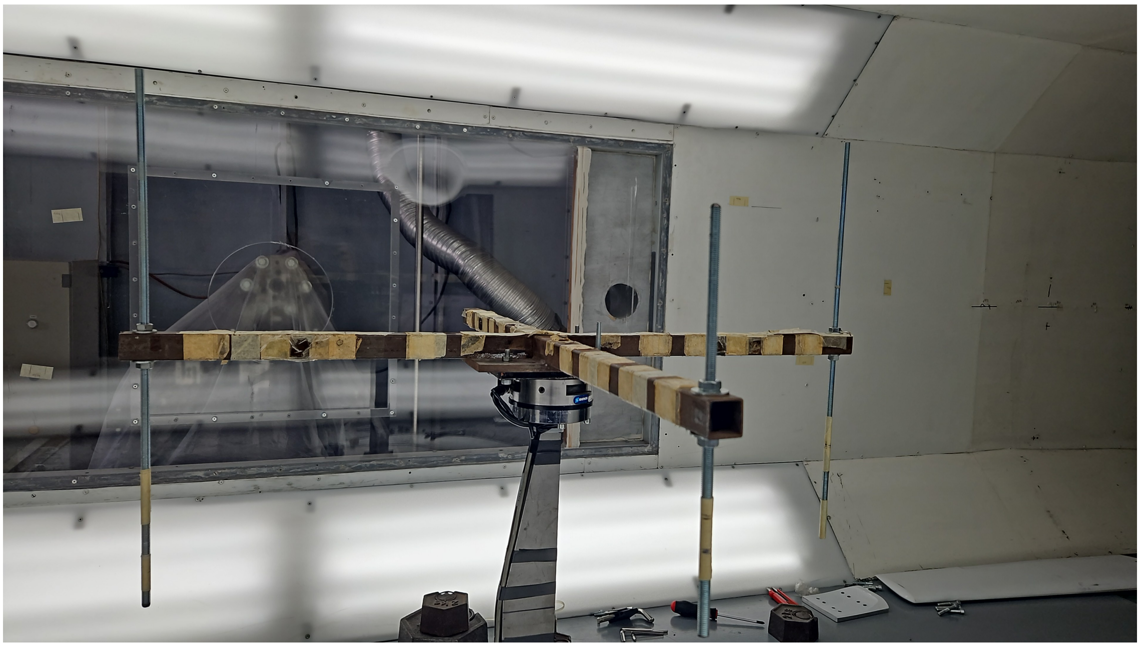

Figure 3.14: Steel structure for the application of the loads.

The F_X test is performed by exerting a tensile force along the longitudinal axis via a steel wire that connects the vertical bar to a pulley system loaded with a specified mass. The mass is previously measured, and a load cell is integrated into the steel wire to monitor any tension losses that might affect the actual load applied to the balance. To ensure decoupling from other forces and moments, the application point and direction of the tensile force are accurately measured prior to data acquisition to exert the forces intersecting the balance center. Any misalignment between the force direction and the longitudinal axis introduces additional moments, which would lead to inaccuracies in the evaluation of the calibration coefficients.

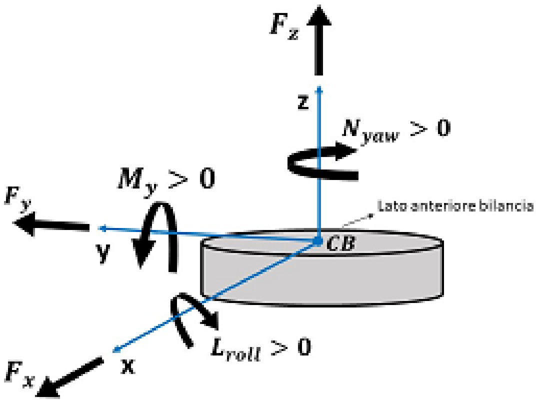

Figure 3.15: Balance reference system

Before proceeding with voltage measurements, a mass of $25kg$ is placed on the interface plate to simulate experimental conditions, specifically the presence of the aircraft model. Additionally, a $1kg$ mass is loaded onto the pulley system to ensure proper tension in the steel wire. These initial loads do not affect the data acquisition as they are applied prior to establishing the reference voltage. Indeed, once the 'zero' reference is set, the measured voltage corresponds exclusively to the calibration load, namely F_X. The calibration load measured by the balance is $1.977kgf$, which corresponds to a typical value of the force produced during the experiments.

Figure 3.16: *F_X calibration test.*

The F_Z test involves applying a vertical force by placing two masses along the horizontal bars using steel hooks. These hooks feature a sharp tip to ensure accurate centering of the loads along the bars. The two masses are positioned along the longitudinal axis at symmetric distances with respect to the center of the balance, thus exerting only vertical forces. The total calibration load is $10.45kgf$, which includes the two masses and the hooks, all accurately weighed before the procedure. As in the previous test, an additional $25kg$ mass is placed on top of the balance to better simulate the weight of the model during the tests. Since the lift alleviates the vertical load on the balance, reducing the net model weight, the reference voltage is established with both the calibration and additional masses applied. The measurement is carried out after removing the calibration load. Consequently, the voltage corresponds to an upward vertical force of $10.45kgf$.

The M_Y test is performed by applying a moment on the y-axis by positioning a mass along the horizontal bar at a specific distance from the balance center. The procedure is similar to the F_Z test, though only a single mass is used to generate the moment. The pure pitching moment is ensured by two factors: the mass is placed strictly along the longitudinal axis to exclude M_X components and a differential measurement approach is adopted. The reference voltage is set with the calibration mass at a specific distance from the balance center. The voltage is then measured after moving the mass to an equivalent distance on the other side of the center. Consequently, the net F_Z load remains zero while the resulting pitching moment, the value of witch is $2.006 kgm$, is equivalent to that produced by the same mass at twice the distance. During the estimation of calibration coefficients, the voltage values are averaged before being integrated into the system of equations.

Figure 3.17: *M_Y calibration test.*

The M_X test involves exerting a rolling moment along the longitudinal axis in a manner similar to the M_Y test. The mass is initially placed on left arm of the structure, then after setting the reference value of the voltages the mass is moved on the other side at the same distance, producing a rolling moment of $2.0896 kgm$.

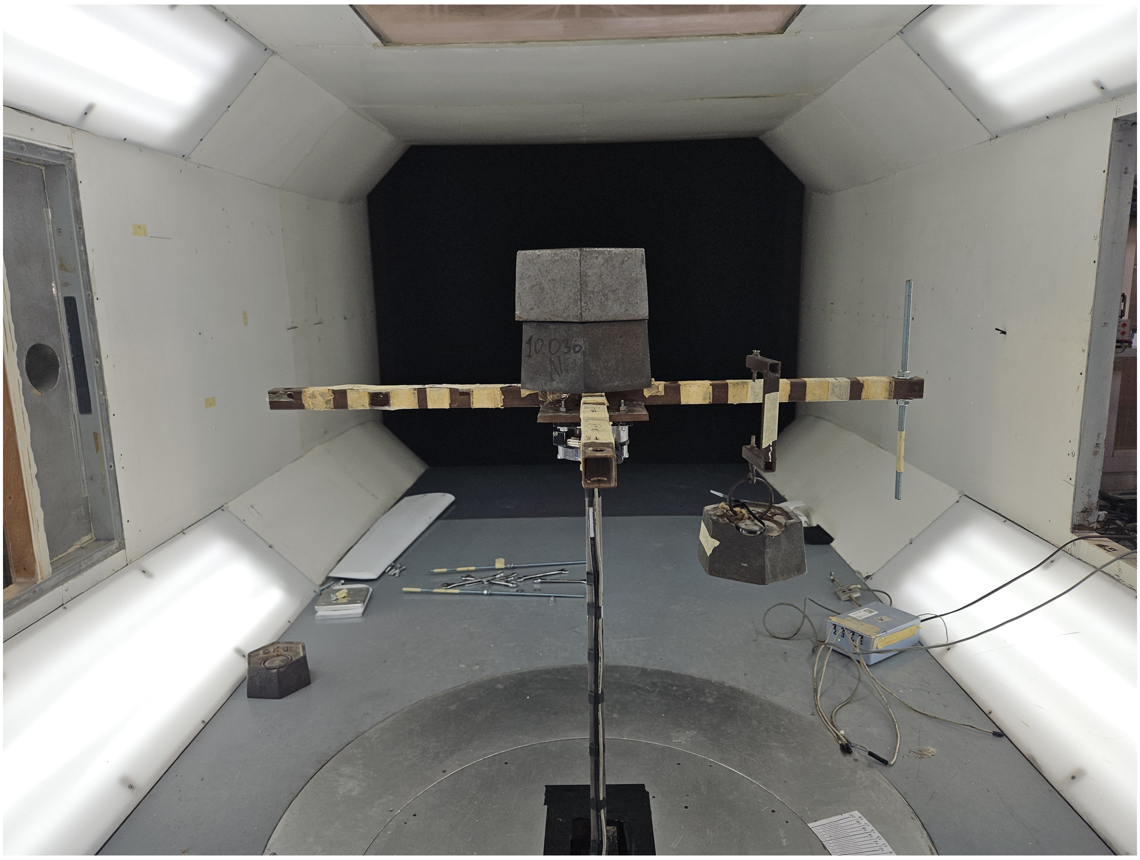

Figure 3.18: *M_X calibration test.*

The F_Y and M_Z tests follow procedures very similar to the pulley system described for the F_X test. Specifically, the F_Y test is performed by applying a lateral force of $-2.014 kgf$. Unlike the other tests, it is not possible to achieve a pure lateral force in this configuration. Since the line of action of the force, defined by the bar, does not intersect the balance center, an M_Z is generated. This moment is calculated as the product of the lateral force and the lever arm, defined by the $0.015m$ offset between the force's line of action and the balance center, resulting in a total moment of $-0.0302 kgm$.

Figure 3.19: *F_Y calibration test.*

The M_Z test is conducted similarly to the F_Y test, but the load is applied at a different location. Specifically, the pulley system is connected to the vertical bar used for the F_X test, exerting a lateral force of $-1.975kgf$ and a resulting yaw moment of $-0.7782kgm$. As with the previous configuration, this additional lateral force component must be taken into account when solving the calibration coefficient equations.

The corresponding voltage values are collected and averaged, since multiple acquisition are performed for a single test. The resulting values obtained are presented in the next table:

Table 3.2: *Balance calibration values*

	1	**2**	**3**	**4**	**5**	**6**
$V1\ (V)$	0.493	-4.904	-0.058	-0.004	0.050	-0.031
$V2\ (V)$	-0.028	0.261	0.002	-0.375	-0.112	-2.084
$V3\ (V)$	0.579	2.265	0.044	-0.048	-4.942	-0.147
$V4\ (V)$	-0.033	-0.142	0.225	0.049	0.289	-1.578
$V5\ (V)$	0.540	2.623	0.027	0.051	4.737	0.023
$V6\ (V)$	0.000	0.040	-0.232	0.051	-0.022	-1.645
$F_X\ (kgf)$	0	0	1.977	0	0	0
$F_Y\ (kgf)$	0	0	0	-2.014	0	-1.975
$F_Z\ (kgf)$	10.450	0	0	0	0	0
$M_X\ (kgm)$	0	0	0	0	2.090	0
$M_Y\ (kgm)$	0	2.006	0	0	0	0
$M_Z\ (kgm)$	0	0	0	-0.030	0	-0.778

The parameters listed in Tab.3.2 are used to generate the linear system. Specifically, each element of the column vector $\{F\}$ is a load, and every six rows contain those applied in a specific test. The voltages are organized in a matrix: the first row contains, in the first six columns, the voltages related to the first test, on the second row the same voltages are written starting from the seventh column, and so on until the seventh row, where the same procedure is carried out with the voltages of the second test. A 36x36 matrix is assembled, then its inverse matrix is multiplied by the loads vector, to obtain an unraveled coefficient matrix in the form of a column vector. The latter is transposed and reshaped, with the elements positioned in a different row six at a time.

3.2.2 Tare

Balance measurements are significantly influenced by the model's weight during tests involving a variable angle of attack α. The balance reference frame rotates with the model and the gravity vector projects different components onto the balance axes as α changes. Specifically, as the angle increases, the normal component of the weight decreases and another component is generated along the balance x-axis. Furthermore, a pitching moment arises due to the offset between the model's center of gravity and the balance calibration center, which also varies with α. These **gravity-induced loads** must be accurately determined and subtracted from the raw measurements to determine the aerodynamic contributions to be transported to the center of gravity.

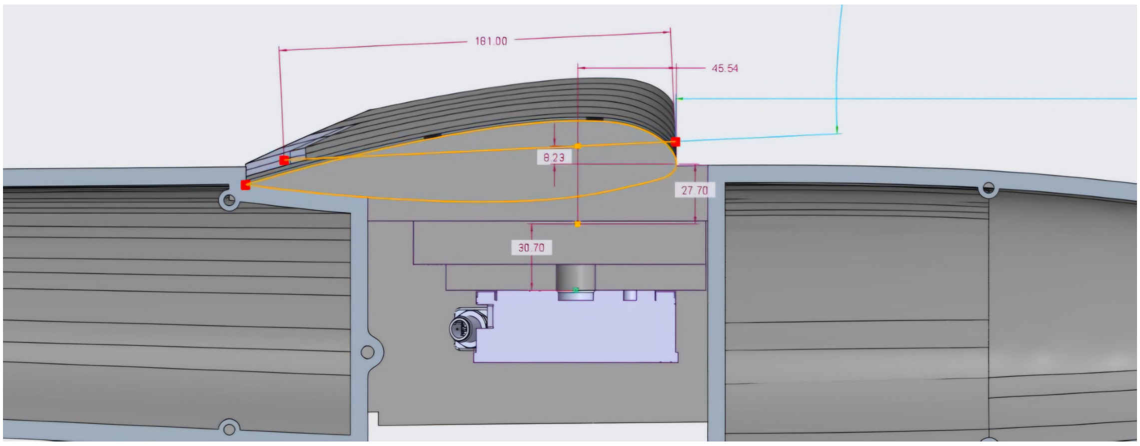

Figure 3.20: *From top to bottom: aerodynamic center of the mean chord, center of gravity and center of the balance (green)*

The procedure consists in a **wind-off test** to acquire the static loads in a suitable range of angles of attack, often corresponding to the ones at which the model will be tested. Tare weight is performed for every configuration of the aircraft, considering also the influence of flap extension and elevator and rudder deflections. The acquisition and processing of the data required for the tare weight are integrated directly into the wind tunnel control software, which automatically performs an interpolation of the wind-off measurements to determine the coefficients of a second-order polynomial function for F_X, F_Z, and M_Y.

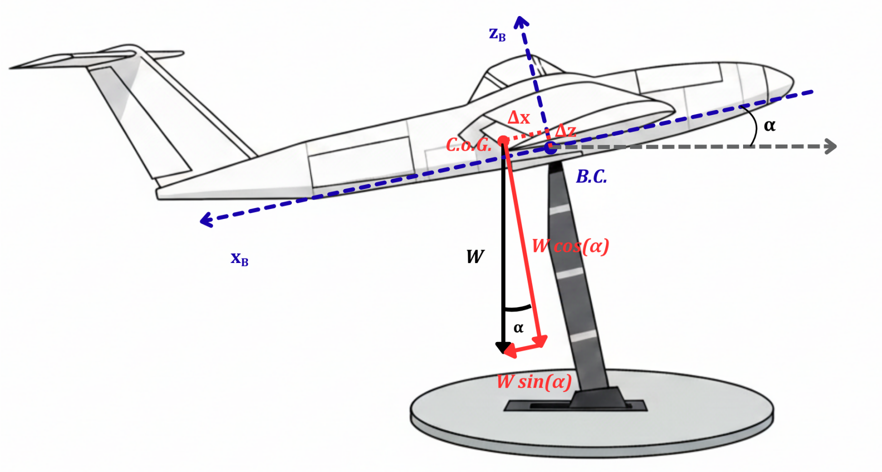

Figure 3.21: *Gravity induced loads*

A total of nine coefficients are identified and exported to a configuration file; these are subsequently loaded before the test to enable real-time compensation of the weight-induced loads. In fact, knowing the geometric angle at which the model is set, forces and moment due to weight are calculated from the interpolation. The tare moment and forces are directly subtracted from the balance measurements.

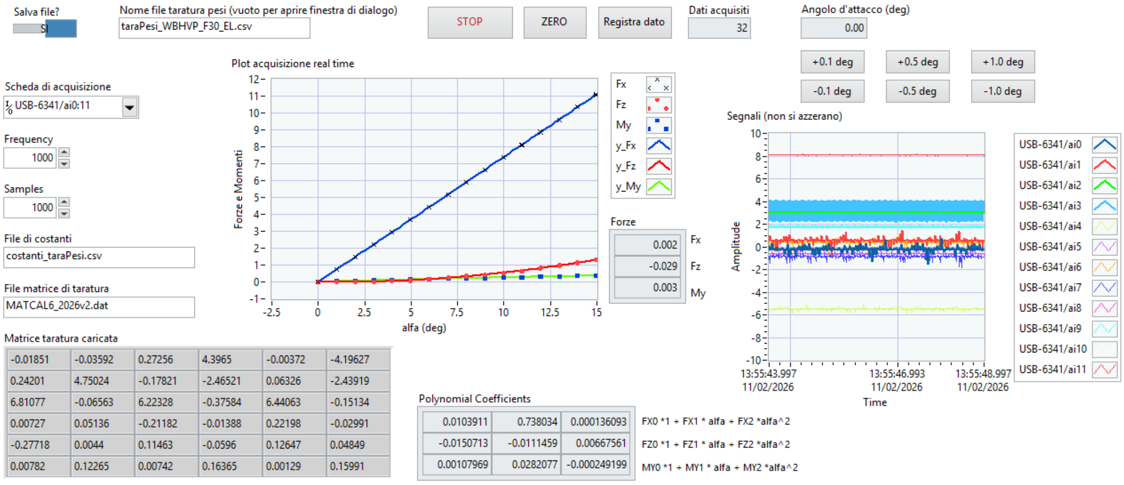

Salva file? SI

Nome file taratura pesi (vuoto per aprire finestra di dialogo): taraPesi_WBHVP_F30_EL.csv

Dati acquisiti: 32

Angolo d'attacco (deg): 0.00

Scheda di acquisizione: USB-6341/ai0:11

Frequency: 1000

Samples: 1000

File di costanti: costanti_taraPesi.csv

File matrice di taratura: MATCAL6_2026v2.dat

Forze:
0.002 Fx
-0.029 Fz
0.003 My

Matrice taratura caricata

-0.01851	-0.03592	0.27256	4.3965	-0.00372	-4.19627
0.24201	4.75024	-0.17821	-2.46521	0.06326	-2.43919
6.81077	-0.06563	6.22328	-0.37584	6.44063	-0.15134
0.00727	0.05136	-0.21182	-0.01388	0.22198	-0.02991
-0.27718	0.0044	0.11463	-0.0596	0.12647	0.04849
0.00782	0.12265	0.00742	0.16365	0.00129	0.15991

Polynomial Coefficients

0.0103911	0.738034	0.000136093	FX0 *1 + FX1 * alfa + FX2 *alfa^2
-0.0150713	-0.0111459	0.00667561	FZ0 *1 + FZ1 * alfa + FZ2 *alfa^2
0.00107969	0.0282077	-0.000249199	MY0 *1 + MY1 * alfa + MY2 *alfa^2

Figure 3.22: *Tare weight software*

Chapter 4

Experimental campaign

A crucial aspect of the investigations carried out in wind tunnels is the breakdown of the aerodynamic properties of the different components of the aircraft. This chapter focuses on the test matrix, including the different layouts of the model, kinematic and flow parameters such as the range of angles of attack and Reynolds number, as well as the model setup for flow visualization. The order of the tests has been dictated by the different phases of the flight envelope, considering cruise, landing and take-off, highlighting the influence of control surfaces (elevator and rudder) on the loads acting on the aircraft model.

4.1 Tested configurations

The test schedule followed both build-down and build-up approaches: starting from the complete model, tests were performed progressively removing components until all configurations in a specific flight condition (cruise, take-off, landing) had been explored; subsequently, tests relative to next flight phase were conducted following a build-up approach. The process is repeated until completion of experimental campaign. The transition between flight phases has been dictated by changing the wing flap incidence, starting from flap retracted, switching to 30° for landing and 20° for take-off.

The tested configurations are:

- **Complete model**: ensures the analysis of the global aerodynamic coefficients, longitudinal and lateral-directional stability and control. Tests were performed for all three flap angles, alternating different deflections of surfaces and combining longitudinal and directional control;

Figure 4.1: *Complete model configuration (flaps cruise)*

Figure 4.2: *Complete model configuration, $\delta_e = -10°$ (flaps take-off)*

- **Wing-body-vertical**: adopted to study the effect of the vertical tail on lateral-directional stability without influence of the horizontal tail. Tests were carried out with different deflections of the rudder; combining this with the complete model allows to isolate the contribution of the horizontal stabilizer and elevator;

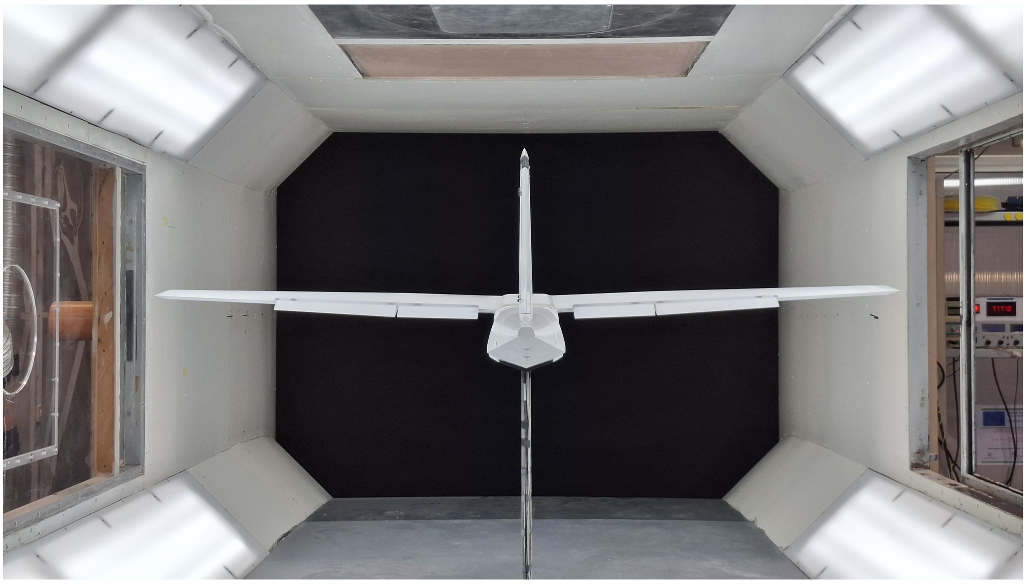

Figure 4.3: *Wing-body-vertical configuration (flaps take-off)*

- **Wing-body**: mainly tested to estimate its contribution to longitudinal and lateral-directional stability compared to configurations including the tail, it is additionally necessary for the calculation of the downwash generated by the wing;

Figure 4.4: *Wing-body configuration (flaps take-off)*

- **Body-horizontal-vertical**: it allows the study of the effect of the isolated tail on stability and control and the variations of effectiveness due to the wing. Together with the wing body and body configuration, it ensures the estimation of the downwash produced by the wing. Tests involved different deflections of control surfaces, accounting for combined effects;

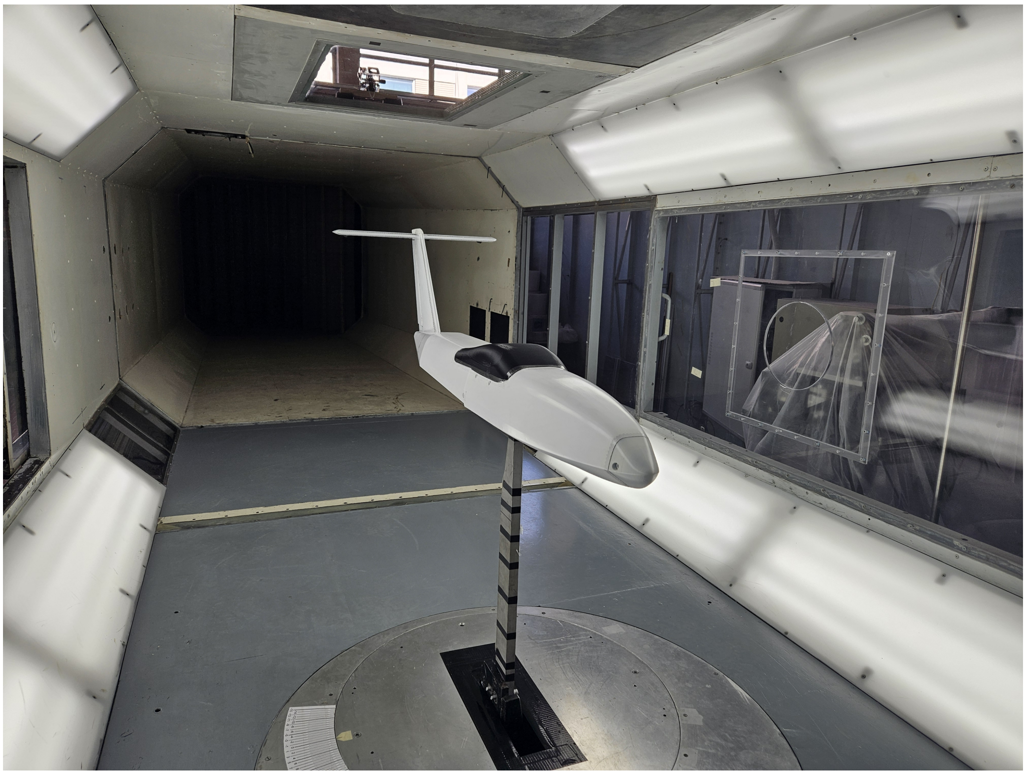

Figure 4.5: *Body-horizontal-vertical configuration.*

- **Body-vertical**: studied for the analysis of the isolated vertical tail performance without the influence of the wing and horizontal tail, tests are also performed with rudder deflection;

Figure 4.6: Body-vertical configuration.

- **Body**: necessary for the estimation of the downwash and for the quantification of the unstable contribution to pitching and yawing moments;

Figure 4.7: Body configuration.

- **Floats configurations**: necessary to analyze the impact of the floats on aircraft performance, these have been tested on the complete model and on wing body configuration.

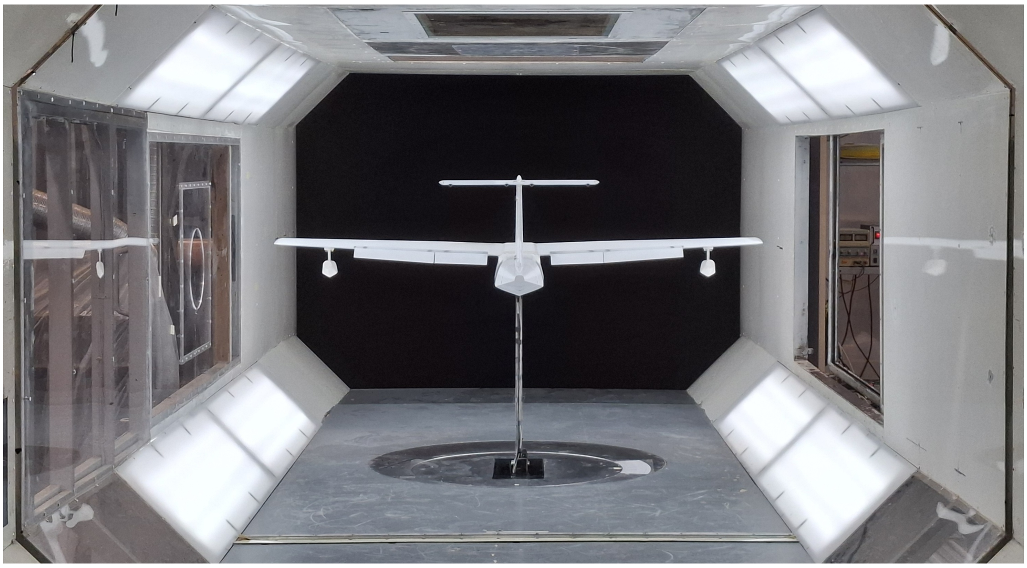

Figure 4.8: *Complete model configuration with floats (flaps landing).*

3D printed components have been produced to assist in the preparation of the model. Support elements for control surfaces and flaps deflection, for example, were made with PLA-Carbon, providing the necessary stiffness to bear the aerodynamic load on the model components.

Figure 4.9: *3D printed flap supports.*

Figure 4.10: *3D printed elevator supports.*

Setups with the isolated vertical tail have been performed using a cap that substitutes the intersection with the horizontal tail. In addition, the wing fairing has been printed to cover the linking area between fuselage and wing, granting a smoother path to the airflow.

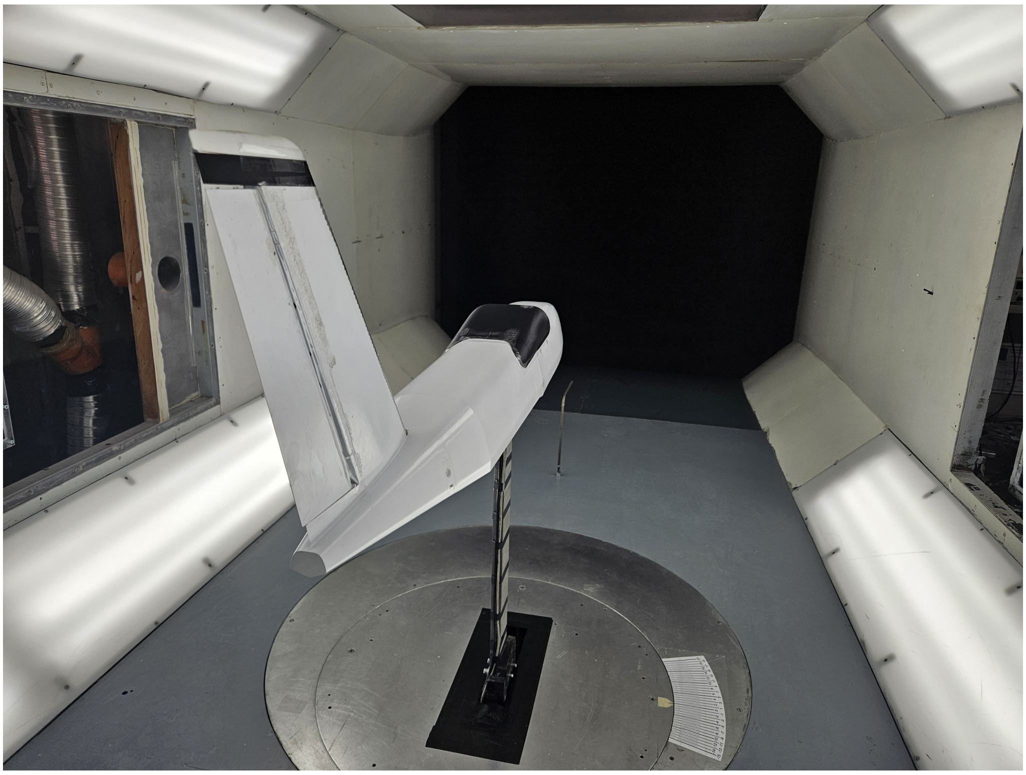

***Figure 4.11:** 3D printed fairing and vertical tail cap.*

4.2 Flow parameters and visualization setup

The test conditions are critical to ensure comparable results during the experimental campaign. To carry out the tests, a velocity of 35 m/s has been selected, ensuring the proper quality of the flow and leading to a Reynolds number of 435000 throughout the tests. A thermocouple positioned inside the testing chamber allowed the measurement of the fluid temperature to account for density and viscosity variations in real time and to monitor the actual Reynolds number. As the latter is particularly low for a seaplane, the overall coefficient values require proper scaling, which is presented in the next chapter, whereas it does not greatly affect the derivatives obtained from the tests. To acquire useful data for the reconstruction of the aircraft behaviour, the angles of attack and sideslip ranges have been selected as $\alpha \in [-1°, 15.5°]$ and $\beta \in [0°, 20°]$. This grants to observe non-linear trends, stall and even post-stall development during longitudinal and lateral-directional evolutions.

A significant portion of the campaign has been dedicated to flow visualization, mostly carried out with wool tufts directly applied on the surface of the model. Wool tufts are a common choice for understanding the aerodynamic behaviour of the air as they are cost-effective, easy to manage and grant a straightforward interpretation; they do not require complex post-processing or particular acquisition devices as they are clearly visible, if a color with the correct contrast with respect to the model surface is selected. Usually, during flow visualization, acquired data regarding forces and moments are not to be trusted, especially with wool tufts. The latter are an invasive visualization technique, as they modify the surface geometry, altering the pressure distribution. In addition, they increase momentum deficit and displacement thickness, particularly harmful in areas with strong adverse pressure gradients. As a consequence, non-linear trends and stall can occur at slightly different angles and lift values, but the macroscopic behaviour is well represented, making wool tufts an effective choice for flow visualization. Recording the tests is good practice, as it allows to analyze different areas of the model avoiding the necessity of multiple or longer runs of the wind tunnel. The choice of the recording device needs careful consideration, as some phenomena could be acquired incorrectly due to the camera frame rate. For this campaign, a frame rate of $60 fps$ was adopted, which demonstrated to be sufficient for the required qualitative assessment of the flow field, even though it could represent a limitation for resolving higher-frequency unsteady phenomena.

Figure 4.12: *Flow visualization with flaps in take-off configuration with* $\delta_r = 10°$

Tufts were extensively employed on wing and tail to properly represent the onset of separation and its spanwise progression on the main surfaces. Furthermore, to investigate the functioning of the slot of the Fowler flaps which contributes to boundary layer re-energization, tufts were positioned on the lower surface of the wing and on the upper surface of the flaps themselves, whereas flow visualization on the fuselage aimed to confirm proper flow reattachment behind the step and verify if separation occurred along the tail cone. On specific occasions, an external longer tuft was employed to visualize flow curvature and wake interactions between the components of the model, as shown in Fig.4.12.

Chapter 5

Post-processing and results

This chapter encompasses the results obtained from the campaign, including visualization and numerical data. Flow visualization experiments are advantageous in providing a qualitative representation of the flow field surrounding the model, allowing the observation of the stall path and particular aerodynamic phenomena, useful for correlation with numerical methods and explanation of experimental data. Measurements resulting from tests have to be collected and organized to evaluate aerodynamic performance and compare different configurations with numerical simulations. The wind tunnel acquisition system already implements corrections for both boundary and tare effects described in Chapter 3, organizing data in *.txt* files. The output files contain:

- **Flow characteristics**: dynamic pressure, speed and Reynolds number;
- **Aerodynamic angles**: angle of attack and sideslip;
- **Aerodynamic coefficients**: C_L,C_D,C_Y,$C_{\mathcal{L}}$,$C_{\mathcal{M}}$,$C_{\mathcal{N}}$;
- **Additional useful data for post-processing**: C_L^2, E,$\frac{C_L^{3/2}}{C_d}$.

These quantities are used to retrieve graphical representations of the aerodynamic characteristics and calculate the necessary parameters for the performance evaluation. Particular attention is paid to the longitudinal and lateral-directional stability and control, as well as the lifting capabilities and drag.

Wind tunnel testing on a scaled model, as explained in the previous chapters, suffers the difficulty of matching the real Reynolds number of the full scale aircraft, meaning the measurement is carried out in a different flow compared to the operative condition. Scaling the results to the operating Reynolds number is necessary for the values that are most affected by it, which are the maximum lift coefficient and the drag coefficient.

5.1 Flow visualization

Following the introduction to flow visualization in the previous chapter, in this section the stall path is presented for all three flight conditions, considering the corrected angle of attack. Furthermore, useful insights are shown for the interpretation of quantitative data to verify the hypotheses.

5.1.1 *Stall paths*

Cruise stall path

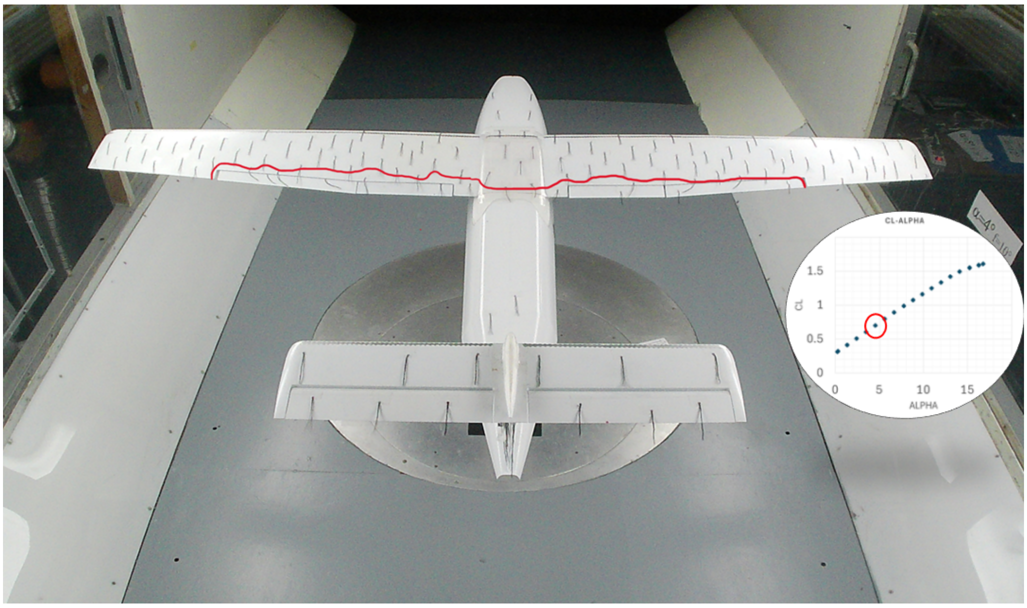

Figure 5.1: *Flow visualization (flaps* 0°*):* α = 4.5°

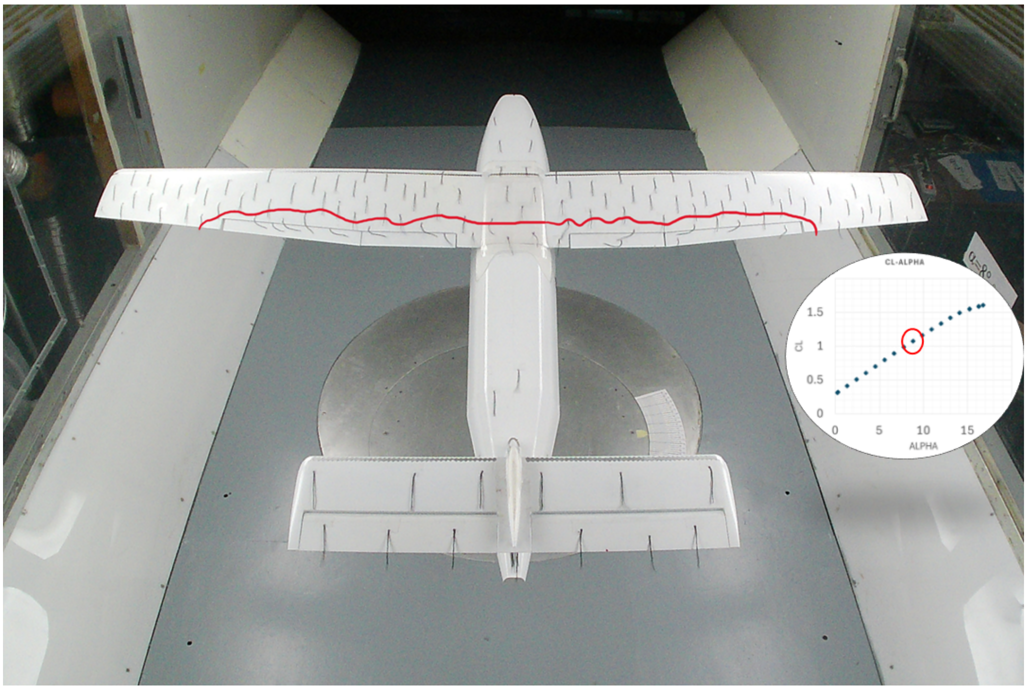

Figure 5.2: *Flow visualization (flaps* 0°*):* α = 8.8°

With flaps retracted flow remains attached throughout the wing, with a small wake confined at the flaps, caused by surface discontinuity. The root of the wing is characterized by increased turbulence due to interference between the boundary layers of the fairing and the wing.

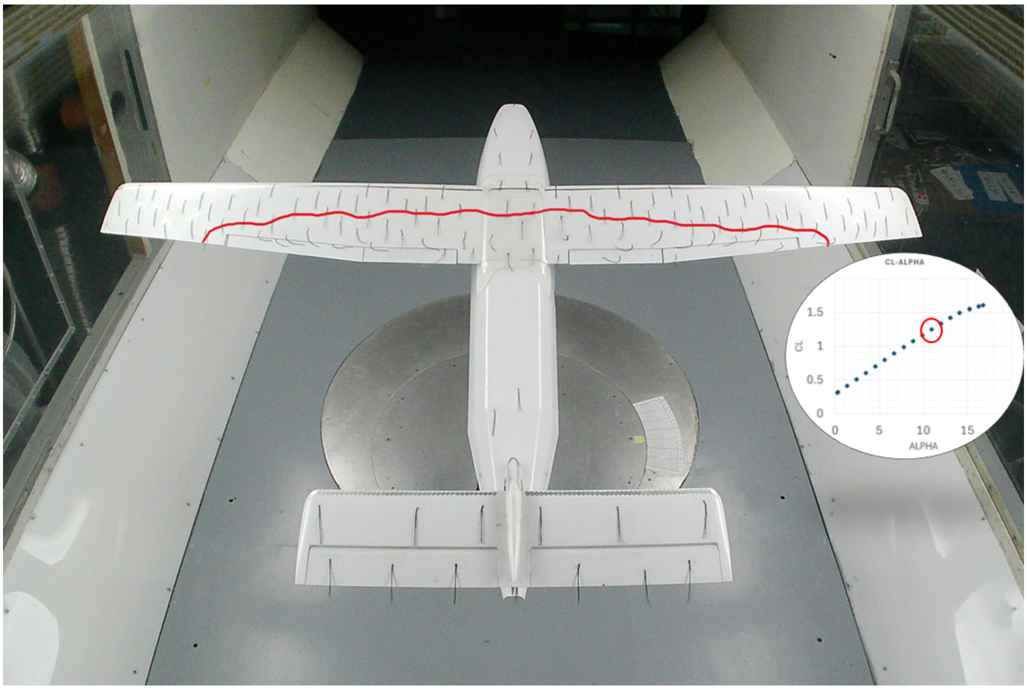

Figure 5.3: *Flow visualization (flaps* 0°*):* α = 10.9°

At 10.9° reverse flow becomes visible near the trailing edge of the root section and the wake on the flaps begins to move up.

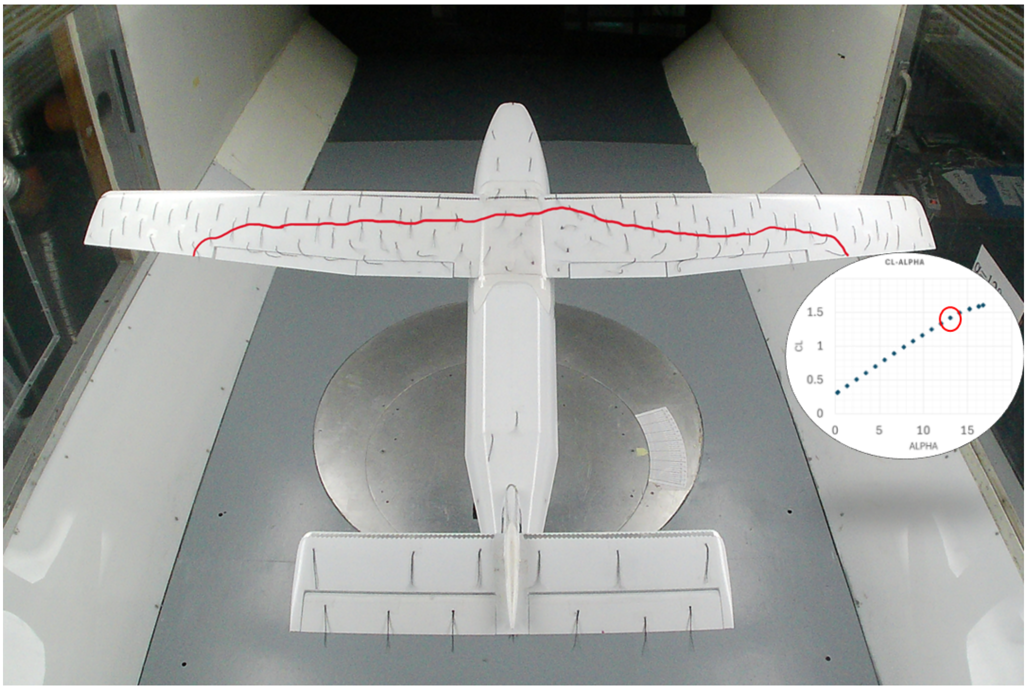

Figure 5.4: *Flow visualization (flaps* 0°*):* α = 13.0°

At 13.0° the wing clearly shows separation starting from the root sections, with reversed flow from the middle of the fairing to the inner flap. Strong flow convergence and fluctuations can be spotted throughout the span until the ailerons section.

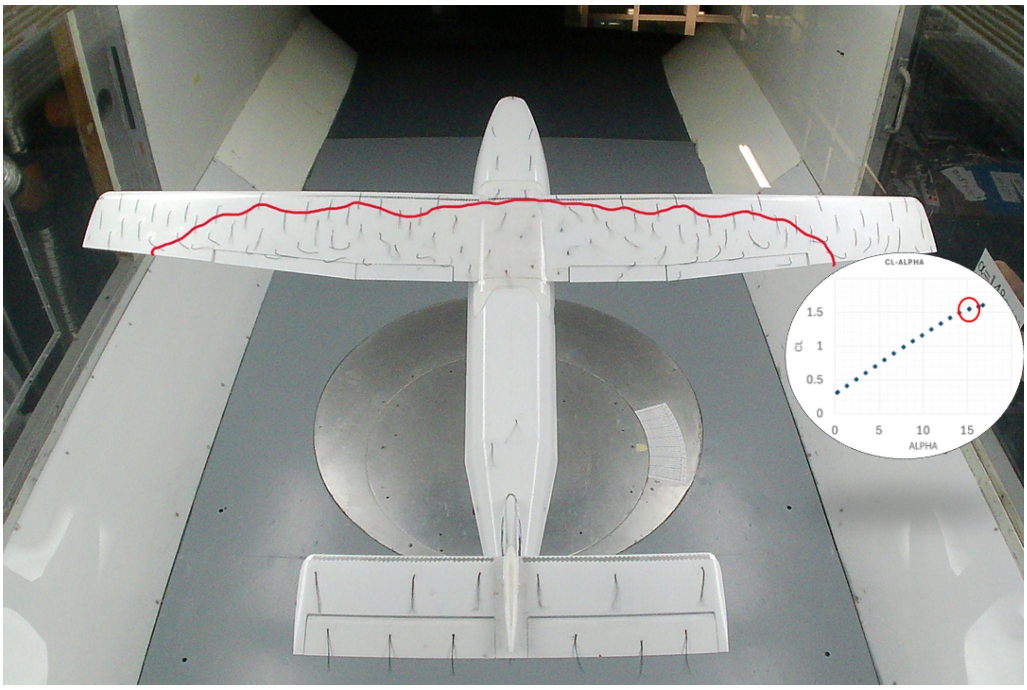

Figure 5.5: Flow visualization (flaps $0°$*):* $\alpha = 15.2°$

Increasing the angle of attack by 2°, expands the zone affected by reverse flow, which now completely includes the first flap. Increased fluctuations are felt even near the earliest chord sections, as well as at the base of the tail cone and at the elevator, but no strong separation can be spotted on the latter, which is still able to control the pitching moment.

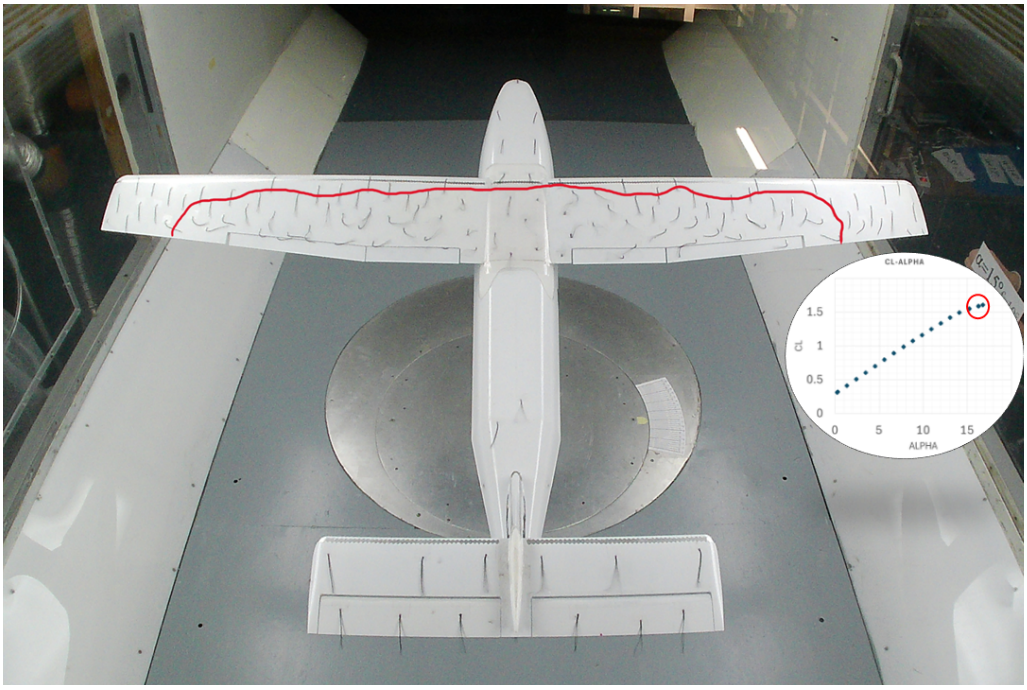

Figure 5.6: Flow visualization (flaps $0°$*):* $\alpha = 16.8°$

At 16.8°, reverse flow begins to affect the outer flaps, whereas on the outer sections of the span no separation occurs, ensuring lateral control.

Take-off stall path

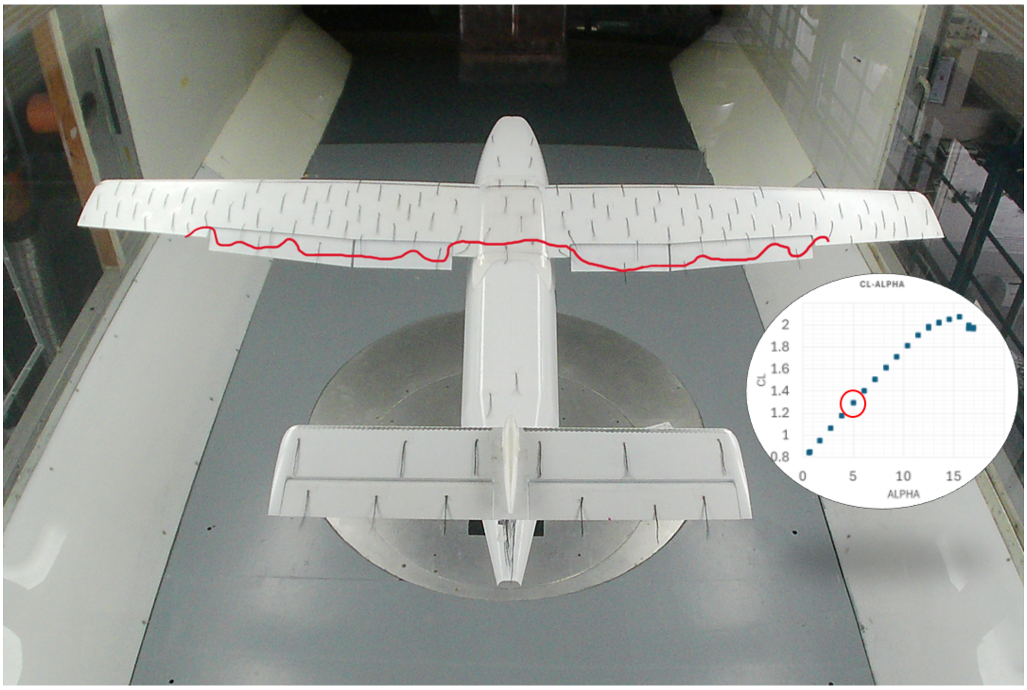

Figure 5.7: *Flow visualization (flaps* 20°*):* α = 5°

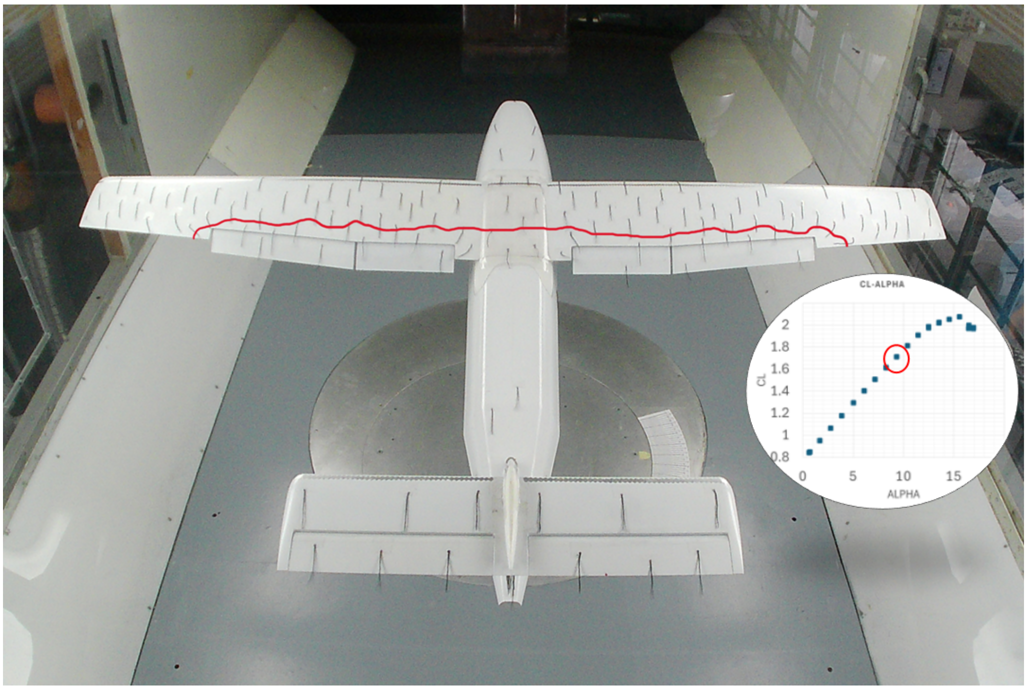

Figure 5.8: *Flow visualization (flaps* 20°*):* α = 9.3°

Considering the flaps deflected by 20°, the effect of their tip vortices can be noticed, with flow converging towards the flaps both at the root and the tip of the wing. Until $\alpha = 5.0°$, flow remains attached on the wing, feeling the beneficial effect of the slot, whereas a wake starts forming on the trailing edge of the flaps. At $\alpha = 9.3°$, the wake shifts on the main wing, with the slot showing proper blowing on the flaps.

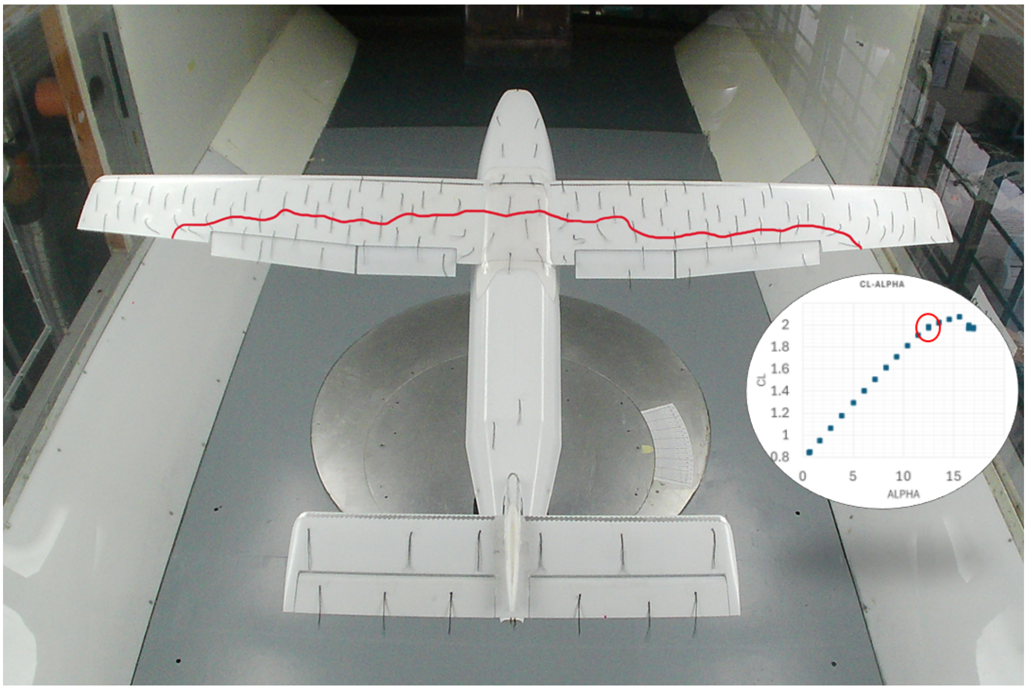

Figure 5.9: *Flow visualization (flaps* 20°*):* $\alpha = 12.5°$

At 12.5°, the inner flap vortex shows a stronger interaction with the root flow, causing a small spot of flow reversal. Velocity fluctuations start to increase on the stabilizer, and separation moves upstream.

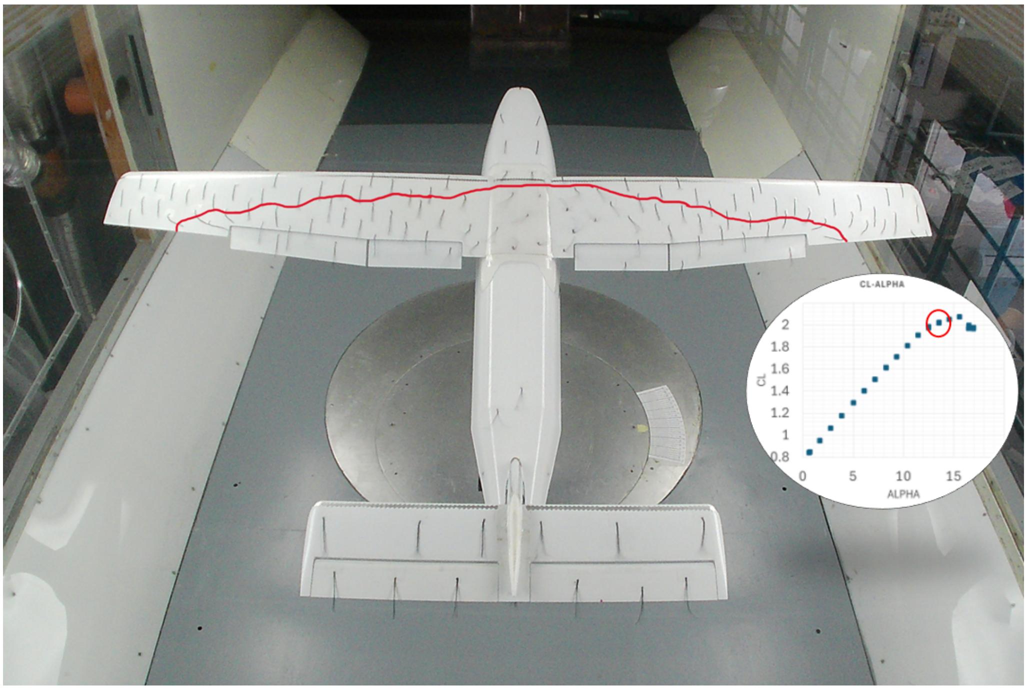

Figure 5.10: *Flow visualization (flaps* 20°*):* $\alpha = 13.5°$

Increasing the angle by 1° causes the reversal flow spot to burst, engaging the fairing and root sections and reaching the middle of the first flap. Separation again affects the rest of the wing and tail cone, showing increased swinging of the tufts.

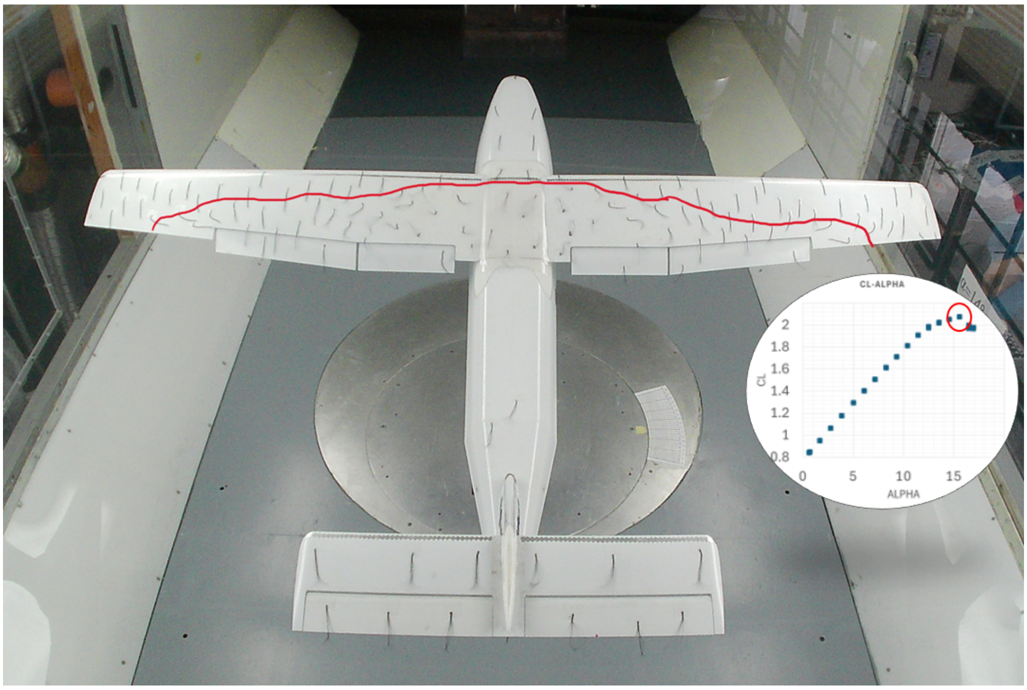

Figure 5.11: *Flow visualization (flaps* 20°*):* α = 15.6°

Taking into account 2° more, the reversed region reaches the locations, at the trailing edge, involved in the same phenomenon with retracted flaps at 16.8°, but with a wider zone upstream, mid-wing. The tail still grants longitudinal control, even if turbulent fluctuations become higher near the root.

Landing stall path

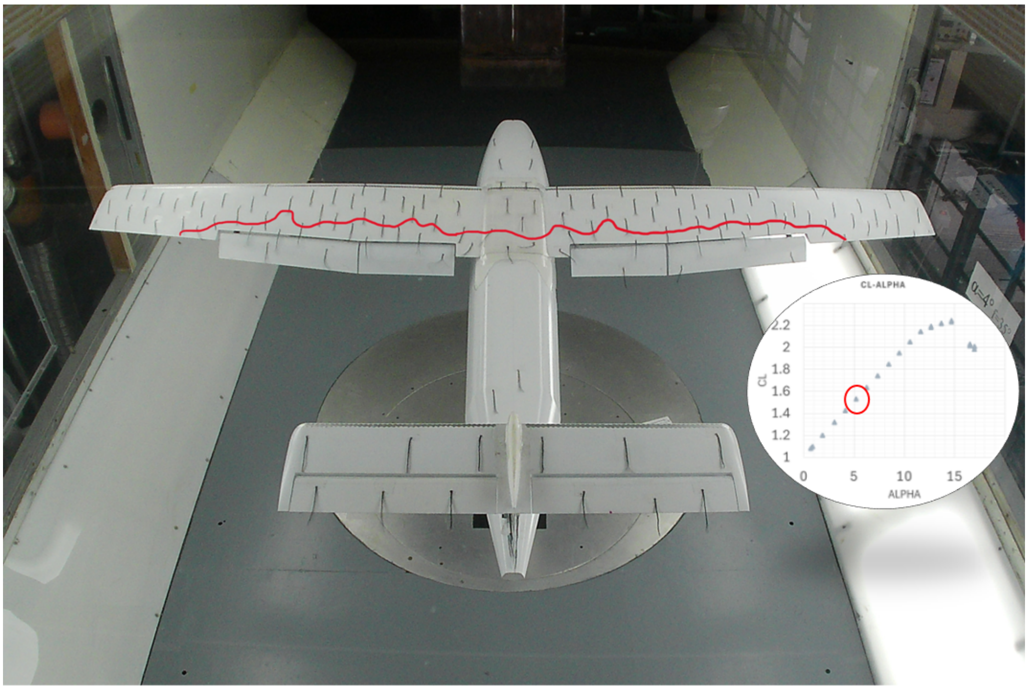

Figure 5.12: Flow visualization (flaps 30°*):* $\alpha = 5.2°$

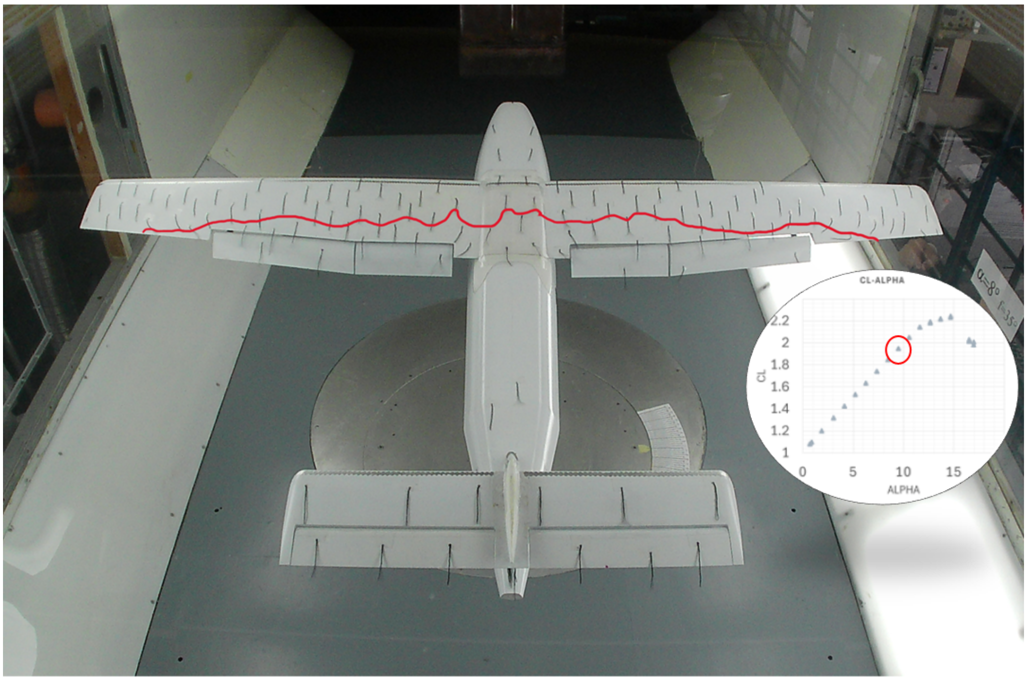

Figure 5.13: Flow visualization (flaps 30°*):* $\alpha = 9.5°$

During landing, the tip vortices of the flaps are more intense: the flow on the wing and even on the fairing is more strongly deflected towards them. The tuft close to the inner tip of the first left flap already experiences the vorticity of the flow even at low incidence. At these angles, the blowing of the slot slightly affects the wing, with a wake forming close to the flap location.

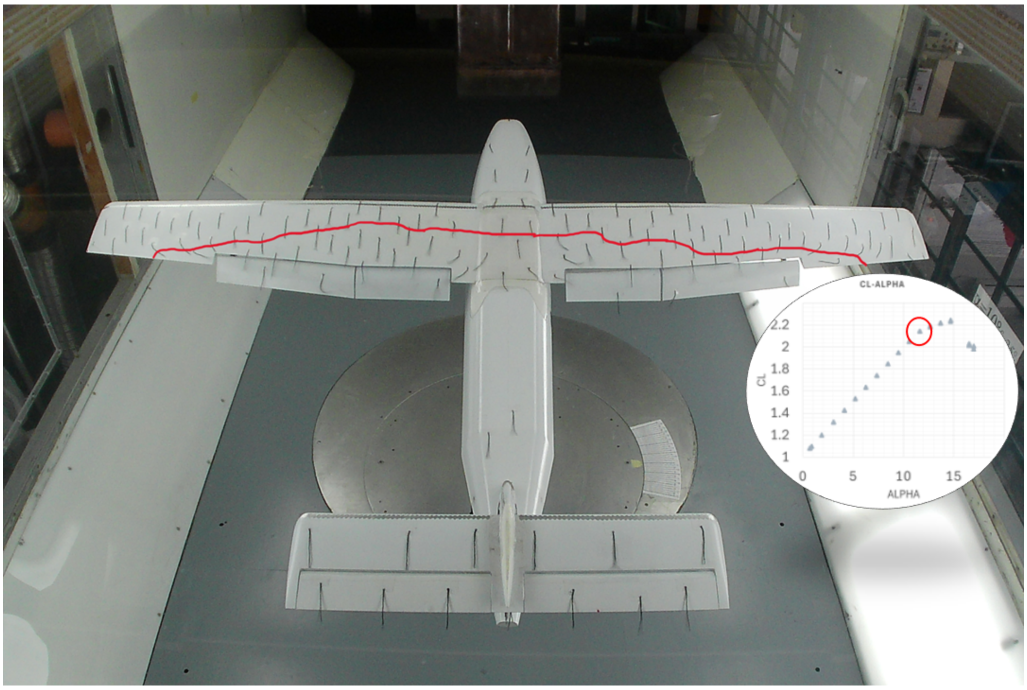

Figure 5.14: *Flow visualization (flaps* 30°*):* α = 11.6°

At 11.6°, separation starts moving upwards, reaching the half of the chord at the inner sections of the wing, and strong fluctuations involve the flaps, which nevertheless still do not show reverse flow.

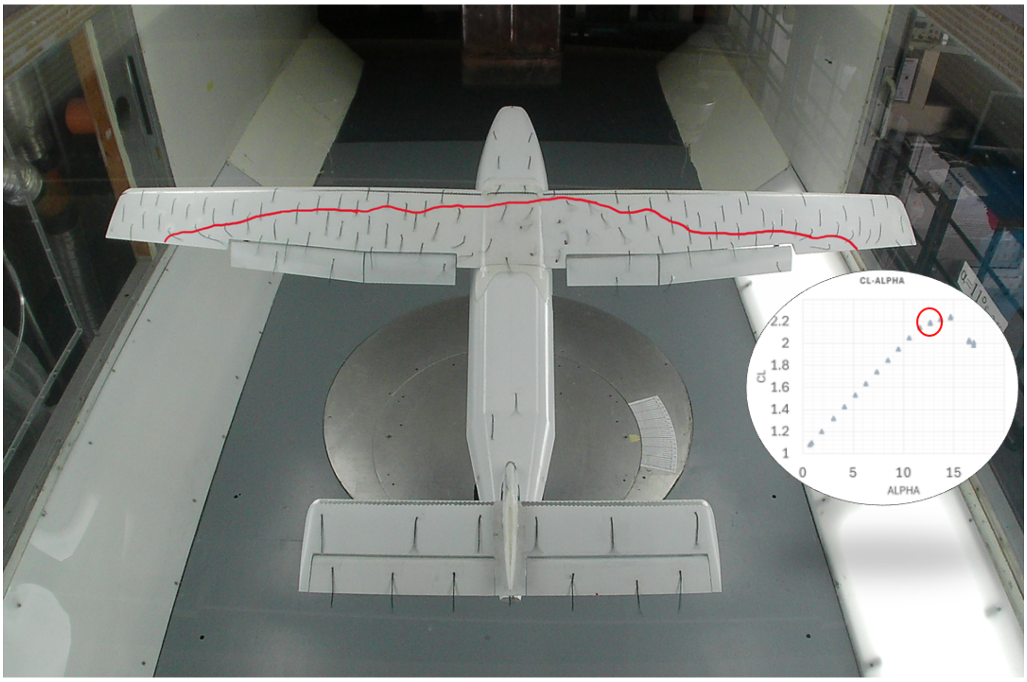

Figure 5.15: *Flow visualization (flaps* 30°*):* α = 12.6°

At $\alpha = 12.6^\circ$, flow reversal abruptly begins at the root of the wing up to the middle of the inner flap, even though the slot grants good quality flow above the latter, excluding it from this phenomenon.

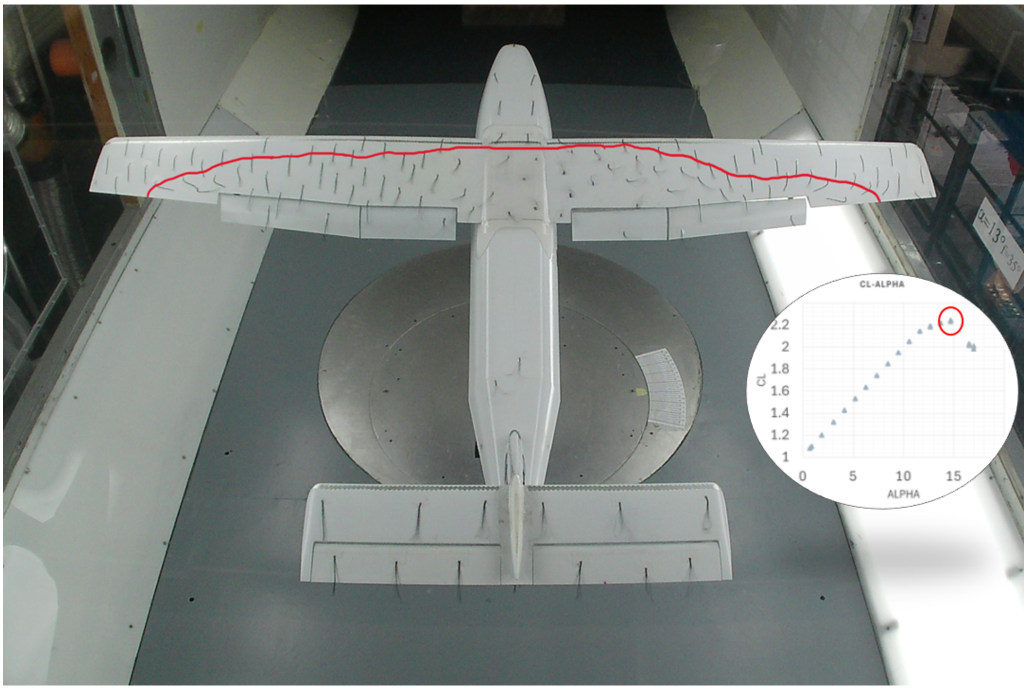

Figure 5.16: *Flow visualization (flaps* 30°*):* $\alpha = 14.7^\circ$

When 14.7° is reached, the reversed region is wider, reaching the outer flap. Widespread separation can be spotted on the inner flaps. Increased turbulence is felt at the tail cone and the horizontal stabilizer, but the stream can still follow its curvature, granting longitudinal control.
In all three configurations, flow reversal begins at the root sections, preserving the effectiveness of the ailerons, which will be positioned after the second set of flaps, for lateral control.

5.1.2 Observed phenomena

Interaction between flap vortex and root of the vertical tail

To explain the flap effect on directional equilibrium, the downstream propagation of the inner vortex of the first flap has been investigated during flow visualization. The vorticity caused at the section of the fuselage where the vertical stabilizer is mounted is intense, and this clarifies the slight reduction in lateral-directional stability due to flap deflection. In the figures below, the flow convergence towards the elevator is also visible on the rudder, caused by the low pressure on the upper surface of the horizontal tail.

Figure 5.17: *Vorticity at the vertical stabilizer due to flap vortex ($\alpha = 5°$, $\beta = 10°$, flaps 30°)*

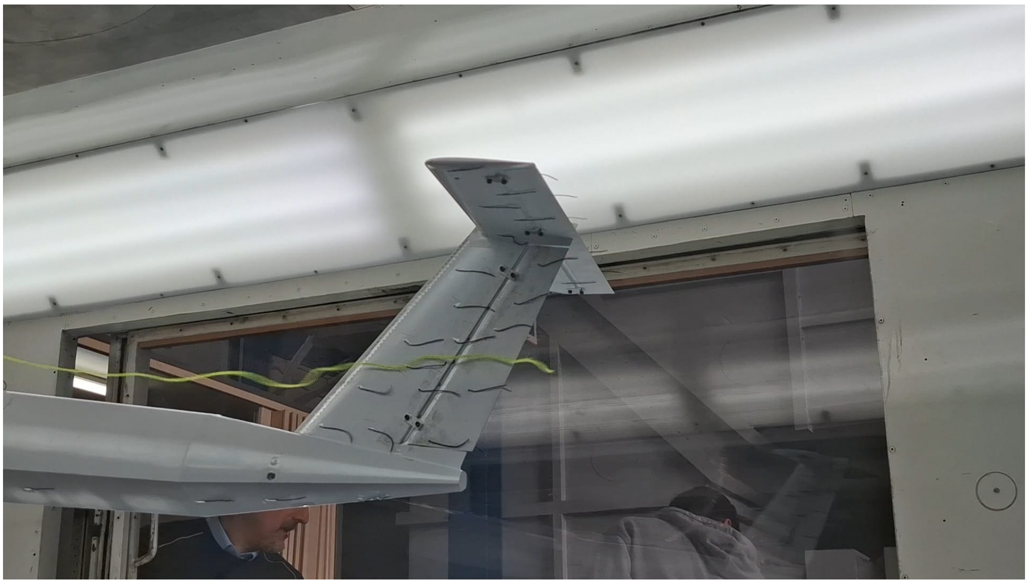

Figure 5.18: *Detail of the disturbance at the vertical tail ($\alpha = 5°$, $\beta = 10°$, flaps 30°)*

Flow downstream of the step

The problems caused by the step have been already presented in Chapter 1, in this paragraph their magnitude is visualized. For the tested seaplane, the step causes the predicted separation, even though the flow rapidly reattaches, considering the following tufts and that the second is positioned $12cm$ behind the step, which already shows only a slight oscillation of the tip. This means that at the lower angles, the worst condition for the flow in this region, air is able to reattach even with increased velocity fluctuations, which get

progressively damped due to the expansion caused by the first section of the tail cone. This portion of the tail is critical, as it is one of the main contribution to fuselage drag, but even here the flow continues to follow the geometry without separating.
On the upper side, as shown in the pictures regarding the stall path, flow is affected by the wake coming from the fairing, but it does not experience a strong separation at the tail cone.

Figure 5.19: *Flow visualization behind the step (α = 0°, β = 0°, flaps 20°)*

Slot effectiveness

The slot between the flaps and the wing is a complicated feature to scale to testing dimensions, and hence its effectiveness is investigated. From the high pressure side, tufts bend towards the slot itself, allowing to visualize the correct path followed by the air. Another important indication of its effectiveness is represented by Fig. 5.15, which shows attached flow on the flap even with separation and intense velocity fluctuations above the upstream section of the wing.

Figure 5.20: Tufts bending towards the slot of the flaps (flaps 20°*)*

Stream curvature and downwash

The camber of the airfoils used for the wing, paired with the angle of attack and the Coanda effect, generates a downward rotation of the velocity vector, a critical acceleration to generate lift. In the picture below, the curvature imposed by wing and fairing geometries is clearly visible. Considering that the wind tunnel is designed to minimize the angle of incidence of the air inside the test chamber, and hence that the flow is horizontal upstream of the model, the longer tuft allows one to see first-hand the downwash felt at the tail, which will be quantified in the next section.

Figure 5.21: Visualization of the downwash caused by wing circulation ($\alpha = 10°$, $\beta = 0°$, flaps 0°*)*

5.2 Longitudinal coefficients, stability and control

Longitudinal tests analyze the aerodynamic behaviour of the aircraft with respect to the angle of attack. In particular, longitudinal stability and control characteristics are examined, as well as lifting capabilities and drag. Stability in general is the tendency of the aircraft to return to its original equilibrium condition after being subjected to a perturbation. Regarding longitudinal stability, a stable aircraft subjected to a perturbation of the angle of attack generates a pitching moment which tends to restore the original equilibrium condition. This behaviour is defined by the pitching moment derivative $C_{\mathcal{M}_\alpha}$, which indicates how fast the pitching moment, measured with respect to the center of gravity, changes with the angle of attack; a stable behavior is indicated by $C_{\mathcal{M}_\alpha} < 0$.
The main components impacting longitudinal equilibrium are the wing, the horizontal tail, the fuselage and the engines.
The equation that expresses the longitudinal stability is derived from the pitching moment equilibrium with respect to the center of gravity, in which the propulsive contribution is neglected. To account for the effect of the fuselage, the aerodynamic center of the wing-body configuration is used as application point of the lift of the wing. Deriving with respect to the angle of attack we obtain:

$$C_{\mathcal{M}_\alpha} = C_{L_{\alpha,w}} \left(\frac{x_{cg} - x_{ac,wb}}{c}\right) - \eta_h V_h C_{L_{\alpha,h}} \left(1 - \frac{d\epsilon}{d\alpha}\right) \tag{5.1}$$

where c is the mean aerodynamic chord of the aircraft, η_h is the dynamic pressure ratio at the horizontal tail, V_h is the volumetric coefficient of the horizontal tail and $\frac{d\epsilon}{d\alpha}$ is the downwash derivative. The tests on different configurations enable the study of the effect of specific components on longitudinal equilibrium and the downwash calculation.
Flap deflection not only affects lift and drag but also contributes to stability. The main contribution of the elevator is to ensure the necessary longitudinal control authority to the aircraft, but its effect on lift and drag have been investigated as well. These studies include the measurements of maximum lift coefficient, drag polar for different aircraft configurations and efficiency. In addition, lift and pitching moment slopes as well as Oswald efficiency factor have been calculated considering $\alpha \in [1°, 8°]$, completing the longitudinal analysis.

5.2.1 Test results

Configurations effect

Aerodynamic characteristics of different components of the model are highlighted in the following figures. In particular, several configurations are presented:

- Body (B);

- Body-vertical (BV);
- Body-horizontal-vertical (BHV);
- Wing-body (WB);
- Wing-body-vertical (WBV);
- Complete model (WBHV);

The comparison between different configurations is performed with flaps retracted and control surfaces in neutral position. The plot of the lift coefficient is presented in Fig. 5.22: the main contribution to the overall lift is given by the wing, followed by the horizontal tail which has an increasing effect on the lift slope respect to the wing-body configuration. Fuselage and vertical tail contribution on lift is negligible.

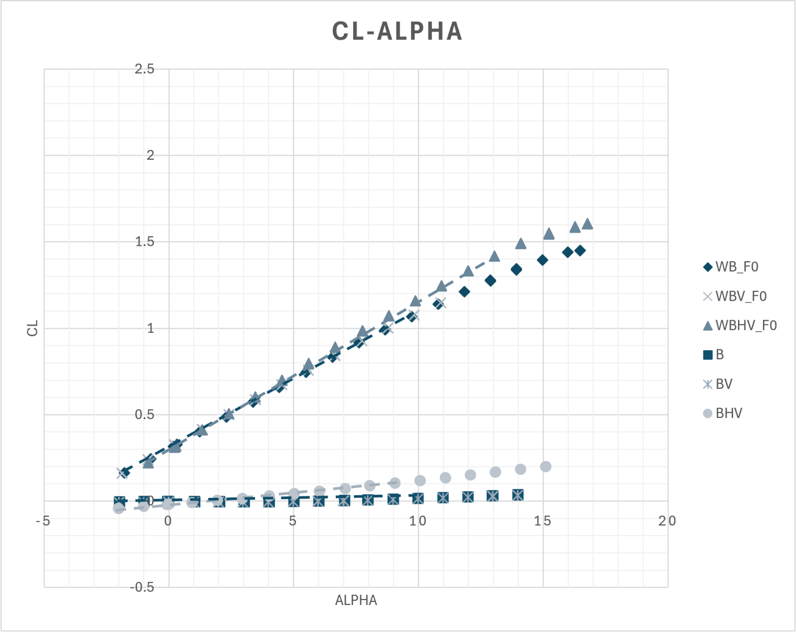

Figure 5.22: *C_L versus α for different model configurations.*

The curves show a linear behavior for a wide range of angles of attack, hence in this range the evaluation of the C_{L_α} derivative for the different configurations is straightforward. The pitching moment curves are interesting for the evaluation of the contribution of the various elements to longitudinal stability: the fuselage and the wing produce an unstable pitching moment with respect to the angle of attack, meanwhile configuration with horizontal tail exhibit a stable behaviour.

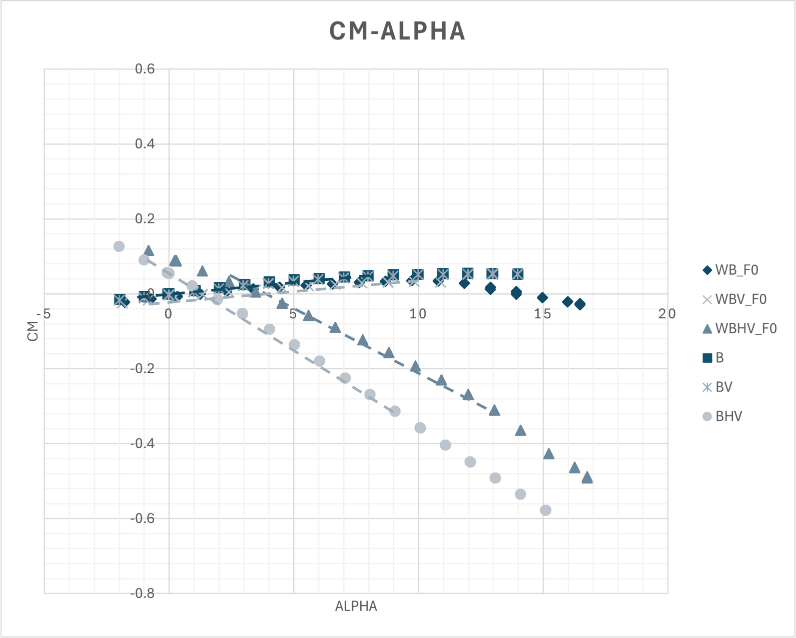

Figure 5.23: $C_{\mathcal{M}}$ *versus* α *for different model configurations.*

Similar to the $C_{\mathcal{M}}$ versus α curves, the $C_{\mathcal{M}}$ versus C_L shows the contributions to the longitudinal stability of the components of the aircraft. The difference in lift generation can be noticed between configurations with and without the wing. Of particular interest is the evaluation of the $C_{\mathcal{M}_{C_L}}$ derivative, fundamental to estimate the Static Stability Margin.

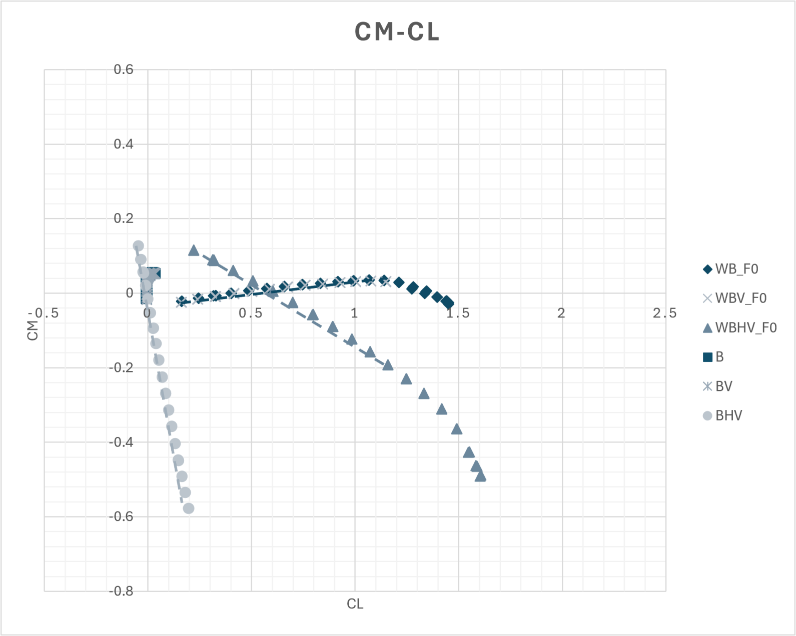

Figure 5.24: $C_{\mathcal{M}}$ *versus* C_L *for different model configurations.*

Drag curves are showed in Figures 5.25 and 5.26: drag variation with respect to lift coefficient is clearly visible for the complete model, wing-body and Wing-body-vertical configurations.

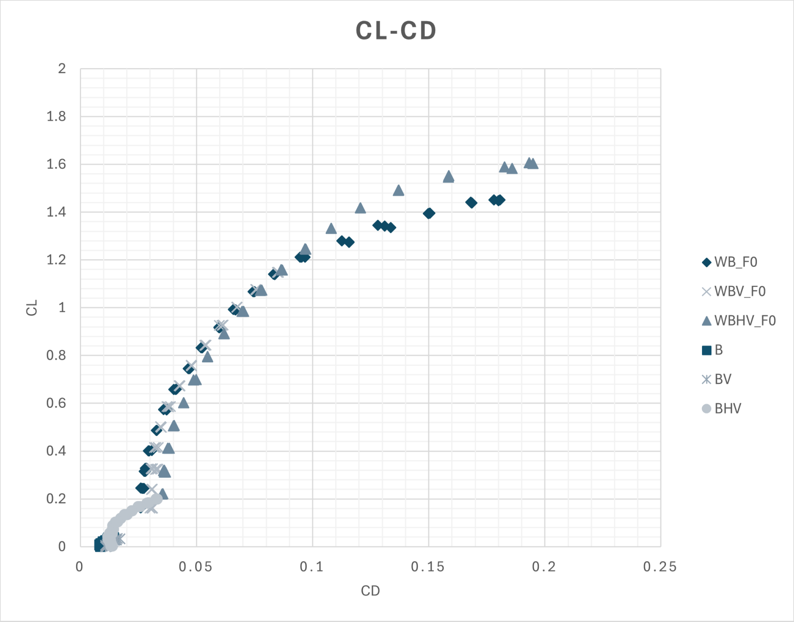

Figure 5.25: C_L *versus* C_D *for different model configurations.*

The vertical tail, as expected, gives an additional parasite drag contribution due to the increasing wet surface and the generated wake, as highlighted by the offset between wing-body and wing-body-vertical drag curves, which is limited to the low C_L range.

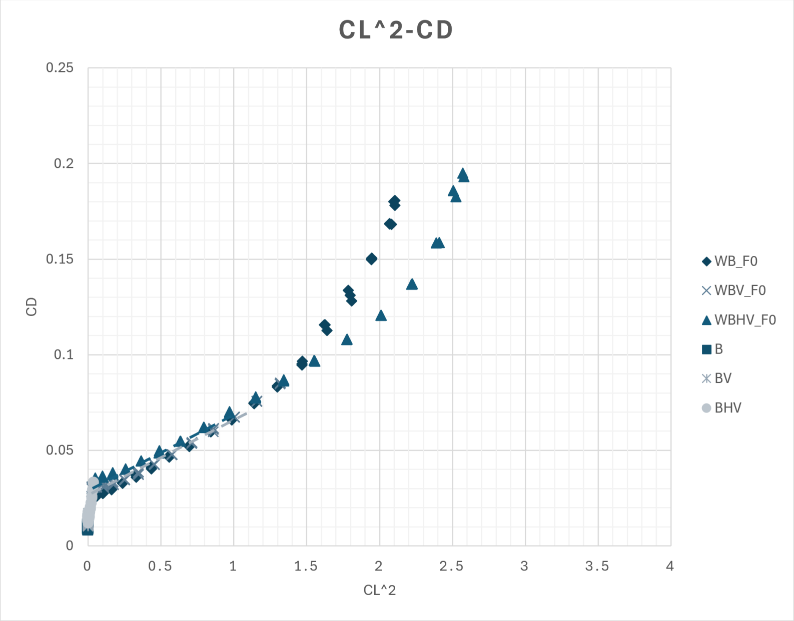

Figure 5.26: C_D *versus* C_L^2 *for different model configurations.*

Plotting C_D versus C_L^2 allows to evaluate the Oswald factor and the drag coefficient at zero lift. In fact, considering the linear range of the curves, is possible to evaluate their slope K and the Oswald factor is extracted with the following relation:

$$e = \frac{1}{\pi \cdot AR \cdot K} \tag{5.2}$$

whereas C_{D0} is estimated as the intersection of the linear curve with the vertical axis of the plot.

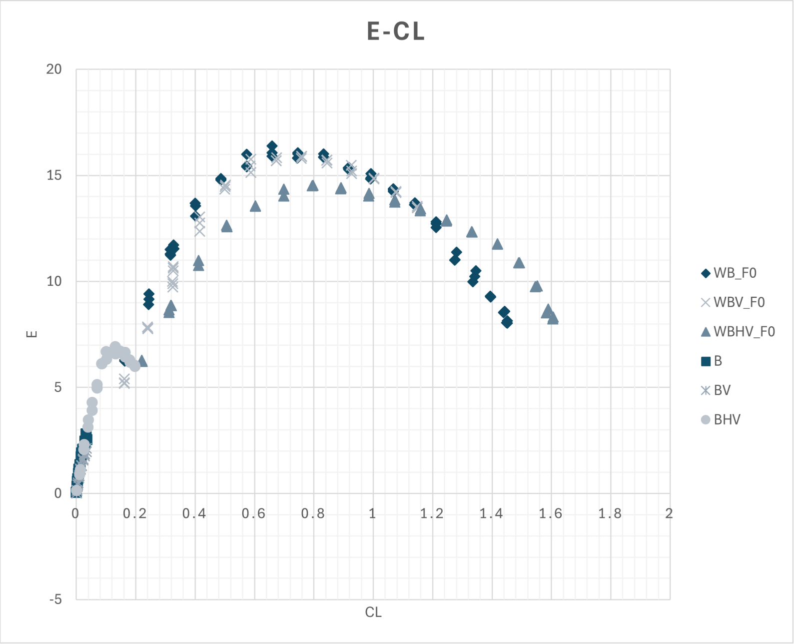

Figure 5.27: *E versus C_L for different model configurations.*

Fig. 5.27 shows the aerodynamic efficiency versus C_L for the different configurations: the complete model presents a lower maximum efficiency compared to the wing-body configurations due to the additional surface of the components and the drag generated by the horizontal tail. Calculated parameters are presented in Tab. 5.1:

	WBHV_F0	**WBV_F0**	**WB_F0**	**BHV**	**BV**	**B**
C_{L_α} $(1/deg)$	0.0895	0.0802	0.0810	0.0135	0.0018	0.0015
C_{L_0}	0.2930	0.3091	0.3005	0.0263	−0.0106	−0.009
$C_{\mathcal{M}_\alpha}$ $(1/deg)$	−0.2870	0.0047	0.0048	−0.041	0.0052	0.0056
$C_{\mathcal{M}_{C_L}}$	−0.3205	0.0586	0.0598	−3.022	–	–
$C_{\mathcal{M}_0}$	0.1960	−0.0244	−0.0228	−0.0126	0.0367	0.0371
C_{D_0}	0.0301	0.0244	0.0224	0.0129	0.0113	0.0091
e	0.8825	0.8570	0.8120	0.2030	–	–

Table 5.1: *Aerodynamic parameters comparison between different configurations*

The horizontal tail increases the lift slope and ensures negative $C_{\mathcal{M}_\alpha}$ and $C_{\mathcal{M}_{C_L}}$, while Body and Wing-Body configurations give an unsettling contribution to the pitching moment slope. The vertical tail does not have significant influence on longitudinal equilibrium, mainly increasing drag. The Oswald efficiency factor of the complete model is about 0.88, a remarkable value mainly due to the wing geometry, with a beneficial effect coming from the tail. As Oswald factor is related to how an aircraft produces lift with respect to an ideal elliptical wing, calculation of this parameter does not have physical meaning without lifting surfaces.

Flaps effect

The impact of the flap deflection on longitudinal equilibrium is examined considering first the Wing-Body configuration and then the complete aircraft model. Aerodynamic performance is evaluated for all flap configurations and presented at the same time to simplify the evaluation of the flap effect itself. The main purpose of flaps is to increase the lift coefficient compared to clean configuration, an effect which is illustrated in Fig. 5.28 for the Wing-Body configuration. $C_{L,max}$ is increased from 1.45 in cruise to 1.92 with flaps at 20° and to 2.09 for landing flaps. Additional effects on lift include the slight increment of slope at the expenses of the stall angle, which decreases.

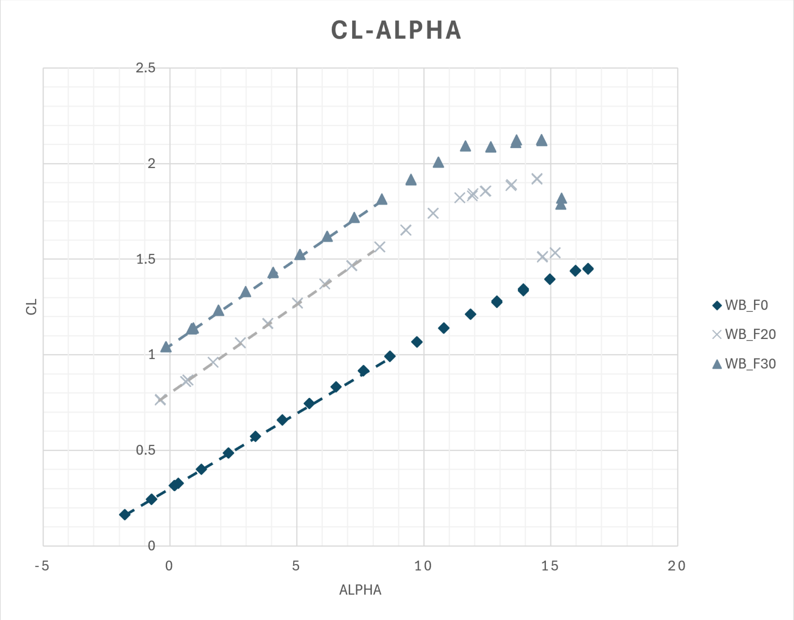

Figure 5.28: Wing-Body configuration: C_L versus α for different flap deflections.

Pitching moment is influenced by flap deflection trough the shifting of the curve towards negative values. The deployment of flaps also modifies the position of the aerodynamic center of the wing, shifting it towards the trailing edge. In the Wing-Body configuration, the aerodynamic center shifts near the center of gravity defined for the complete aircraft, which is the reduction pole adopted for the measurements, leading to an almost zero C_{M_α}.

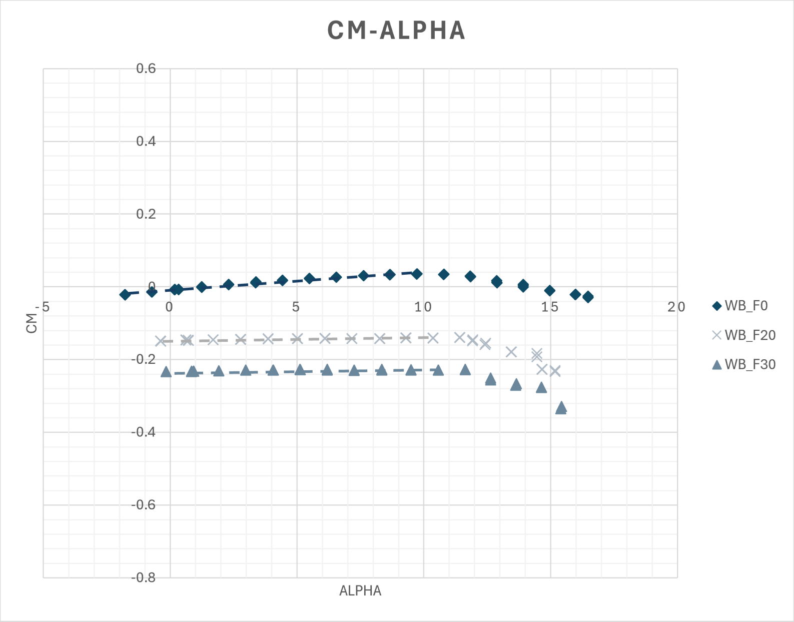

Figure 5.29: *Wing-Body configuration: C_M versus α for different flap deflections.*

The same considerations can be retrieved from the C_M versus C_L curves in Fig. 5.30, in which the translation along the horizontal axis is a consequence of the increased lift generated by the deflection of the flaps.

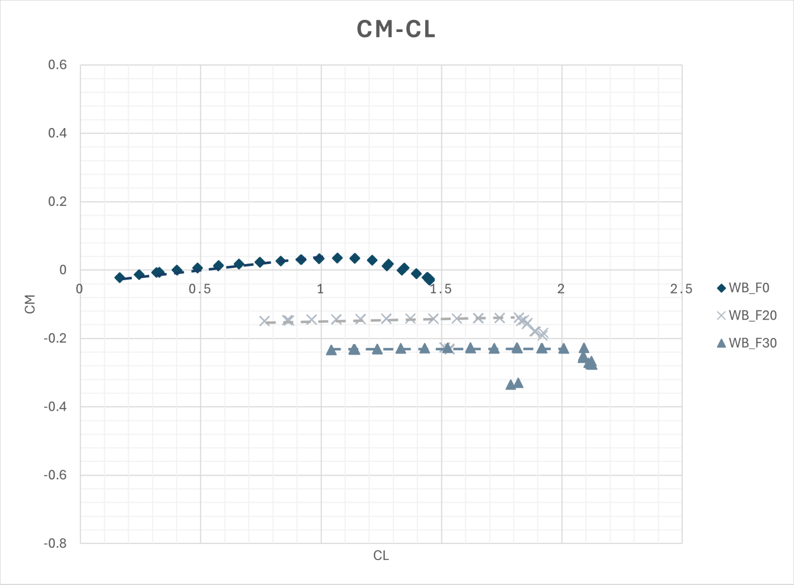

Figure 5.30: *Wing-Body configuration: C_M versus C_L for different flap deflections.*

The increase in drag is highlighted in Fig. 5.31: the higher lift produced by flaps generates greater induced drag and the exposed surface due to the extension generates additional parasite drag.

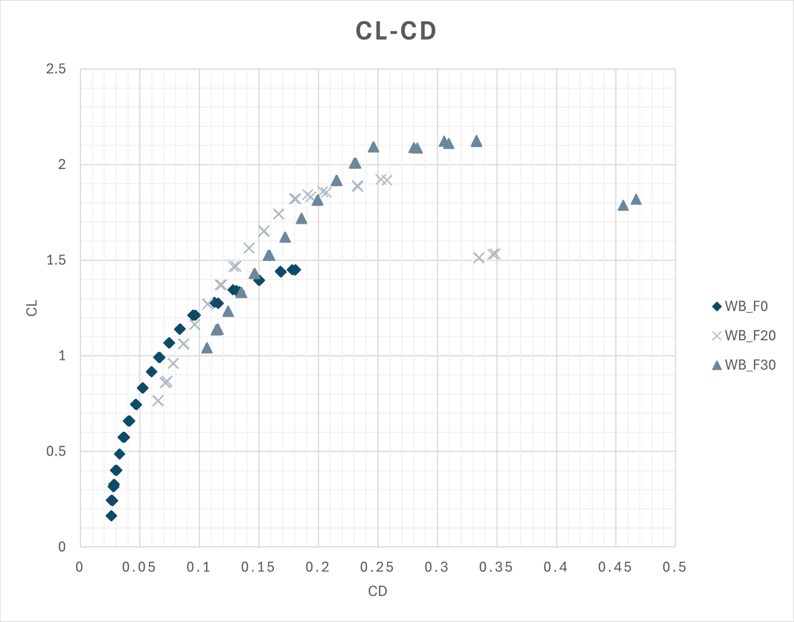

Figure 5.31: *Wing body configuration:* C_L *versus* C_D *for different flap deflections.*

The Oswald factor is slightly improved in take-off configuration, raising from 0.81 to 0.85, whereas the beneficial effect becomes less evident for landing, where the Oswald factor goes to 0.83.

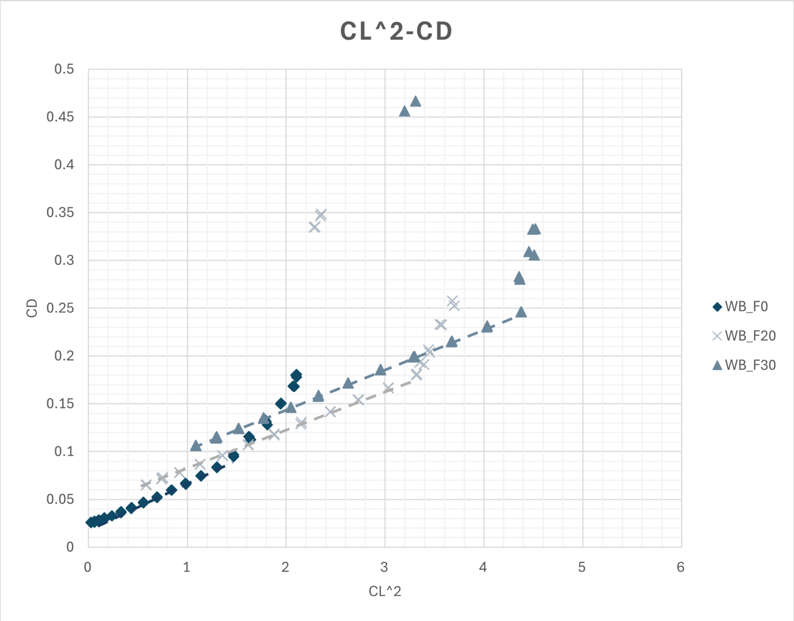

Figure 5.32: *Wing-Body configuration:* C_D *versus* C_L^2 *for various flap deflections.*

The aerodynamic efficiency is reduced by the flaps, as shown in Fig.5.33. The maximum efficiency achieved by the wing-body configuration with flap retracted is 16.4, progressively decreasing with flap deflection.

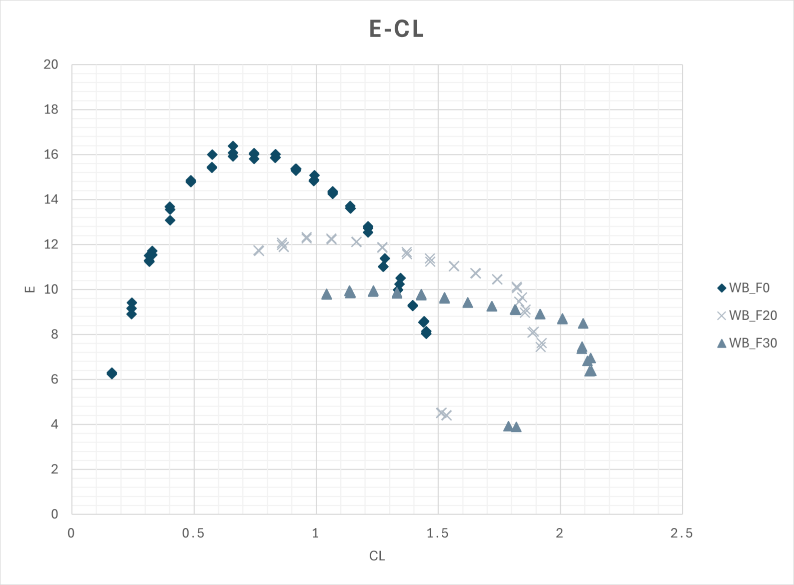

Figure 5.33: *Wing-Body configuration: E versus C_L for different flap deflections.*

A review of the calculated parameters is presented in the following table:

	WB_F0	**WB_F20**	**WB_F30**
$C_{L,max}$	1.4508	1.9231	2.0922
C_{L_α} $(1/deg)$	0.0810	0.0926	0.0907
C_{L_0}	0.3005	0.8053	1.0607
$C_{\mathcal{M}_\alpha}$ $(1/deg)$	0.0048	0.0006	0.0004
$C_{\mathcal{M}_{C_L}}$	0.0598	0.0063	0.0045
$C_{\mathcal{M}_0}$	−0.0228	−0.1508	−0.2354
C_{D_0}	0.0224	0.0393	0.0588
e	0.8120	0.8468	0.8271
E_{max}	16.382	12.330	9.955

Table 5.2: *Wing-Body: longitudinal aerodynamic parameters comparison between different flap configurations.*

The effect of flaps on aerodynamic parameters of the complete aircraft are displayed in the following diagrams: the $C_{L,max}$ increases from 1.6 to 2.07 in take-off setting and to 2.23 in landing, meanwhile considerations about the lift curve slope are the same as the wing-body configuration.

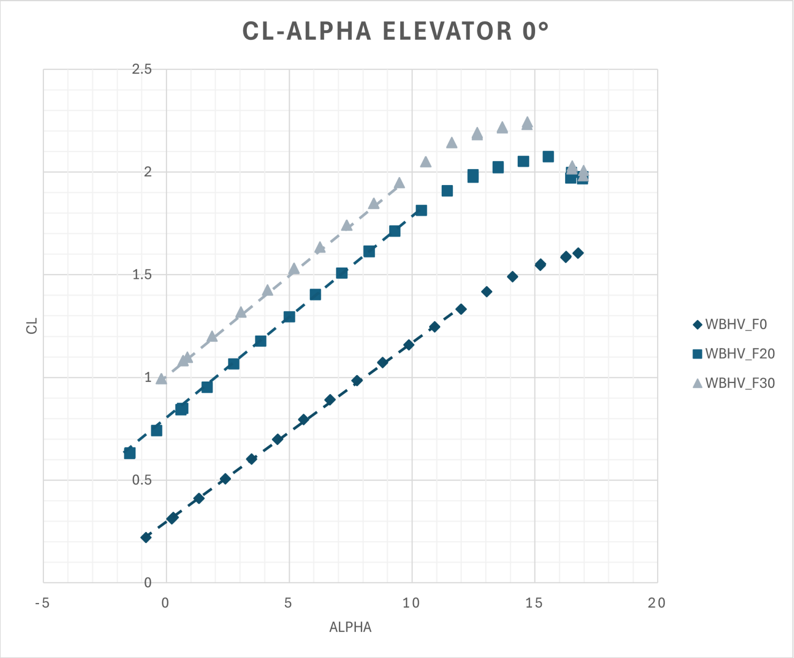

Figure 5.34: *Complete model:* C_L *versus* α *for different flap deflections.*

The $C_{\mathcal{M}}$ versus α and $C_{\mathcal{M}}$ versus C_L plots show the longitudinal stability performance of the aircraft, the negative contribution to the pitching moment slope is provided by the horizontal tail, ensuring the stable behavior of the seaplane.

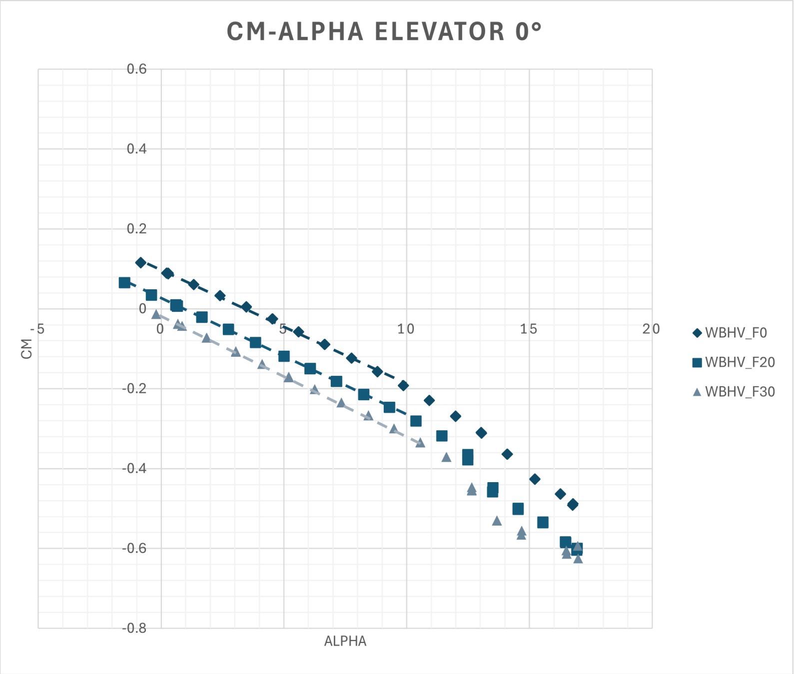

Figure 5.35: *Complete model:* $C_{\mathcal{M}}$ *versus* α *for different flap deflections.*

The effect of flap deflection is the shift of the curve by a negative offset and a slight decrease in the $C_{\mathcal{M}_\alpha}$. On the other hand, effects on the $C_{\mathcal{M}}$ versus C_L curve are the axact opposites, as the static stability margin, related to the slope of the curve in the linear range, is reduced by flap deflection, passing from 0.32 in clean configuration to 0.29 in take-off and 0.30 in landing, while the curves shift upwards with increasing angle of the flaps, leading to higher C_{M_0}.

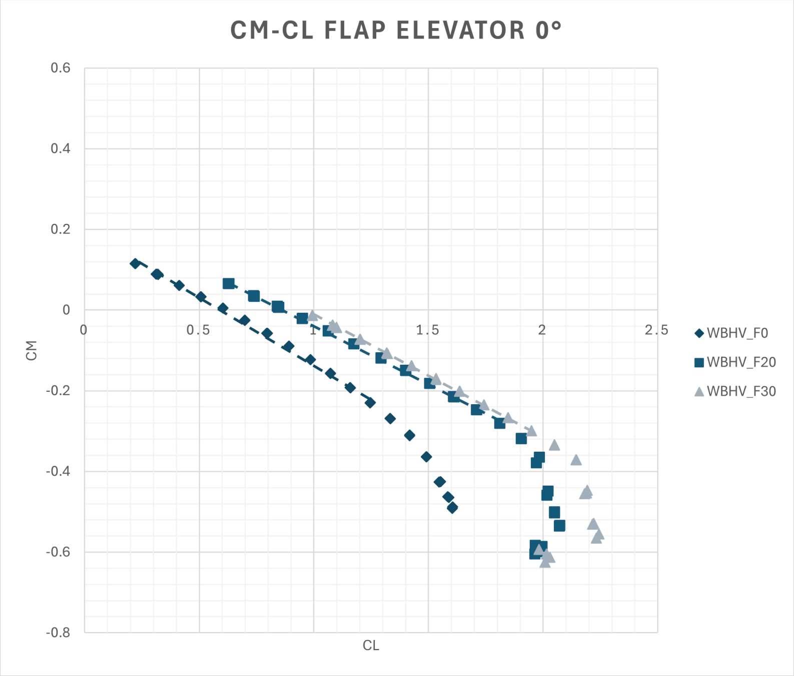

Figure 5.36: *Complete model: C_M versus C_L for different flap deflections.*

The drag polars of the complete aircraft at different flap positions are plotted in Fig. 5.37:

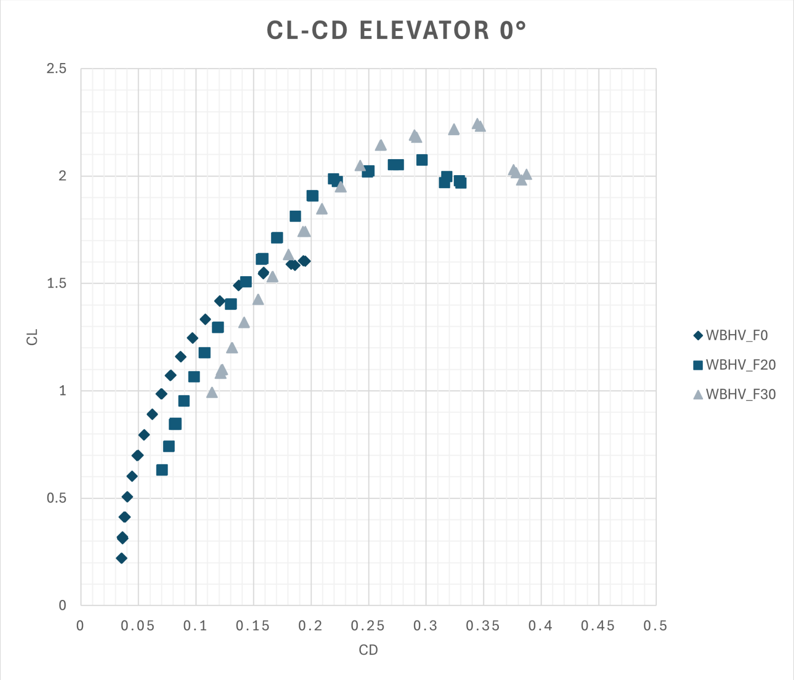

Figure 5.37: *Complete model: C_L versus C_D for different flap deflections.*

The increase in C_D is due to parasite and induced drag, The impact of flaps on drag is also visible through the C_D versus C_L^2 curve.

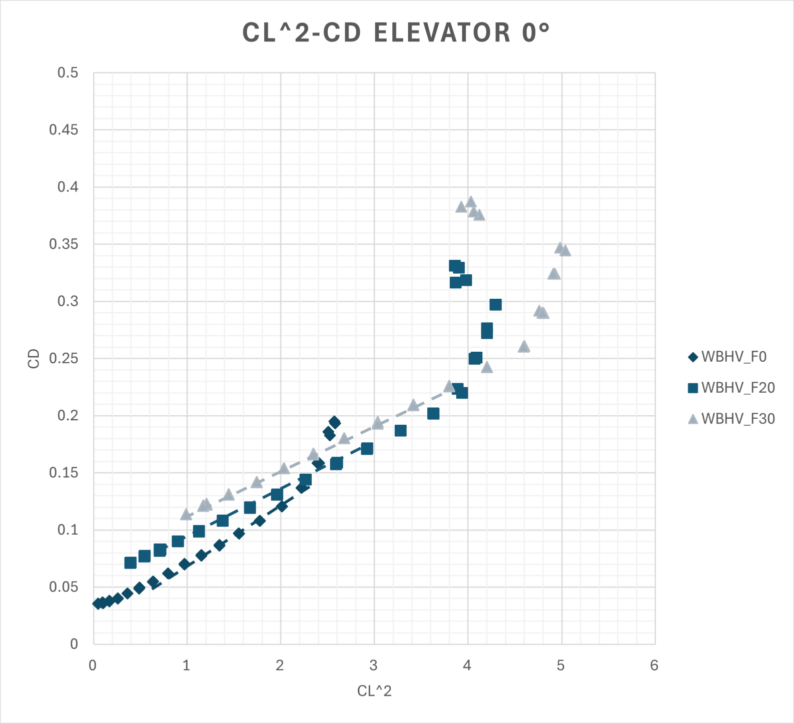

Figure 5.38: *Complete model:* C_D *versus* C_L^2 *for different flap deflections.*

Finally, the efficiency is significantly reduced by flap extension. The maximum efficiency reached by the complete model is 14.5, decreasing to 10.9 with take-off flaps and to 9.3 with landing flaps.

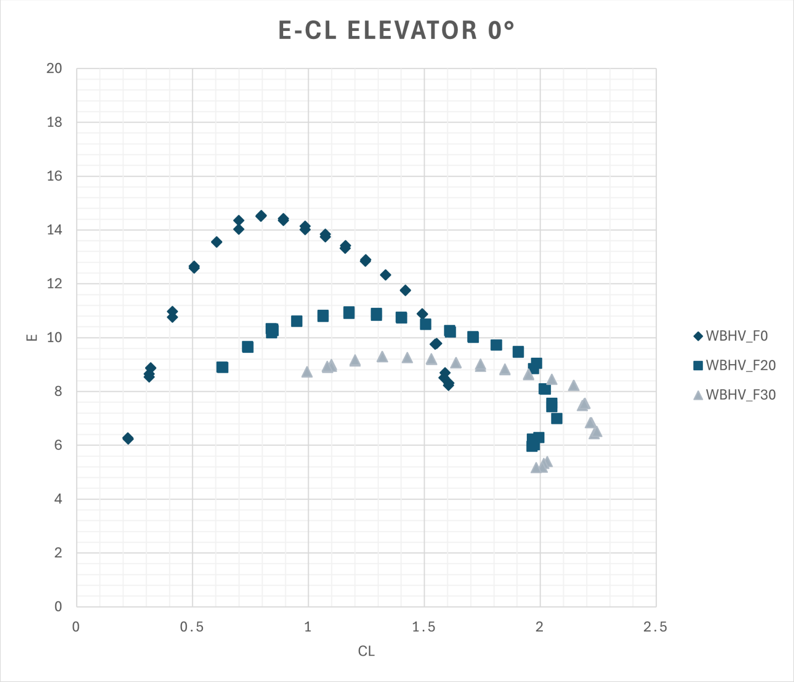

Figure 5.39: *Complete model:* E *versus* C_L *for different flap deflections.*

Aerodynamic parameters of the complete model for different flap deflections can be synthesized in the following table:

	WBHV_F0	**WBHV_F20**	**WBHV_F30**
$C_{L,max}$	1.6060	2.0732	2.2321
C_{L_α} $(1/deg)$	0.0895	0.1014	0.0985
C_{L_0}	0.2930	0.7836	1.0192
$C_{\mathcal{M}_\alpha}$ $(1/deg)$	−0.0287	−0.0294	−0.0296
$C_{\mathcal{M}_{C_L}}$	−0.3205	−0.2900	−0.3005
$C_{\mathcal{M}_0}$	0.1960	0.2553	0.2893
C_{D_0}	0.0301	0.0538	0.0731
e	0.8825	0.9050	0.8914
E_{max}	14.534	10.943	9.308

***Table 5.3:** Complete model: longitudinal aerodynamic parameters comparison between different flap configurations.*

Comparisons can be carried out for C_L versus α and $C_{\mathcal{M}}$ versus C_L curves of Wing-Body and complete model: the gap between the two configurations increases with angle of attack, an effect caused by the increasing slope due to the horizontal tail.

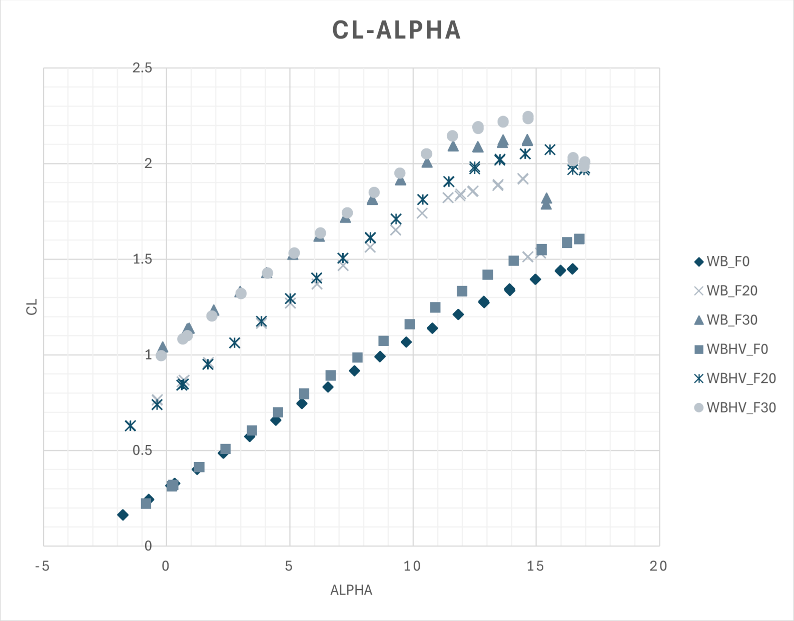

***Figure 5.40:** Wing body and Complete model: C_L versus α for different flap deflections.*

Flap deflection leads to different effects between the complete model and Wing-Body configurations: on the first, flaps cause a shift of the curve upward and increase the $C_{\mathcal{M}_{C_L}}$ because of the stronger downwash, the effect on the latter is the opposite. In fact, as the flap configuration transitions from clean to landing, the curves are moved down and the slope is diminished, due to the shift towards the trailing edge of the aerodynamic center.

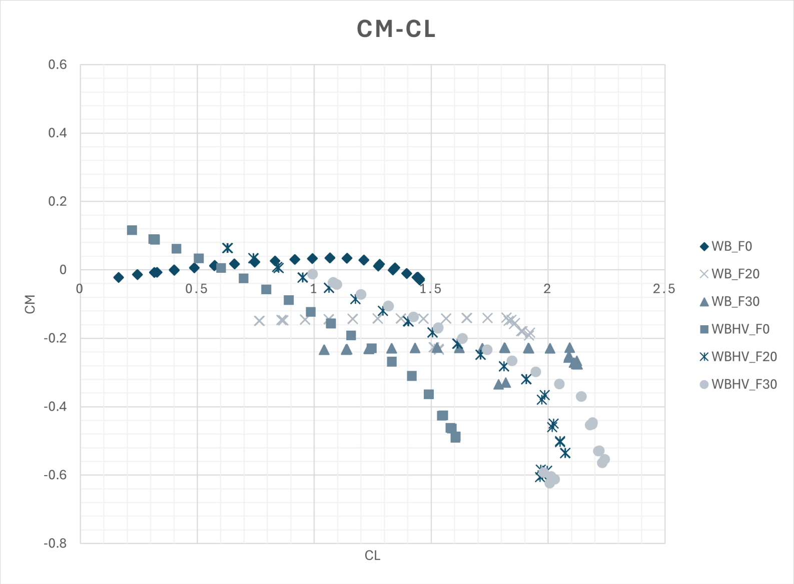

Figure 5.41: Wing body and Complete model: $C_{\mathcal{M}}$ versus C_L for different flap deflections.

	WBHV_F0	WB_F0	WBHV_F20	WB_F20	WBHV_F30	WB_F30
$C_{L,max}$	1.6060	1.4508	2.0732	1.9231	2.2321	2.0922
C_{L_α} $(1/deg)$	0.0895	0.0810	0.1014	0.0926	0.0985	0.0907
C_{L_0}	0.2930	0.3005	0.7836	0.8053	1.0192	1.0607
$C_{\mathcal{M}_{C_L}}$	−0.3205	0.0598	−0.2900	0.0063	−0.3005	0.0045
$C_{\mathcal{M}_0}$	0.1960	−0.0228	0.2553	−0.1508	0.2893	−0.2354

Table 5.4: Complete model and Wing-Body: aerodynamic parameters comparison at different flap configurations.

Elevator effect

The impact of the elevator on aerodynamic performance of the aircraft is studied for all flap configurations. Starting from flap retracted, the C_L versus α curve is presented in the following figure:

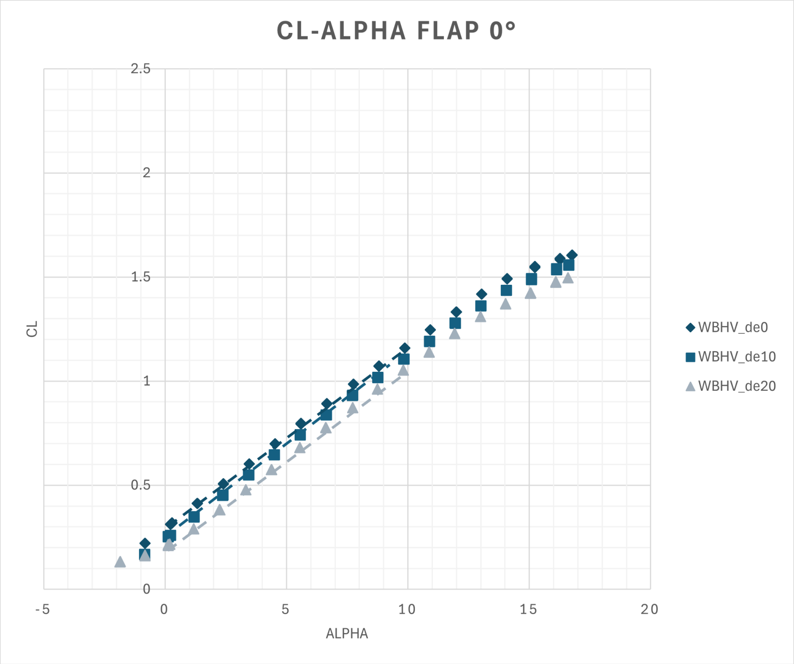

Figure 5.42: *Clean configuration:* C_L *versus* α *for different elevator deflections.*

The effect of the elevator deflection is to shift the lift curve slightly downward due to the downforce generated by the horizontal tail, reducing the $C_{L,max}$ of the aircraft, whereas the lift slope is not affected significantly.

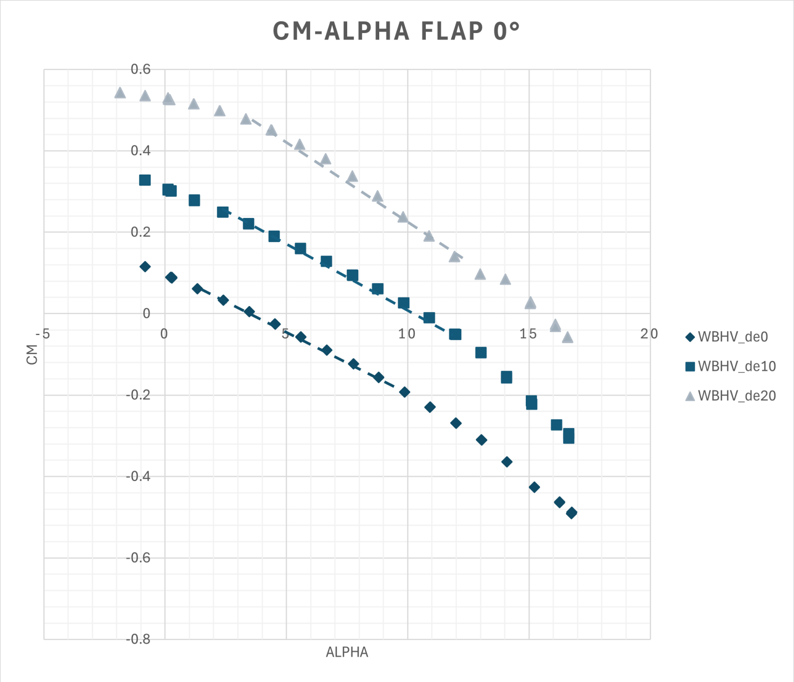

Figure 5.43: *Clean configuration:* C_M *versus* α *for different elevator deflections.*

The pitching moment curve translation is the main purpose of the elevator deflection. The trim angle is postponed from 4.5° without elevator up to 15.5° with $-20°$ of deflection, while the $C_{\mathcal{M}_\alpha}$ is not affected at all. At $-20°$ the linear range is smaller compared to other curves, where the linear range extends up to $12°$.

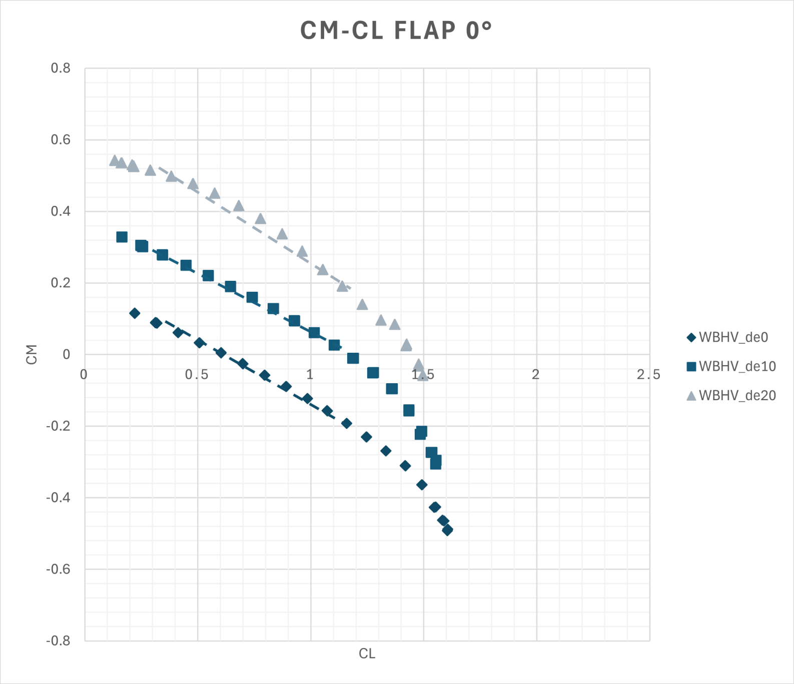

Figure 5.44: *Clean configuration:* $C_{\mathcal{M}}$ *versus* C_L *for different elevator deflections.*

The $C_{\mathcal{M}}$ versus C_L plot follows the same trend previously explained. The trim is reached up to $C_{L,max}$, which is the maximum lift coefficient in which is possible to trim the aircraft, usually defined as $C_{L_{e,max}}$. The static stability margin is slightly reduced from 0.321 without elevator deflection to 0.315 for -10 deflection and 0.304 for $-20°$ deflection.

Figures 5.45 and 5.46 display the drag polar and the C_D versus C_L^2 curves, the flap deflection effect is shifting the curve to lower C_L, increasing C_{D_0}. In addition, there is a beneficial effect in terms of Oswald factor.

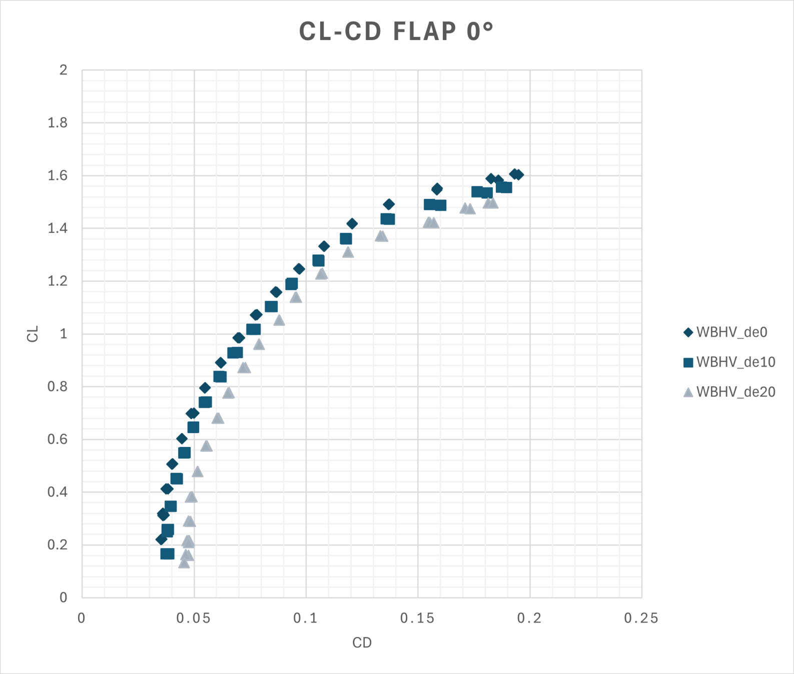

Figure 5.45: *Clean configuration:* C_L *versus* C_D *for different elevator deflections.*

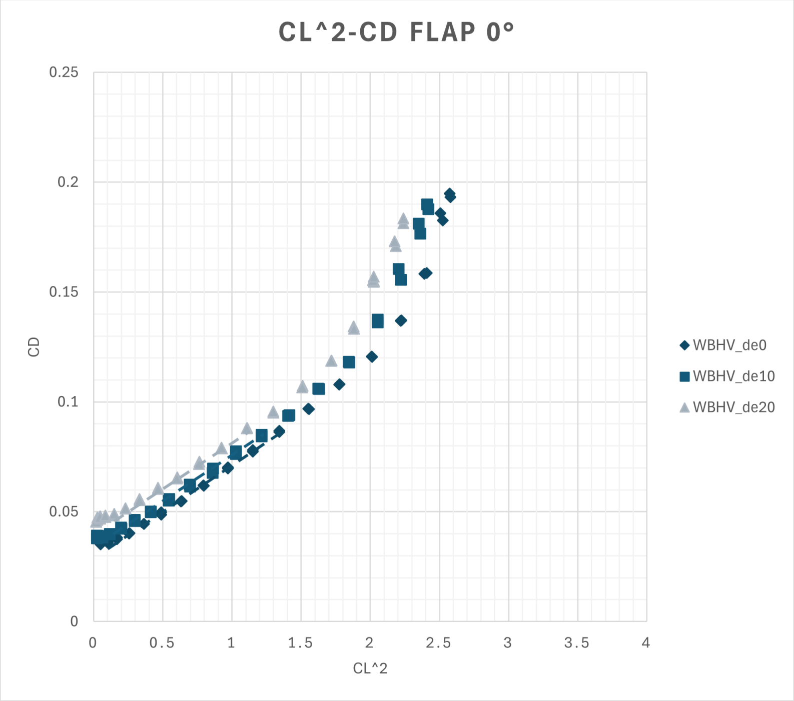

Figure 5.46: *Clean configuration:* C_D *versus* C_L^2 *for different elevator deflections.*

The efficiency curves are plotted in the following figure. The lower lift and increase in drag due to elevator deflection necessarily lead to lower aerodynamic efficiency compared to neutral position.

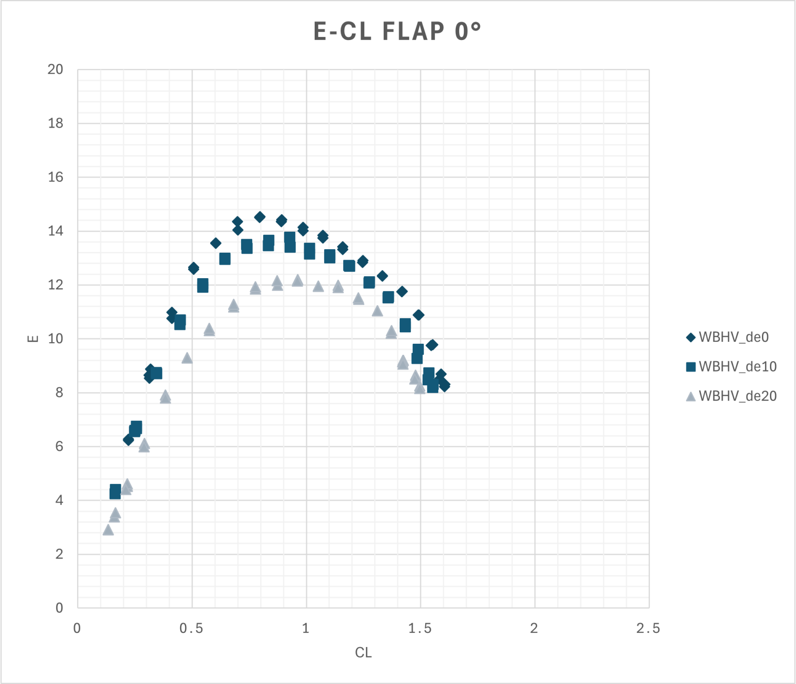

Figure 5.47: *Clean configuration: E versus C_L for different elevator deflections.*

A summary of the elevator deflection effects on the complete aircraft is provided in the following table:

	WBHV_de0	**WBHV_de10**	**WBHV_de20**
$C_{L,max}$	1.6060	1.5562	1.4962
C_{L_α} $(1/deg)$	0.0895	0.0899	0.0896
C_{L_0}	0.2930	0.2365	0.1823
C_{M_α} $(1/deg)$	−0.0287	−0.0283	−0.0272
$C_{M_{C_L}}$	−0.3205	−0.3146	−0.3035
C_{M_0}	0.1960	0.3899	0.5662
C_{D_0}	0.0301	0.0343	0.0437
e	0.8825	0.9119	0.9717
E_{max}	14.534	13.754	12.200

Table 5.5: *Complete model, flap 0°: aerodynamic parameters comparison between different elevator deflections.*

Elevator control derivatives on pitching moment and lift are listed in Tab.5.6. The elevator has low influence on lift coefficient, meanwhile its control authority is not constant with respect to the deflection angle, but decreases of 5% from 10° to 20°.

	WBHV_de10	WBHV_de20
$C_{L_{\delta_e}}$ $(1/deg)$	0.0057	0.0055
$C_{\mathcal{M}_{\delta_e}}$ $(1/deg)$	−0.0194	−0.0185

Table 5.6: *Complete model, flap* $0°$*: control derivatives.*

The impact of the elevator is then examined for the take-off configuration. Following the same trend described for clean setup, the overall lift coefficient is reduced by the elevator deflection, therefore the $C_{L,max}$ is reduced to 1.97 for $-20°$ deflection, decreasing the beneficial effect of flap. The C_{L_α}, on the other hand, does not experience significant changes.

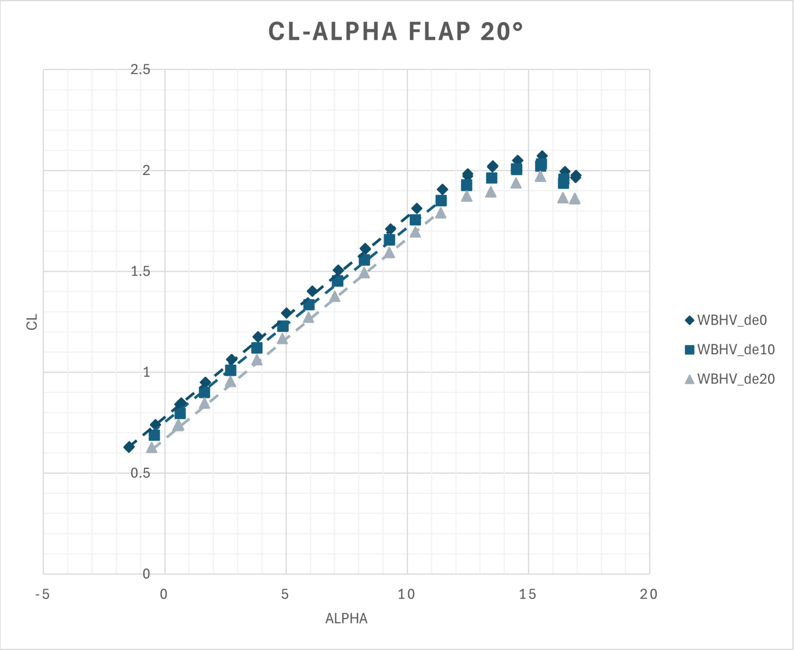

Figure 5.48: *Take-off configuration:* C_L *versus* α *for different elevator deflections.*

$C_{\mathcal{M}}$ versus α curves are provided in the following figure. The shift in the pitching moment curve grants to trim at various angles of attack. Looking at Fig.5.50, showing the $C_{\mathcal{M}}$ versus C_L curves, the Static Stability Margin is reduced by the elevator deflection, providing a beneficial effect in controlling the aircraft at higher lift coefficients. However, strong nonlinearities are shown at high values of C_L, drastically reducing the control power of the elevator.

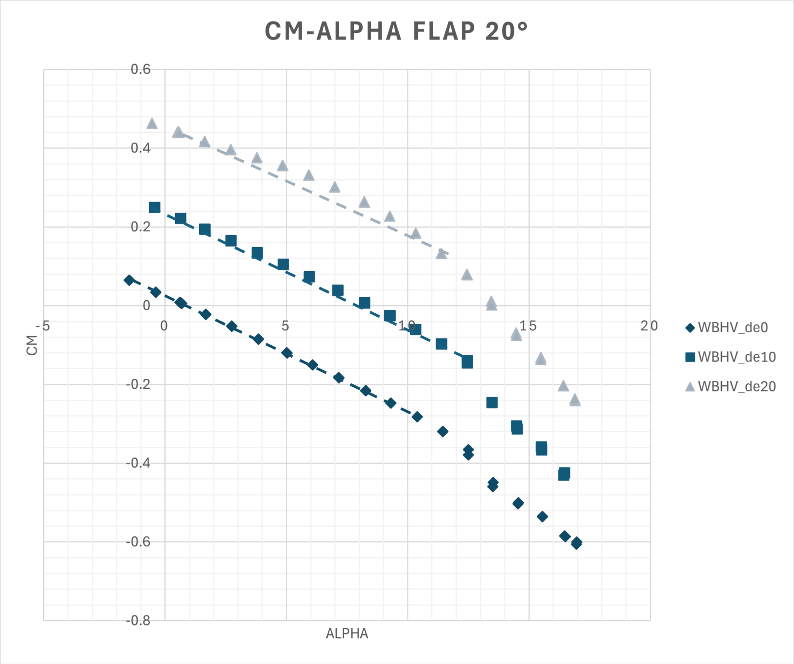

Figure 5.49: *Take-off configuration:* C_M *versus* α *for different elevator deflections.*

The equilibrium is reached at $C_L = 1.93$, hence the maximum lift coefficient achievable for the aircraft in take-off is the equilibrated lift coefficient $C_{L_e,max} = 1.93$, instead of the initial 2.07 obtained without elevator deflection.

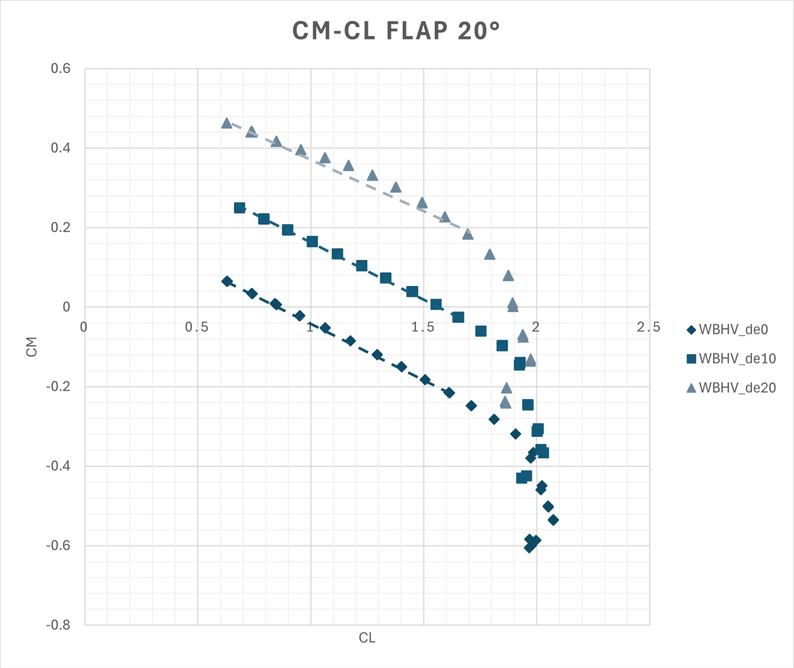

Figure 5.50: *Take-off configuration:* C_M *versus* C_L *for different elevator deflections.*

The drag polar is shifted towards higher values of the C_D as the elevator is deflected upwards. The increment of Oswald factor is experienced also for the take-off configuration, even though the increased downwash reduces this parameter at $-20°$.

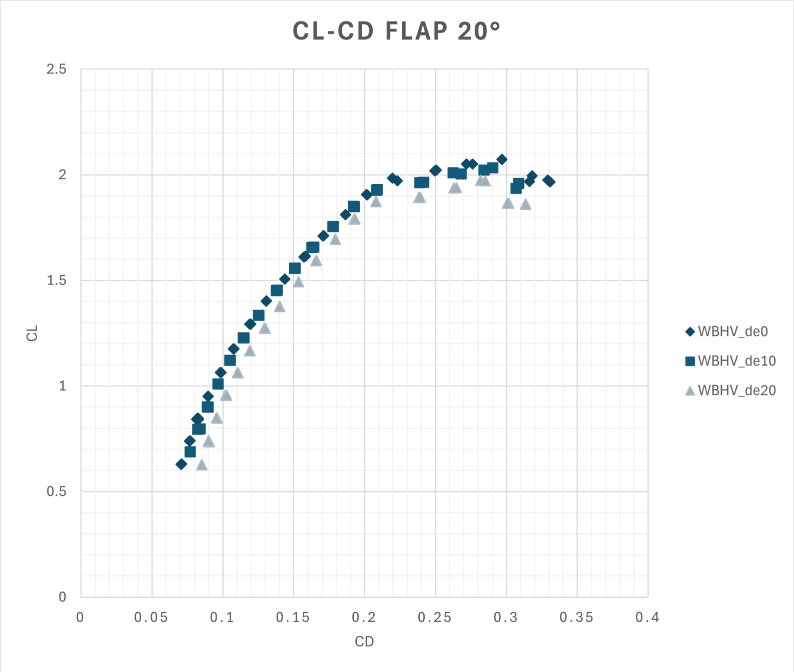

Figure 5.51: *Take-off configuration:* C_L *versus* C_D *for different elevator deflections.*

The maximum deflection produces a considerable increase in drag coefficient.

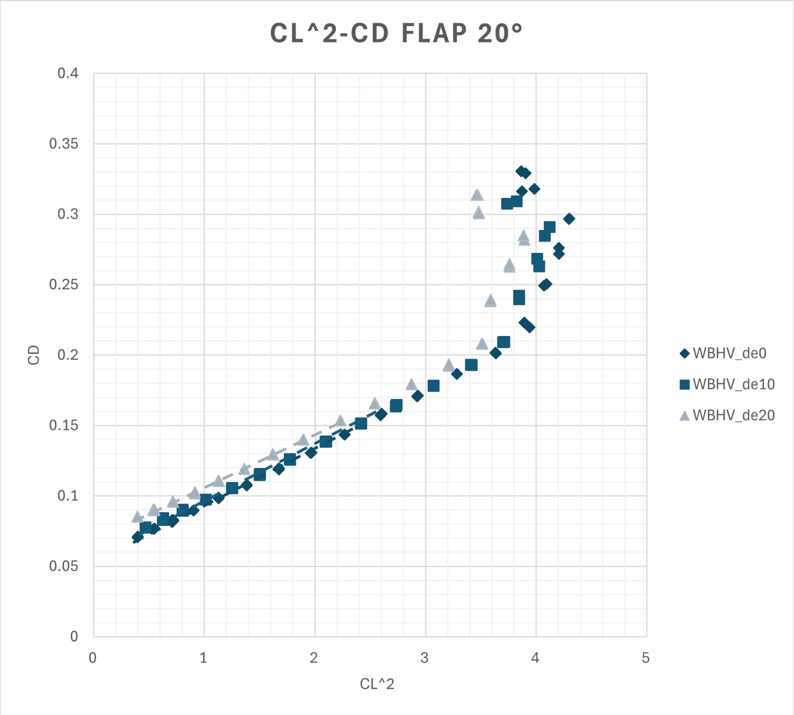

Figure 5.52: *Take-off configuration:* C_D *versus* C_L^2 *for different elevator deflections.*

The aerodynamic efficiency reflects considerations on drag previously expressed: the decreasing effect is enlarged at $-20°$ deflection, lowering the maximum value at 9.85 compared to 10.94 obtained without deflection.

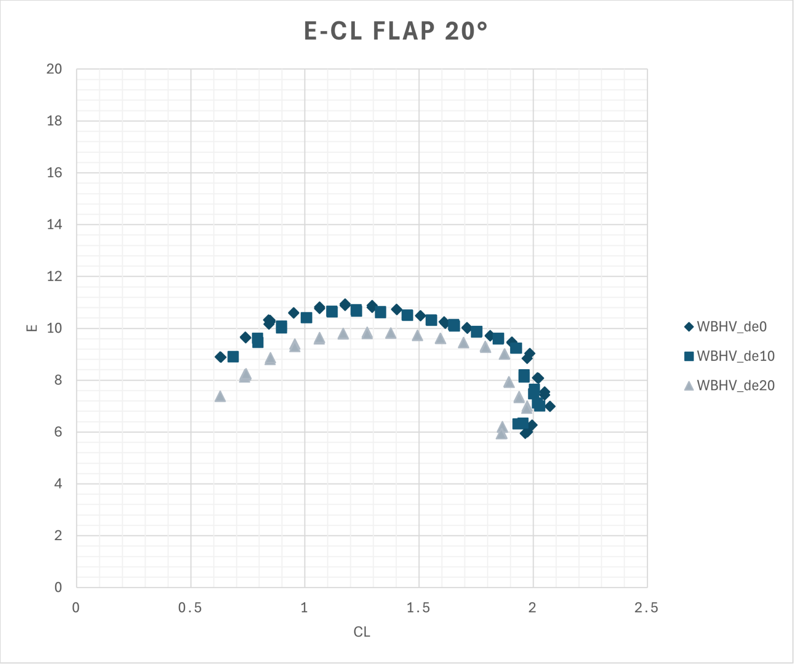

Figure 5.53: *Take-off configuration: E versus* C_L^2 *for different elevator deflections.*

Aerodynamic parameters and derivatives are listed in the following table, providing a comprehensive summary of the elevator effects at take-off:

	WBHV_de0	**WBHV_de10**	**WBHV_de20**
$C_{L,max}$	2.0732	2.0306	1.9728
C_{L_α} $(1/deg)$	0.1014	0.1010	0.0986
C_{L_0}	0.7836	0.7316	0.6880
C_{M_α} $(1/deg)$	-0.0294	-0.0279	-0.0210
$C_{M_{C_L}}$	-0.2900	-0.2766	-0.2132
C_{M_0}	0.2553	0.4414	0.6006
C_{D_0}	0.0538	0.0591	0.0680
e	0.9050	0.9510	0.9384
E_{max}	10.943	10.7036	9.856

Table 5.7: *Complete model, flap* 20°*: aerodynamic parameters comparison between different elevator deflections.*

The elevator control authority is described by the $C_{L_{\delta_e}}$ and $C_{M_{\delta_e}}$ coefficients:

	WBHV_de10	**WBHV_de20**
$C_{L_{\delta_e}}$ $(1/deg)$	0.0052	0.0048
$C_{M_{\delta_e}}$ $(1/deg)$	-0.0186	-0.0172

Table 5.8: *Complete model, flap* 20°*: control derivatives.*

Following figures focus on the elevator effect on the aircraft model with flap in landing position. C_L experience an overall reduction due to the downforce produced by elevator deflection, the $C_{L,max}$ is therefore decreased from 2.23 to 2.14 at maximum deflection.

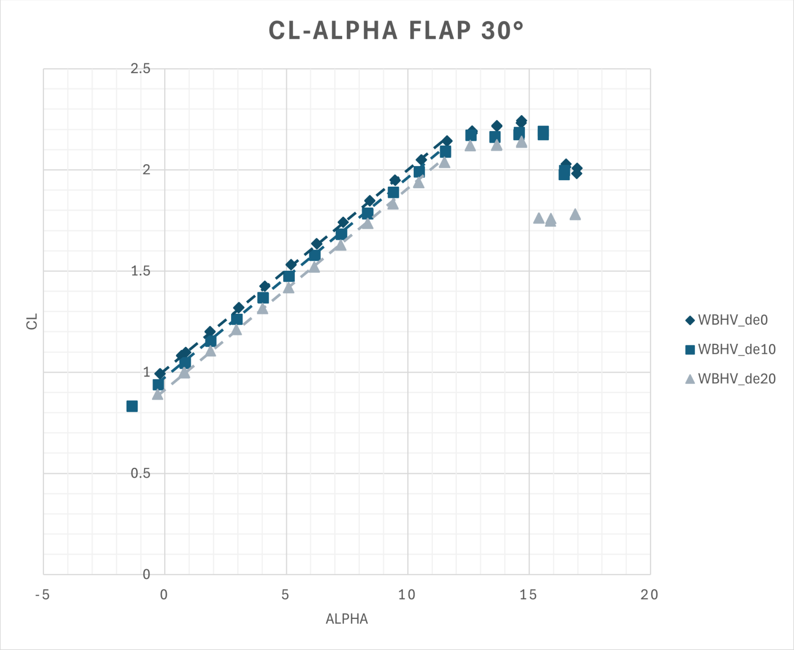

Figure 5.54: *Landing configuration:* C_L *versus* α *for different elevator deflections.*

Pitching moment curves are displayed in Fig. 5.55. It can be noticed the shift of the C_M to higher values as the deflection progressively reaches more negative values.

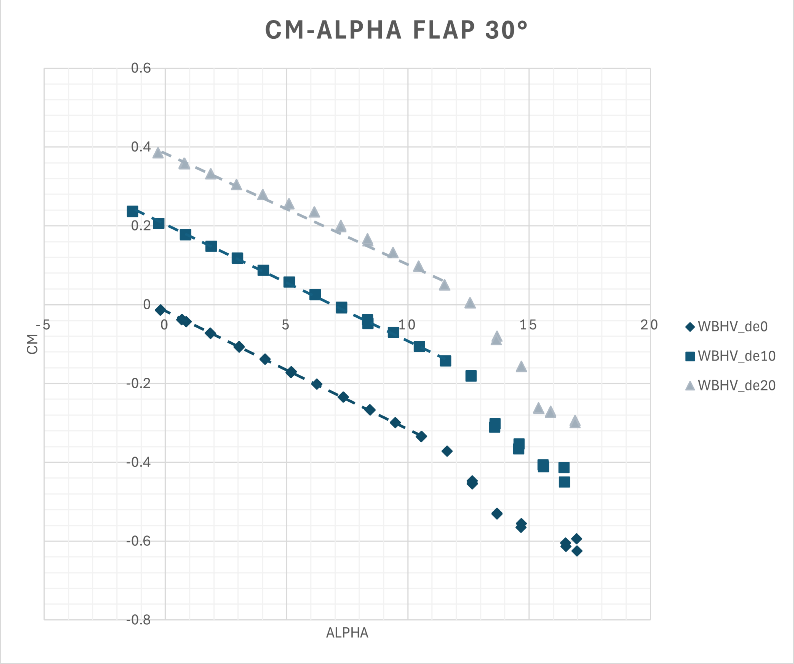

Figure 5.55: *Landing configuration:* C_M *versus* α *for different elevator deflections.*

The C_M versus C_L curve is fundamental to evaluate the performance in landing condition, as the aircraft has to reach the highest value of lift while controlling the pitch. The elevator authority drastically influences the maximum lift coefficient achievable and consequently the stall speed.

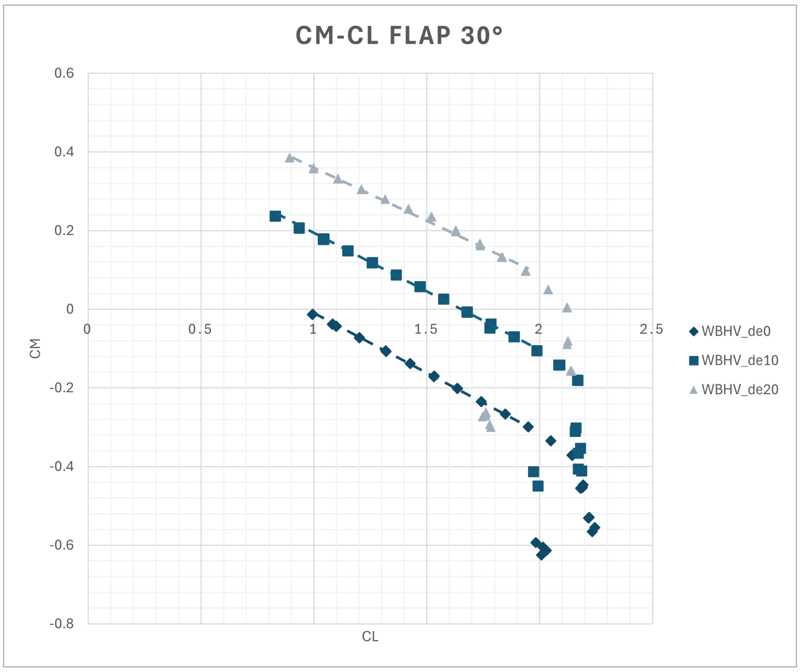

Figure 5.56: *Landing configuration:* C_M *versus* C_L *for different elevator deflections.*

The elevator deflection reduces the Static Stability Margin and shifts pitching moment curves upwards, trimming the aircraft at higher C_L coefficients. Non linearity at the maximum deflection still provides enough control power to the elevator to guarantee pitch control at lift coefficient near the stall with a maximum equilibrated lift coefficient of 2.12.

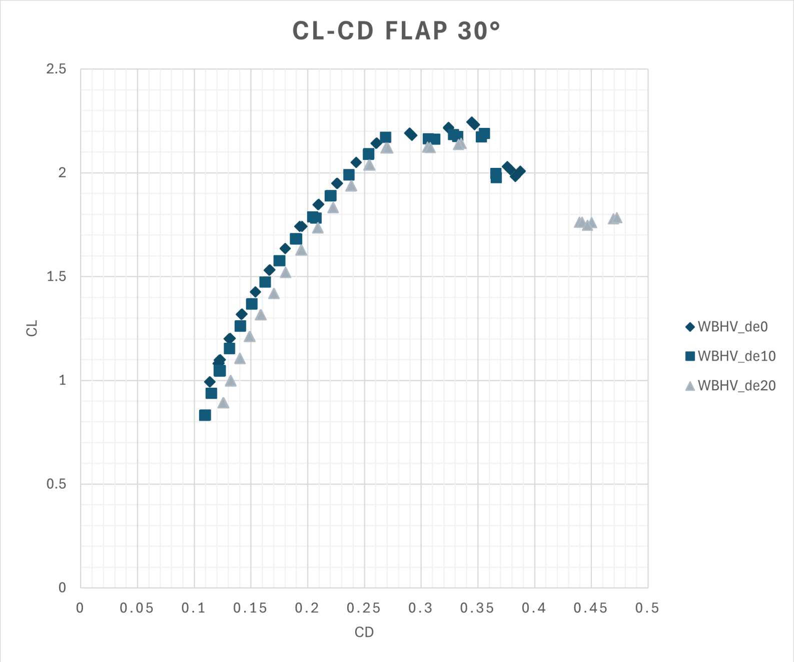

***Figure 5.57:** Landing configuration: C_L versus C_D for different elevator deflections.*

Regarding drag, the effects of the deflection of the elevator are similar to those shown in other configurations, that is the increase in parasite drag and a beneficial effect on the Oswald factor.

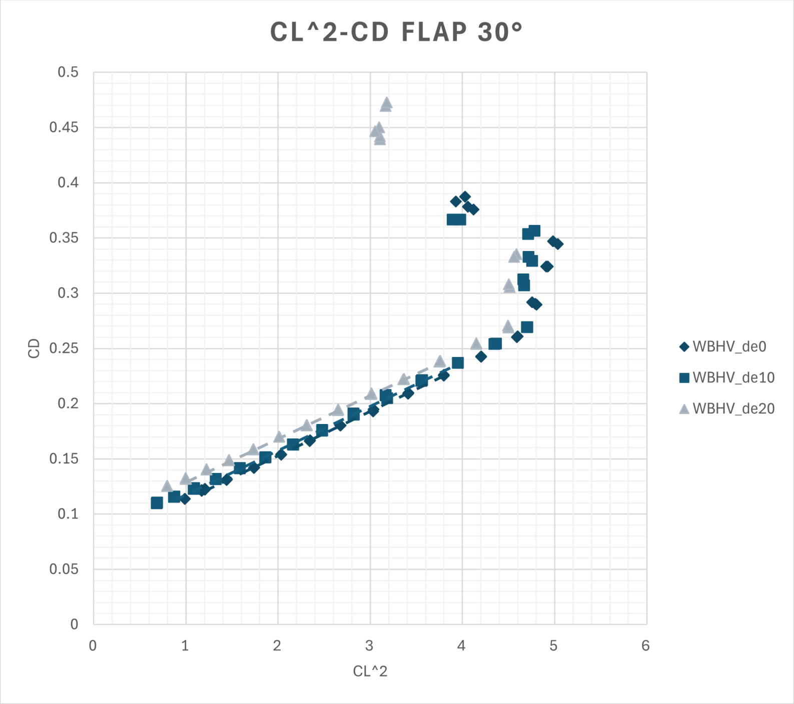

***Figure 5.58:** Landing configuration: C_D versus C_L^2 for different elevator deflections.*

Efficiency obtained in landing configuration is lower compared to other configurations. The elevator further contributes to decreasing this value, especially at maximum deflection.

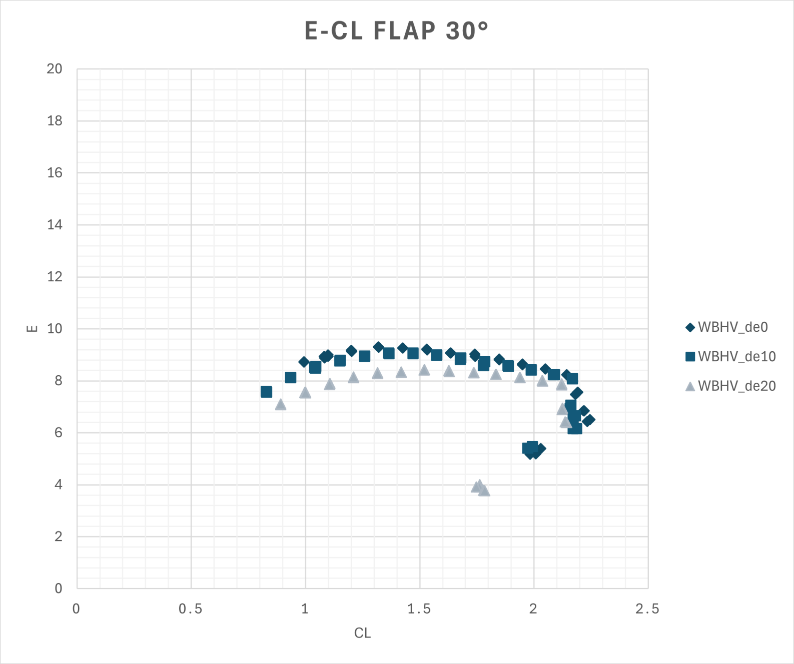

Figure 5.59: *Landing configuration: E versus* C_L *for different elevator deflections.*

The Tab.5.9 offers a synthesis of the aerodynamic effect of the elevator in landing condition:

	WBHV_de0	**WBHV_de10**	**WBHV_de20**
$C_{L,max}$	2.2321	2.1879	2.1420
C_{L_α} $(1/deg)$	0.0985	0.0983	0.0971
C_{L_0}	1.1092	0.9662	0.9244
C_{M_α} $(1/deg)$	−0.0296	−0.0289	−0.0239
$C_{M_{C_L}}$	−0.3005	−0.2939	−0.2458
C_{M_0}	0.2893	0.4874	0.6039
C_{D_0}	0.0731	0.0792	0.0936
e	0.8914	0.9166	0.9409
E_{max}	9.308	9.055	8.43

Table 5.9: *Complete model, flap* 30°*: longitudinal aerodynamic parameters comparison between different elevator deflections.*

Concerning control derivatives, the $C_{L_{\delta_e}}$ is similar compared to other configurations, whereas $C_{M_{\delta_e}}$ has an higher value at $-10°$ compared to clean and take-off conditions. At $-20°$, however, the decrease in the control derivative is larger than those registered in other cases.

	WBHV_de10	**WBHV_de20**
$C_{L_{\delta_e}}$ $(1/deg)$	0.0053	0.0047
$C_{M_{\delta_e}}$ $(1/deg)$	−0.0198	−0.0157

Table 5.10: *Complete model, flap 30°: control derivatives.*

The analysis of the effects of elevator deflection can be completed by comparing the aerodynamic performance between clean and take-off flap configuration and combining the different elevator deflections. Lift coefficient is influenced by the flap extension, increasing $C_{L,max}$ and C_{L_α}. The elevator deflection has similar impact on the two configurations, specifically in shifting lift curve downwards.

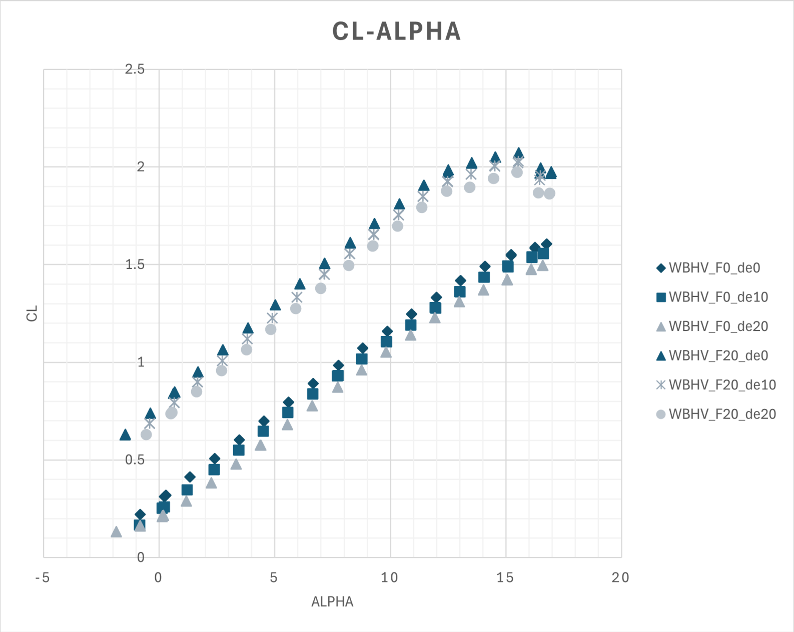

Figure 5.60: *Cruise and take-off:* C_L *versus* α *for different elevator deflections.*

Pitching moment curves are mainly influenced by the elevator deflection, with an offset between cruise and take-off due to the pitching moment induced by flaps.

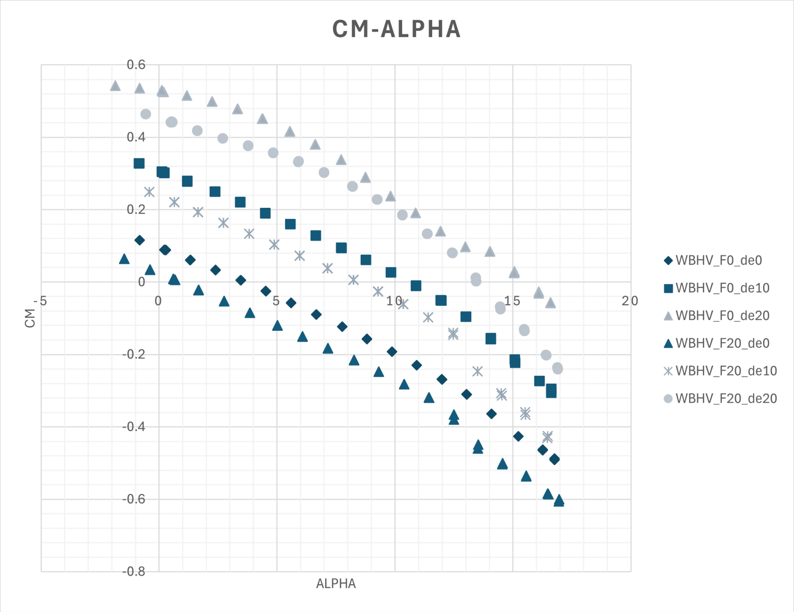

Figure 5.61: *Cruise and take-off:* $C_{\mathcal{M}}$ *versus* α *for different elevator deflections.*

$C_{\mathcal{M}}$ versus C_L plot shows a translation of pitching moment curves to higher values of C_L in take-off condition and an increased effect in reducing the static stability margin by deflecting the elevator.

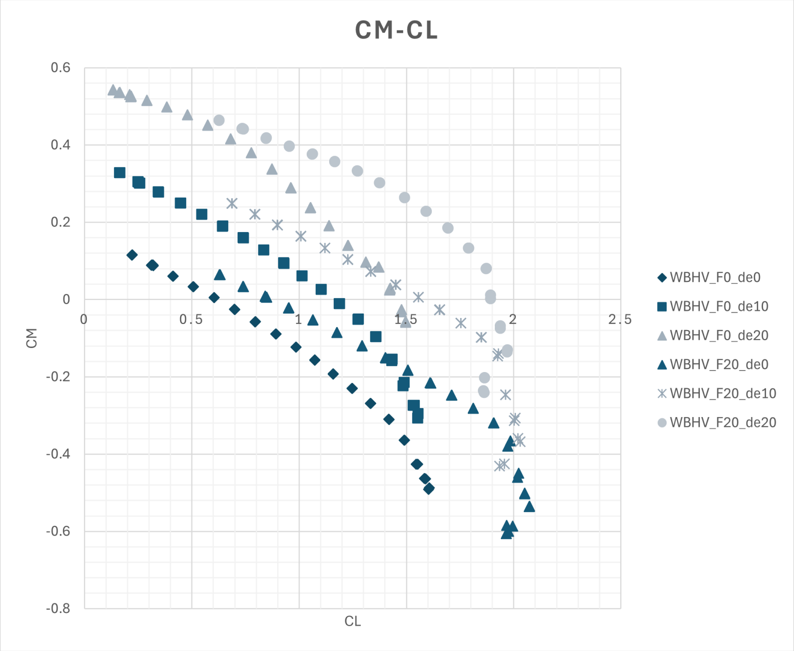

Figure 5.62: *Cruise and take-off:* $C_{\mathcal{M}}$ *versus* C_L *for different elevator deflections.*

Figures 5.63 and 5.64 show the difference in drag between the two configurations. The elevator generates a similar effect in both flap settings.

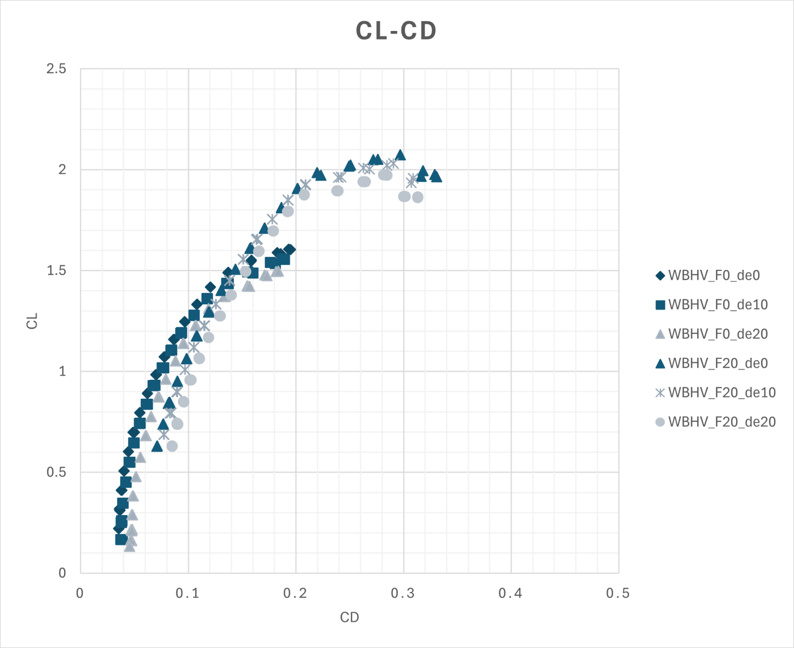

Figure 5.63: *Cruise and take-off:* C_L *versus* C_D *for different elevator deflections.*

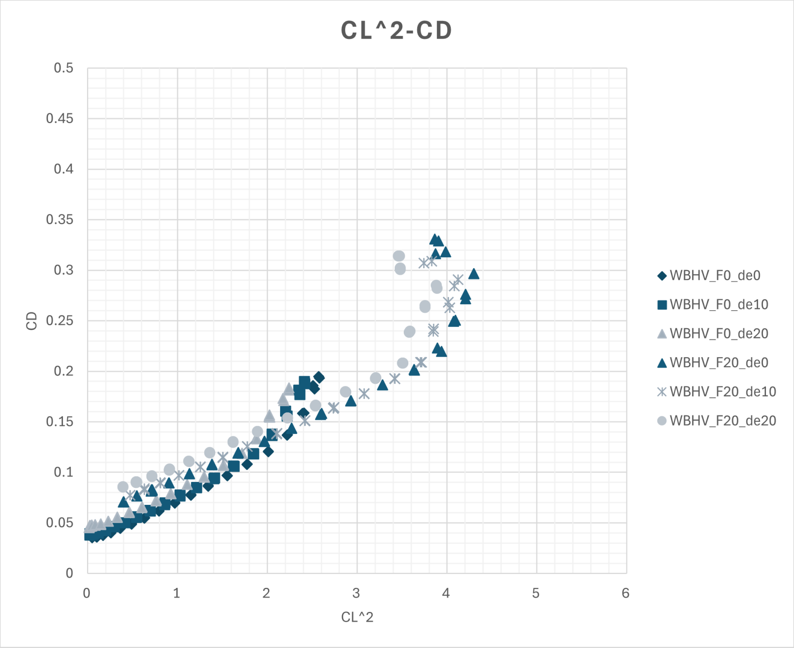

Figure 5.64: *Cruise and take-off:* C_D *versus* C_L^2 *for different elevator deflections.*

The efficiency experiences greater variation due to the elevator deflection in cruise condition, as shown in the following plot:

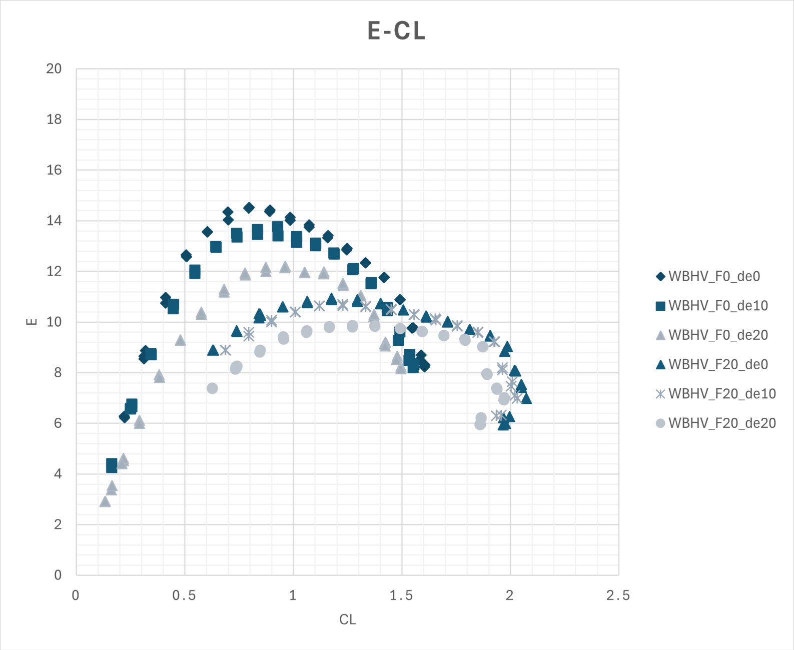

Figure 5.65: Cruise and take-off: E versus C_L for different elevator deflections.

Floats effect

The influence of the floats on the aerodynamic performance of the aircraft is examined in order to evaluate possible unfavorable effects on lift, drag and stability. Aerodynamic characteristics are evaluated comparing tests performed on the complete aircraft model. As shown in the following plot, lift is not particularly influenced by the addition of floats.

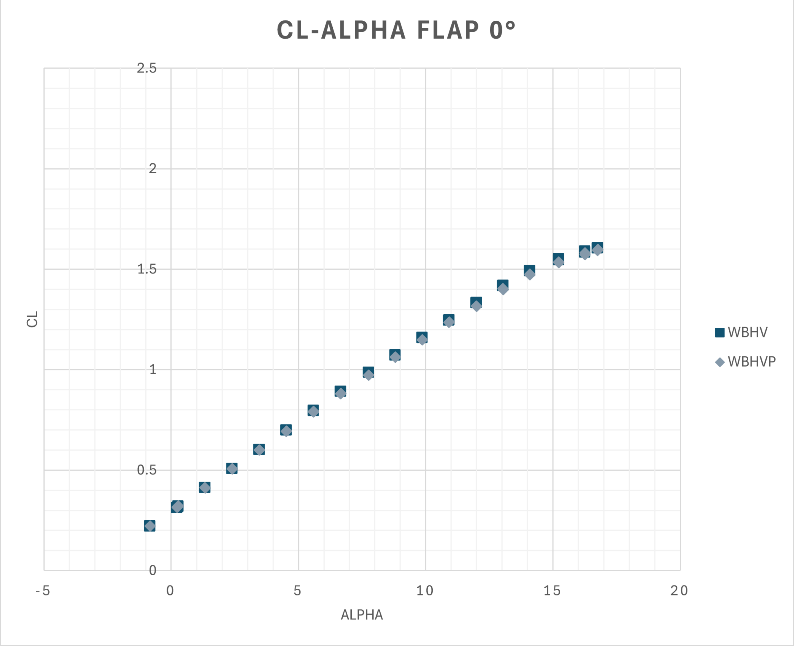

Figure 5.66: Floats influence on complete aircraft: C_L versus α

The same trend is registered for the pitching moment: the disturbance produced by additional bodies under the wing does not affect aircraft longitudinal stability.

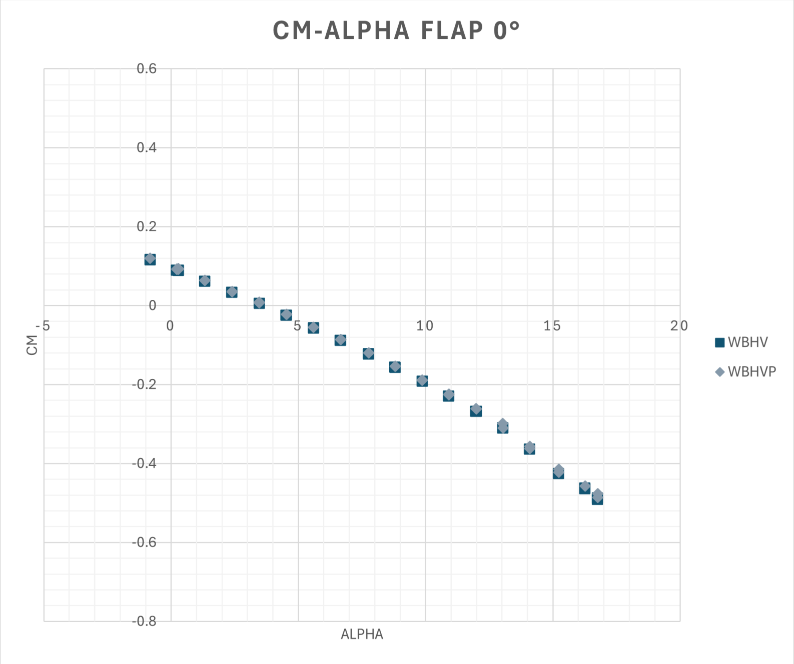

Figure 5.67: *Float influence on complete aircraft:* C_M *versus* α

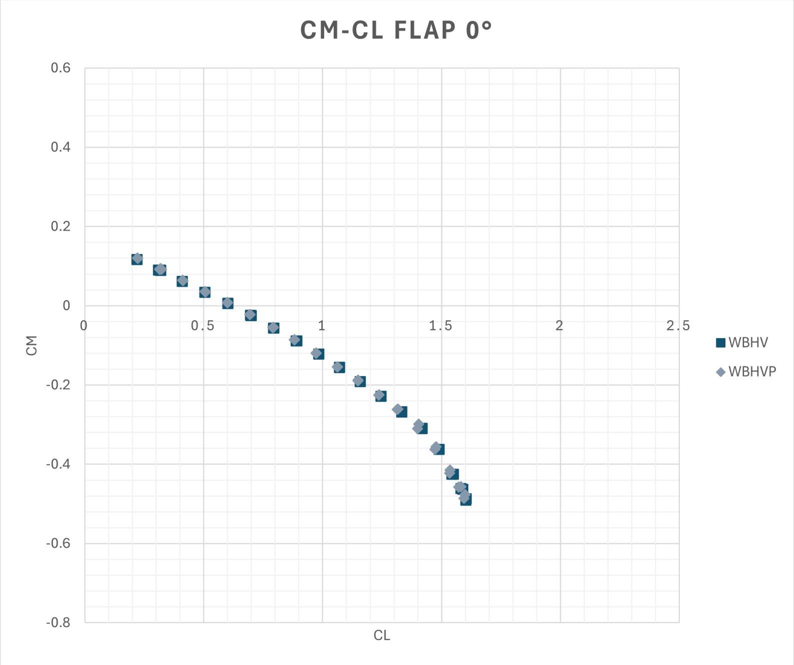

Figure 5.68: *Float influence on complete aircraft:* C_M *versus* C_L

The main effect of floats shows on drag: the additional bodies increase the wet surface and consequently friction drag. Furthermore, their blunt shape with the sharp step produces a large separation which contributes to the increase of pressure drag. These effects, along with possible interference drag produced by the interaction between wing and float, are responsible for the increased drag of the seaplane.

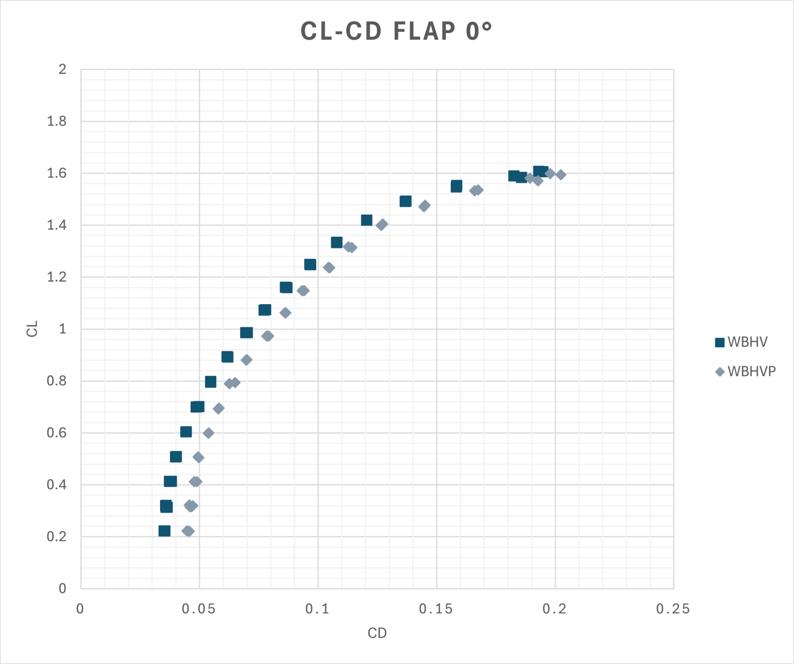

Figure 5.69: Floats influence on complete aircraft: C_L versus C_D

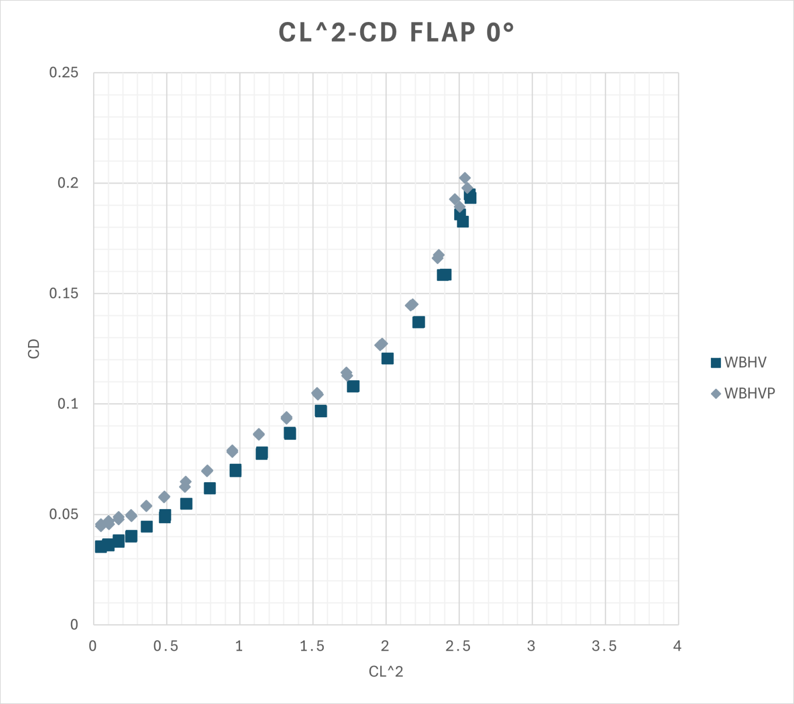

Figure 5.70: Floats influence on complete aircraft: C_D versus C_L^2

As expected, the increasing drag affects the overall efficiency of the aircraft.

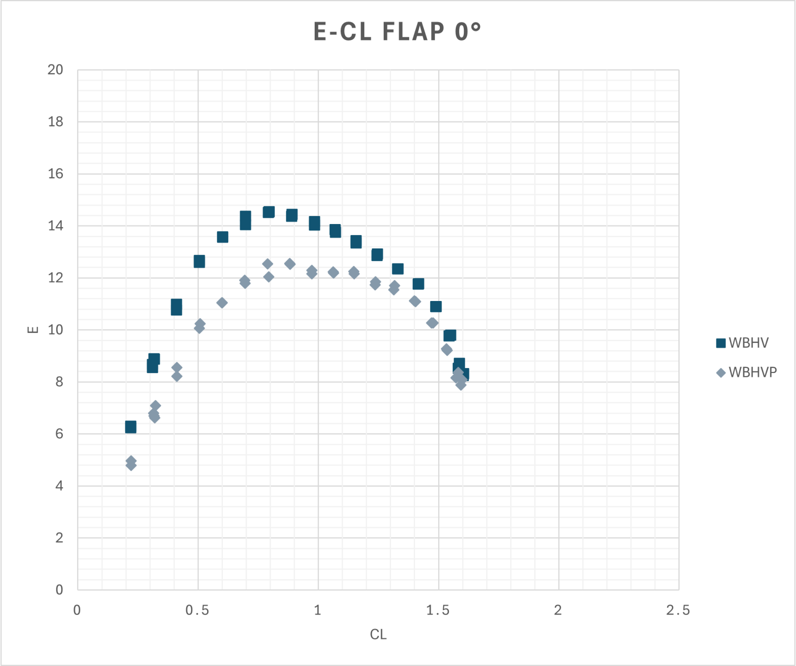

Figure 5.71: *Float influence on complete aircraft: E versus* C_L

Table 5.11 lists all the parameters necessary for the analysis of floats effect on aircraft aerodynamic performance:

	WBHV	**WBHVP**
C_{L_α} $(1/deg)$	0.0895	0.0877
C_{L_0}	0.2930	0.2967
C_{M_α} $(1/deg)$	−0.0287	−0.0297
$C_{M_{C_L}}$	−0.3205	−0.3260
C_{M_0}	0.1960	0.2013
C_{D_0}	0.0301	0.0400
e	0.8825	0.9073
E_{max}	14.534	12.553

Table 5.11: *Complete model, float effects: aerodynamic parameters comparison*

Downwash calculation

The determination of the downwash derivative is fundamental to understand how the flow around the tail behaves and to analyze the influence of the wing on the horizontal tail. The wing's circulation reduces the incidence of the airflow on the horizontal tail, impacting significantly on its performance and, consequently, on longitudinal stability. Furthermore, understanding the downwash produced by the wing is critical to prevent deep-stall risk, which is a typical phenomenon related to T-tail configuration: when the aircraft is at high angles of attack, the wake of the wing could impact the horizontal tail resulting in a complete loss of stability; consequently, a pitch-up moment arises, leading the airplane to exceed the stall angle. The result is the aircraft "locked" at extremely high angles of attack, with a completely stalled wing and without the possibility of recovering due to ineffective longitudinal control. The downwash derivative estimation is performed applying the following consideration: the $C_{\mathcal{M}_\alpha}$ of the complete aircraft can be expressed as

$$C_{\mathcal{M}_{\alpha,WBHV}} = C_{\mathcal{M}_{\alpha,WB}} - \eta_H V_h C_{L_{\alpha,H}} \left(1 - \frac{d\epsilon}{d\alpha}\right) \tag{5.3}$$

while the $C_{\mathcal{M}_\alpha}$ of the body-tail configuration is

$$C_{\mathcal{M}_{\alpha,BHV}} = C_{\mathcal{M}_{\alpha,B}} - \eta_H V_h C_{L_{\alpha,H}} \tag{5.4}$$

in this way, supposing that the dynamic pressure ratio is the same between the body-tail configuration and complete aircraft, the downwash derivative $1 - \frac{d\epsilon}{d\alpha}$ is obtained by the ratio:

$$\frac{C_{\mathcal{M}_{\alpha,WBHV}} - C_{\mathcal{M}_{\alpha,WB}}}{C_{\mathcal{M}_{\alpha,BHV}} - C_{\mathcal{M}_{\alpha,B}}} = \frac{\eta_H V_h C_{L_{\alpha,H}} \left(1 - \frac{d\epsilon}{d\alpha}\right)}{\eta_H V_h C_{L_{\alpha,H}}} \tag{5.5}$$

These tests provide the derivatives required for determining the downwash, providing the computation for all three flap settings. $C_{\mathcal{M}}$ versus α curves for the required configurations are shown below:

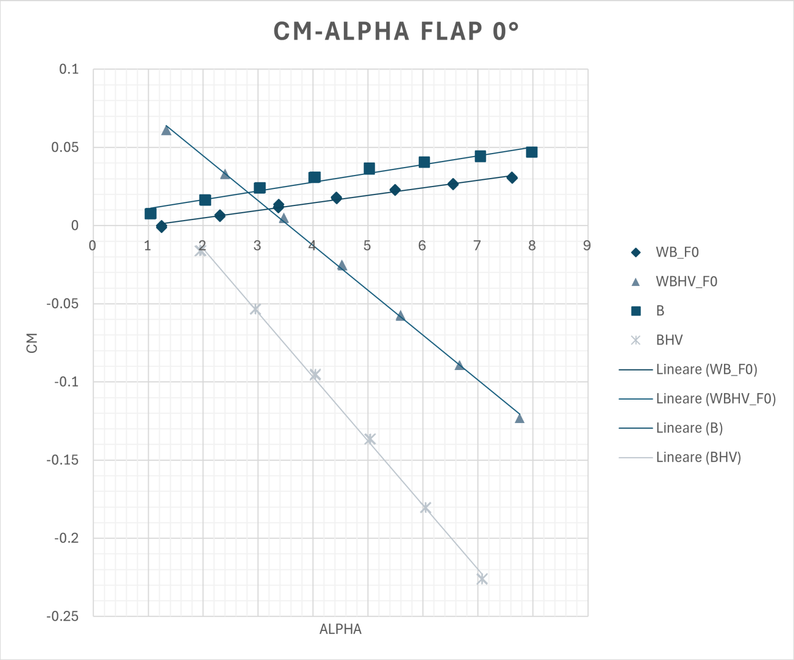

Figure 5.72: Required derivatives for downwash determination (flaps cruise)

While the $C_{\mathcal{M}_\alpha}$ of the body and body-tail configuration is the same for all three conditions, the derivatives related to the complete aircraft and wing-body differ between the various flap positions.

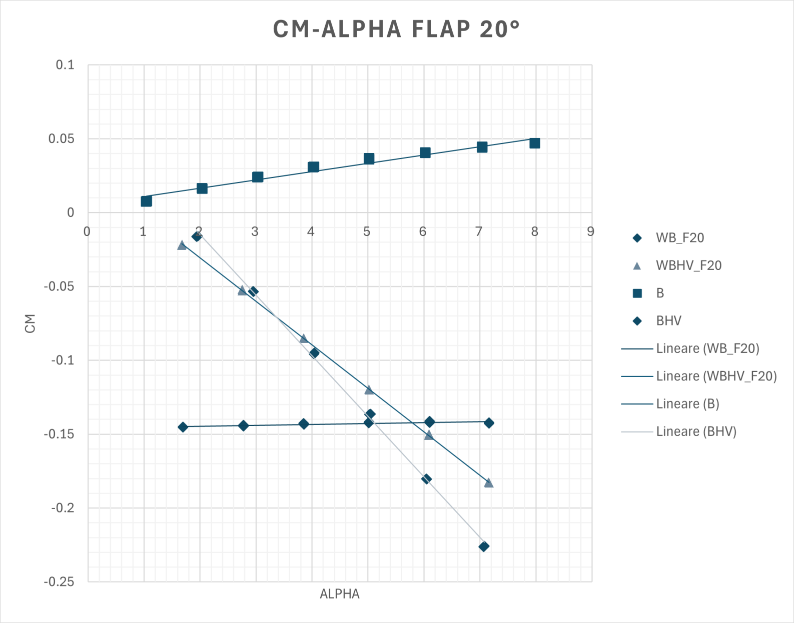

Figure 5.73: *Required derivatives for downwash determination (flaps take-off)*

Tab.5.12 sums up the required parameters: as only slight changes in $C_{\mathcal{M}_\alpha}$ occur between landing and take-off settings, the overall downwash derivative does not change. Cruise condition has a lower downwash derivative compared to other flap deflections, even though it shows a less stable behaviour. This is explained by the higher instability of the Wing-Body compared to the other flap settings, which compensates in the overall downwash derivative.

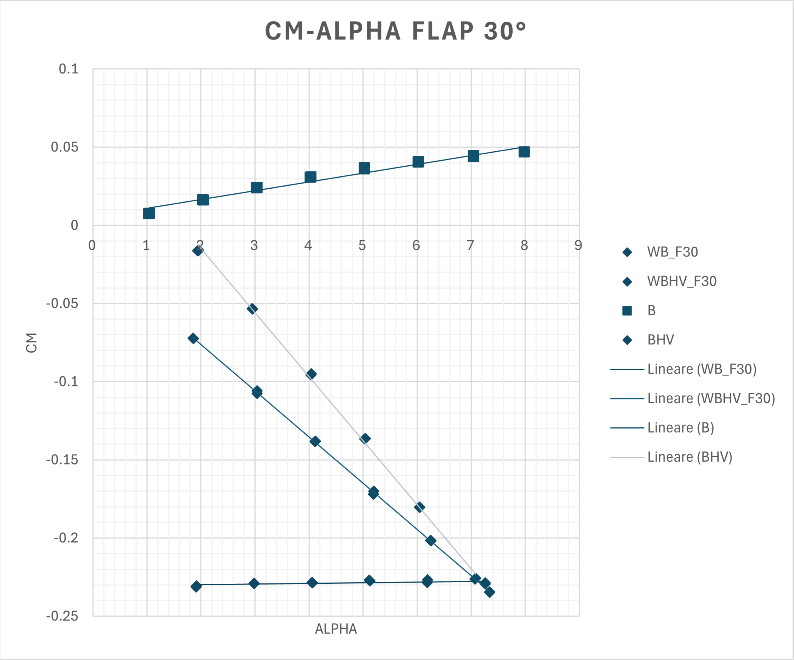

Figure 5.74: *Required derivatives for downwash determination (flaps landing)*

Ta. 5.12 shows a summary of the parameters involved in the analysis. Estimated downwash values are typical for this type of aircraft.

	Flap 0°	**Flap** 20°	**Flap** 30°
$C_{M_{\alpha,B}}$ $(1/deg)$	0.0056	0.0056	0.0056
$C_{M_{\alpha,BHV}}$ $(1/deg)$	−0.0410	−0.0410	−0.0410
$C_{M_{\alpha,WB}}$ $(1/deg)$	0.0048	0.0006	0.0004
$C_{M_{\alpha,WBHV}}$ $(1/deg)$	−0.0287	−0.0294	−0.0296
$\frac{d\epsilon}{d\alpha}$	0.2811	0.3562	0.3562

Table 5.12: *Downwash determination parameters*

5.2.2 Comparison with numerical methods

In the preliminary design phase numerical and experimental data are combined to provide an initial evaluation of the characteristics of the aircraft. Aerodynamic estimation was performed through two different methodologies:

- **Roskam methodology**: this is a preliminary estimation method of the aerodynamic characteristics of an aircraft. It combines semi-empirical formulas and statistical data for the evaluation of the aerodynamic coefficients. The methodology is based on a modular approach. Starting from the geometry definition of the main components of the aircraft (wing, fuselage, tail, ...), aerodynamic coefficients are estimated for the wing using a combination of simplified theories and statistical corrections based on experimental data, even considering the effects of compressibility, Reynolds number, 2-D and 3-D geometric data [12]. The aerodynamic estimation is then carried out on the fuselage, tail, nacelles and other components to provide their contribution. The overall aircraft lift, drag, and moments are obtained by combination of the various effects. Despite the limitation due to the simplifications adopted, the methodology represents an extremely valid and consolidated tool for the preliminary analysis of the aircraft, providing sufficiently accurate results for an initial aerodynamic analysis;

- **VSP Aero**: it is a solver developed by NASA for the preliminary estimation of the flow field around an aircraft. The software is integrated with **OpenVSP**, a parametric modeling environment for the generation of the geometry [17]. The solver directly executes the analysis starting from the geometry provided by OpenVSP, enabling the resolution of the flow field by using either a Vortex Lattice Method (VLM) or a panel method. In the first case, the solver performs the discretization of the geometry with a series of vortices applied on the mean camber surfaces, enabling the calculation of the flow field and consequently the overall aerodynamic characteristics of the aircraft from potential theory. This methodology does not consider the effect of thickness in the calculation, modeling the lifting surfaces as "sheets" and the fuselage as intersections of two flat surfaces. In the second case, tridimensional geometry is divided into a number of panels on which doublets are applied, enabling the resolution of the potential flow field. The latter methodology is more accurate as the panel discretization allows the modeling of complex geometries. Both methods are based on the potential flow theory which assumes inviscid flow; as a consequence, there are significant limitations in estimating drag and flow separation at stall conditions. Nevertheless, the tool is widely adopted for the preliminary estimation of aerodynamic performance.

Comparison with numerical result is performed on the complete aircraft with flaps retracted, comparing the C_L versus α, C_M versus α and C_M versus C_L curves, considering also the effect of elevator deflection. Focusing on the case with elevator in neutral position, good correlation between numerical and experimental data is achieved on lift, with minimum difference in the slope.

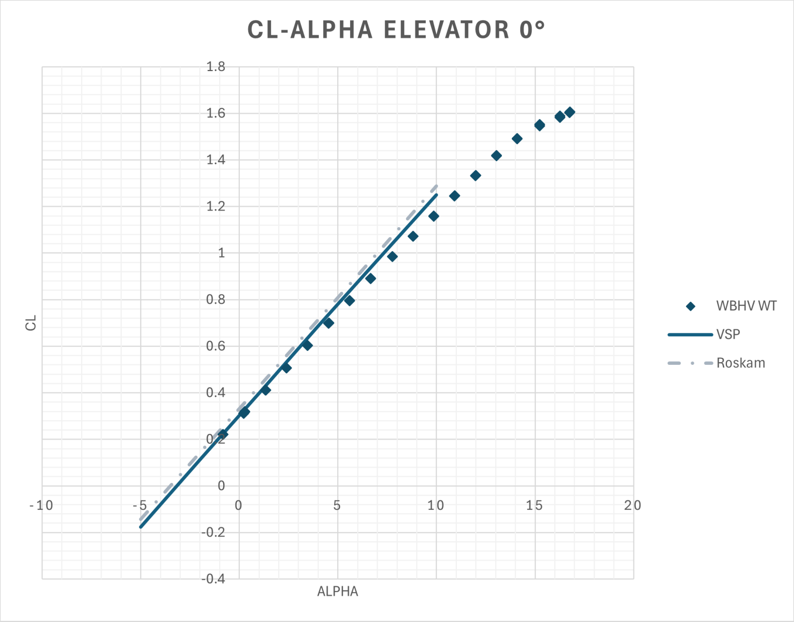

Figure 5.75: *Numerical and experimental results:* C_L *versus* α *at elevator* $0°$

The C_M versus α shows great agreement with experimental results throughout the linear range. Looking at figure 5.76, Roskam method is slightly less accurate in predicting aerodynamic derivatives compared to VSPAero.

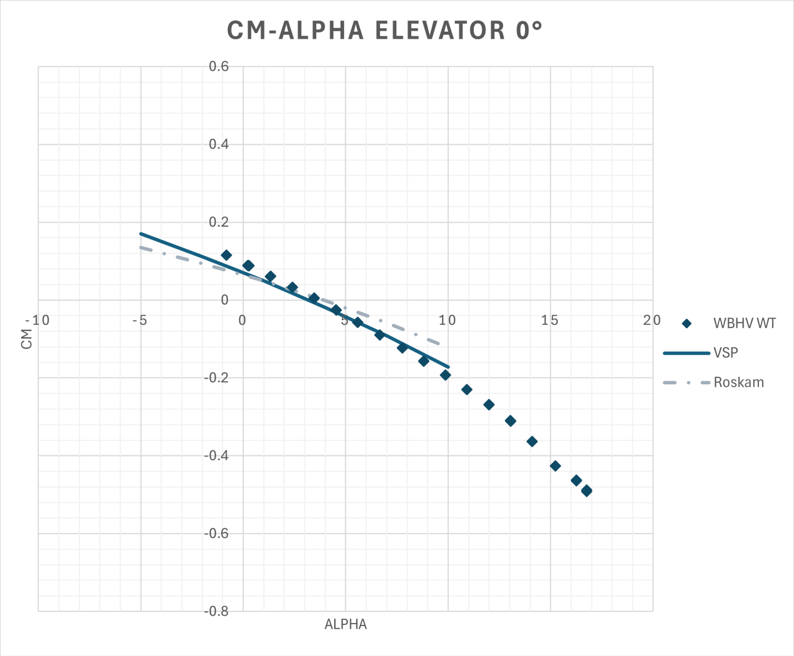

Figure 5.76: *Numerical and experimental results:* C_M *versus* α *at elevator* $0°$

Similar considerations can be made for C_M versus C_L curves. The static stability margin is predicted with sufficient accuracy, especially by VSPaero, with a $C_{M_{C_L}}$ of -0.219 compared to the -0.32 obtained experimentally.

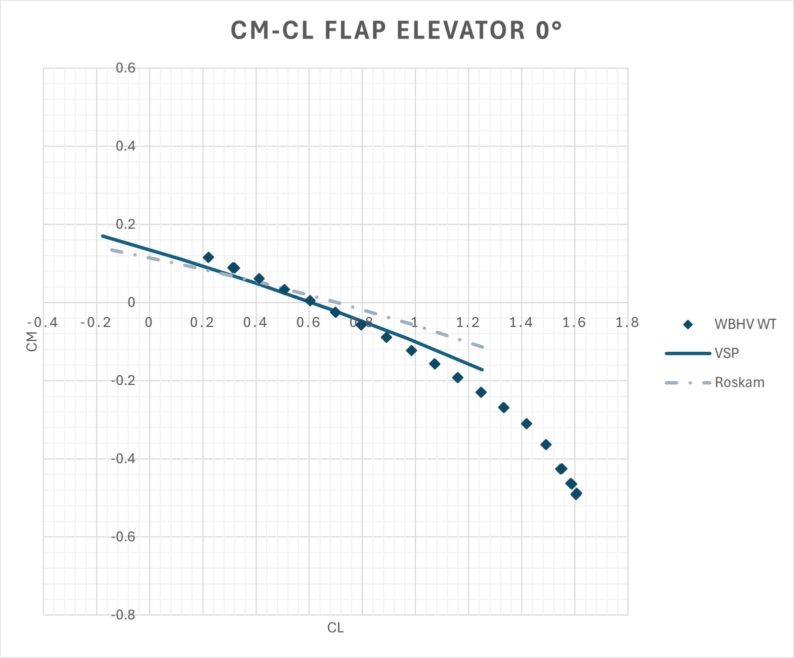

Figure 5.77: Numerical and experimental results: C_M *versus* C_L *at elevator* $0°$

The comparison between numerical and experimental results on the effect of the elevator is then performed for a deflection of $-10°$.

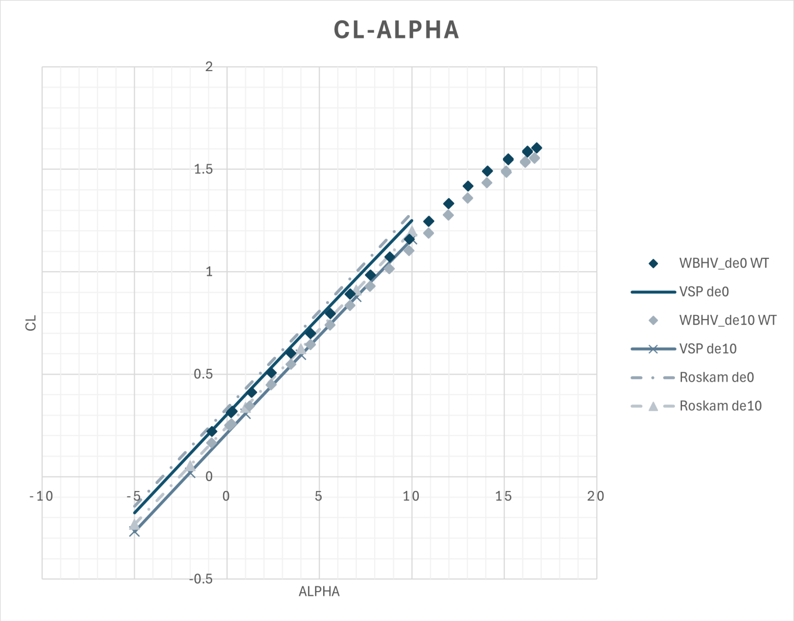

Figure 5.78: Numerical and experimental results: C_L *versus* α *for different elevator deflection*

The lift curves are well predicted by both methods. The loss of lift due to the elevator deflection is estimated with sufficient accuracy, even though numerical data overestimate the offset of the curves produced by the control surface.

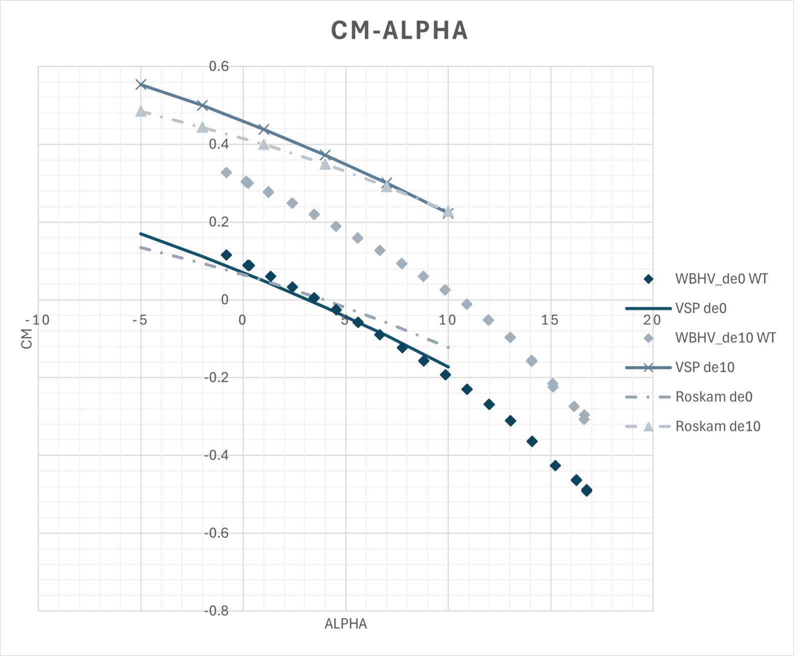

Figure 5.79: Numerical and experimental results: C_M versus α for different elevator deflection

The same trend is observable in the C_M versus C_L comparison plot. $C_{M_{\delta_e}}$ calculated by Roskam and VSP is larger compared to the value obtained from wind tunnel testing.

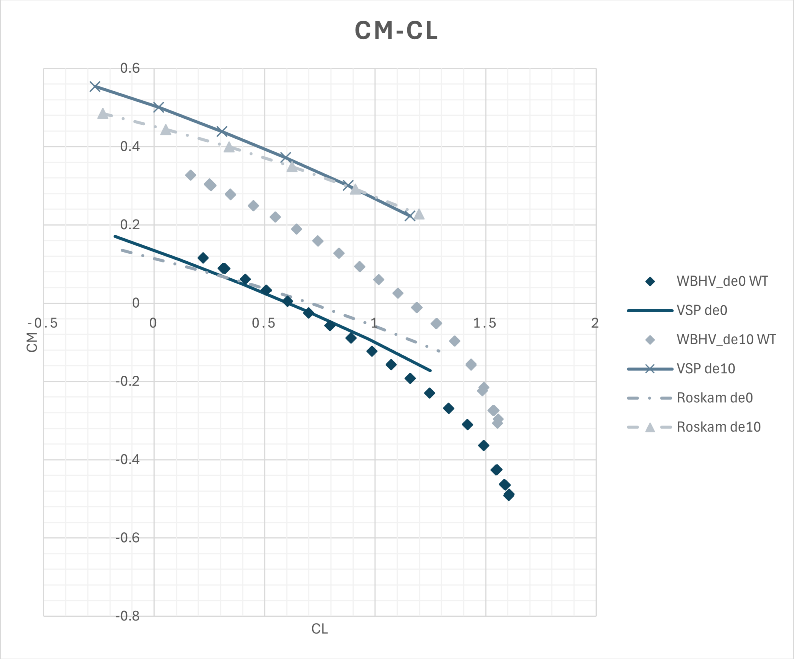

Figure 5.80: Numerical and experimental results: C_M versus C_L for different elevator deflection

Predictions performed by preliminary estimation tools are consistent with the accuracy achievable. Furthermore, numerical analysis are carried out considering the full scale aircraft, thus Reynolds and Mach differences affect the accuracy of the methods. Table 5.13 provides the list of the main aerodynamic coefficients considered for the comparison:

	WT 0°	**VSP** 0°	**Roskam** 0°	**WT** 10°	**VSP** 10°	**Roskam** 10°
C_{L_α} $(1/deg)$	0.0895	0.0952	0.0954	0.0899	0.0951	0.0954
$C_{\mathcal{M}_\alpha}$ $(1/deg)$	−.0287	−0.0228	−0.0171	−0.0283	−0.221	−0.0171
$C_{\mathcal{M}_{C_L}}$ $(1/deg)$	−0.3205	−0.2192	−0.1582	−0.3146	−0.2110	−0.1582
$C_{\mathcal{M}_0}$	0.1960	0.1339	0.1183	0.3890	0.5022	0.4524
$C_{\mathcal{M}_{\delta_e}}$	−	−	−	−0.0193	−0.0366	−0.0334
$C_{L_{\delta_e}}$	−	−	−	0.0057	0.0091	0.0089

Table 5.13: *Numerical and experimental aerodynamic parameters*

5.3 Lateral-directional coefficients, stability and control

Lateral-directional analysis focuses on the yawing and rolling moments, as well as side-force, generated by various features of the aircraft due to a sideslip angle β. Regarding directional static stability, a positive derivative $C_{\mathcal{N}_\beta}$ is required to grant that in case of $\beta > 0$ (wind from pilot's right to left), a restoring moment arises to align the body x-axis to the wind x-axis.

The definition of a positive deflection of the rudder implies that a negative yawing moment must be generated, that is, $C_{\mathcal{N}_{\delta_r}} < 0$.

Ailerons can also affect directional equilibrium, but since the model was not equipped with them, no results were reported. Usually, $C_{\mathcal{N}_{\delta_a}} > 0$ as the positive deflection of the ailerons causes a loss of induced drag on the left wing and an increase on the right wing.

A similar breakdown can be applied to the rolling moment. An aircraft, stable with respect to roll, shows $C_{\mathcal{L}_\beta} < 0$. This implies that if a perturbation causes the aircraft to lower its right wing (positive roll) and consequently sink because of a vertical non-equilibrium condition ($L < W$), the positive sideslip generates a negative rolling moment that levels the wing, restoring the original attitude and lifting capabilities.

Regarding $C_{\mathcal{L}_{\delta_a}}$, it has to be negative, for reasons similar to $C_{\mathcal{N}_{\delta_r}}$.

$C_{\mathcal{L}_{\delta_r}} > 0$, since positive rudder deflection generates a negative side-force on the vertical tail that causes a positive rolling moment, as its center of pressure is above the center of gravity.

In the plots below, $C_{\mathcal{L}}$ is referred to as C_{Roll} to avoid confusion with the lift coefficient. The slopes were calculated considering the range $\beta \in [0°, 10°]$ and all the tests were carried out with the seaplane at $\alpha = 0°$.

5.3.1 Test results

Configurations effect

In this section, the influence of the different elements of the seaplane on the lateral-directional equilibrium is investigated, considering cruise condition and no deflection of the control surfaces.

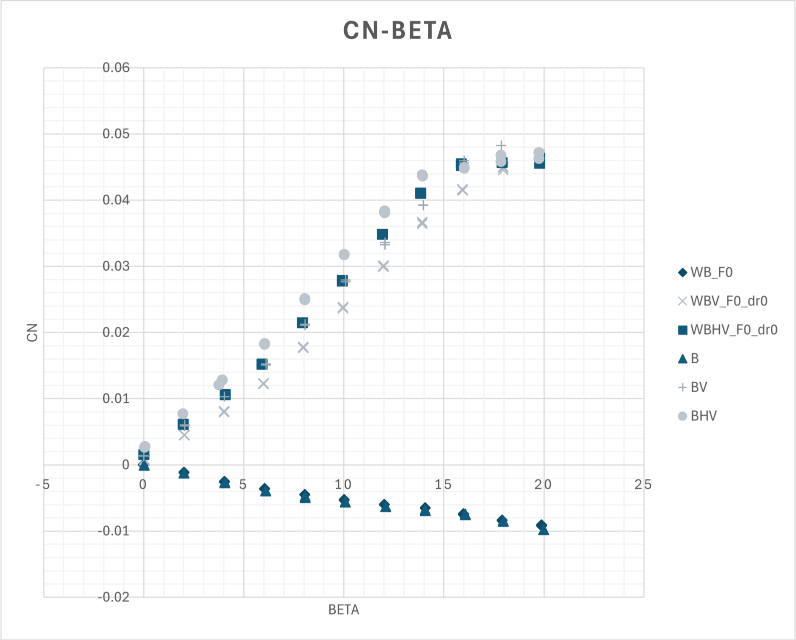

Figure 5.81: Effects of the configuration on the $C_N - \beta$ curve

The most unstable condition with respect to yaw is caused by the fuselage, which is an unstable component of the aircraft even in inviscid Munk's theory, as already seen for the longitudinal equilibrium. Adding the wing has small impact on directional stability, with a minimal increase (less negative) of C_{N_β} due to the pressure build-up caused by the wing slightly behind the center of gravity on the exposed side. The main stabilizing effect is clearly generated by the vertical stabilizer.

Wing contribution on the Body-Vertical configuration shows an opposing behaviour compared to configurations without the vertical tail. However, this is perfectly coherent with the flow field, as the additional presence of the wing straightens the air reducing the effective sideslip at the tail, that is: $\beta(1 - \frac{\delta\sigma}{\delta\beta})$[1].

The attitude is preserved when mounting the horizontal tail, which allows to spot another phenomenon: the endplate effect. The horizontal stabilizer improves the behaviour of the vertical tail, increasing C_{N_β}, because the pressure zones on the latter are more isolated from each other, increasing the pressure peaks. Furthermore, the horizontal stabilizer stops the flow from going upwards towards the vertical tip, reducing tip vortex intensity

---

[1] Note that for a vertical surface, sideslip appears as the angle of attack.

and increasing pressure on the exposed side of the rudder. The latter effect is similar to the blockage caused by the wing on the airflow trying to climb over the fuselage.

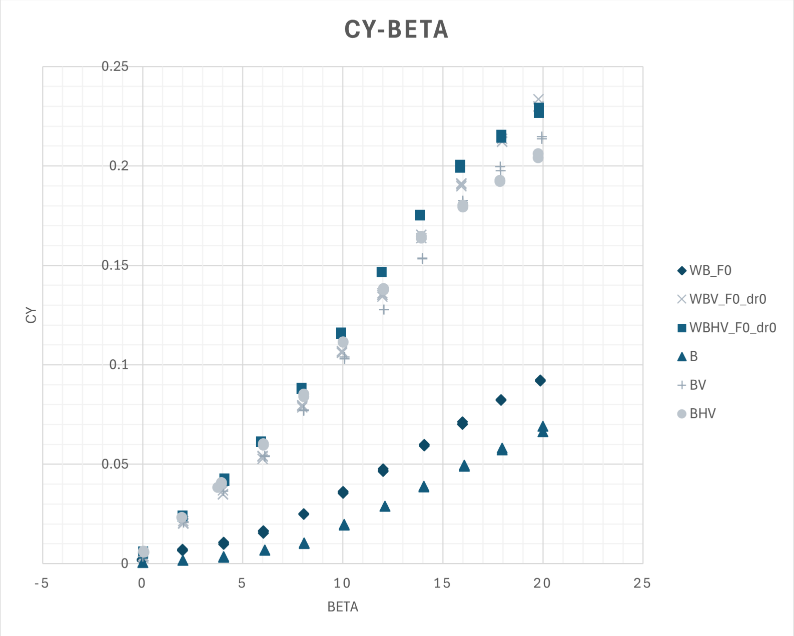

Figure 5.82: *Effects of the configuration on the $C_Y - \beta$ curve*

It is of particular interest to pair this directional stability analysis with the contributions to side-force to extensively explain its physics. Looking at the plot, the effect of the wing on fuselage stability appears negligible because of the very small lever, not because it adds little side-force. As shown, the vertical stabilizer strongly increases C_{Y_β}; this, paired with its longitudinal position, explains the even higher increase of the yawing moment coefficient. Adding the horizontal tail always increases the side-force, as expected from previous considerations, just like the wing. The side-force added by the wing more than offsets the amount lost at the tail, but this likely reduces the contribution of the vertical stabilizer, causing the decrease of the yawing moment arm to outweigh the increase in lateral force.

The rolling moment derivative of the isolated body is slightly positive mainly because of the shape of the sections. The upper part is rounded, allowing flow expansion, whereas the lower is flat and sharp, causing pressure build-up on the exposed side and separation on the other. Mounting the wing strongly increases stability due to both the geometric and effective dihedral, that is the apparent increase in dihedral angle due to the upwash caused by the airflow trying to climb over the fuselage around the wing location. A wing with no dihedral paired to a fuselage sees a normal component of velocity in sideslip flow, which is equal to the normal component observed on the isolated wing with non-zero dihedral. In all three plots, no clear "stall" can be noticed if the vertical tail is missing, with a linear behaviour throughout the range of β. When the vertical tail is added, the lateral stability increases, but the stall is more abrupt without the wing, as happens in

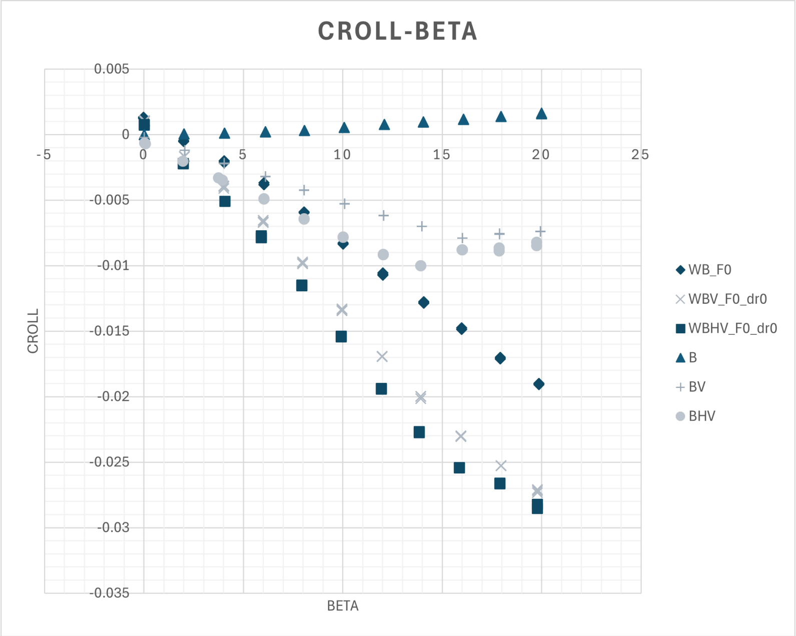

Figure 5.83: *Effects of the configuration on the* $C_{\mathcal{L}} - \beta$ *curve*

directional equilibrium, because the effective sideslip seen by the vertical tail is higher without the main lifting surface. Similarly to the other coefficients, performance increases when mounting the horizontal tail because of the endplate effect.

	WBHV	**WBV**	**WB**	**BHV**	**BV**	**B**
C_{Y_0}	0.0008	−0.0011	−0.0004	0.0012	0.0006	−0.0180
C_{Y_β} $(1/deg)$	0.0110	0.0102	0.0033	0.0105	0.0097	0.0018
$C_{\mathcal{N}_0}$	0.0060	−0.0003	−0.0001	0.0017	0.0005	−0.0020
$C_{\mathcal{N}_\beta}$ $(1/deg)$	0.0026	0.0023	−0.0005	0.0029	0.0026	−0.0006
$C_{\mathcal{L}_0}$	0.0011	0.0014	0.0015	−0.0060	−0.0002	0.0000
$C_{\mathcal{L}_\beta}$ $(1/deg)$	−0.0015	−0.0014	−0.0009	−0.0007	−0.0050	0.0001

Table 5.14: *Lateral-directional aerodynamic derivatives and zero-intercepts*

Considering the first three columns, the contributions of the main components of the aircraft to lateral-directional stability derivatives can be extracted for the clean configuration.

	WB	**V**	**H**
C_{Y_β} $(1/deg)$	0.0033(30%)	0.0069(63%)	0.0008(7%)
$C_{\mathcal{N}_\beta}$ $(1/deg)$	−0.0005	0.0028(90%)	0.0003(10%)
$C_{\mathcal{L}_\beta}$ $(1/deg)$	−0.0009(60%)	−0.0005(33%)	−0.0001(7%)

Table 5.15: *Contributions of the various components to the lateral-directional stability derivatives*

Flaps effect

Changing features of the aircraft linked to the longitudinal characteristics can somehow also impact lateral-directional equilibrium, since the perturbations are not small anymore and Bryan hypotheses can not be considered entirely valid. As shown in the longitudinal analysis, flaps mainly affect lift, drag and pitching moment coefficients, but increasing the lifting capabilities of the wing with those means changing the geometry, that is the effect of the wing itself, as well as modifying existent interactions between the components.

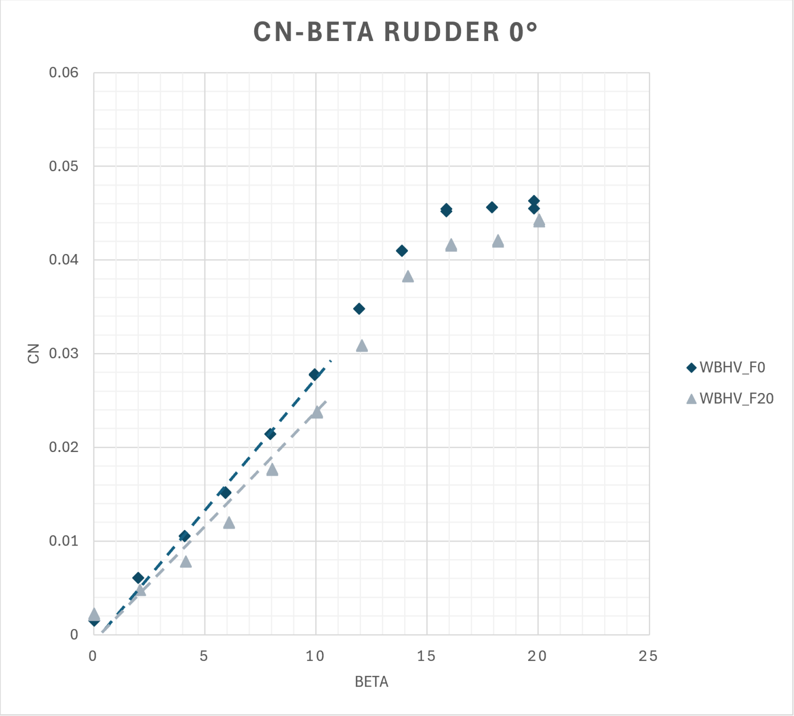

Figure 5.84: *Effects of flaps on the $C_N - \beta$ curve*

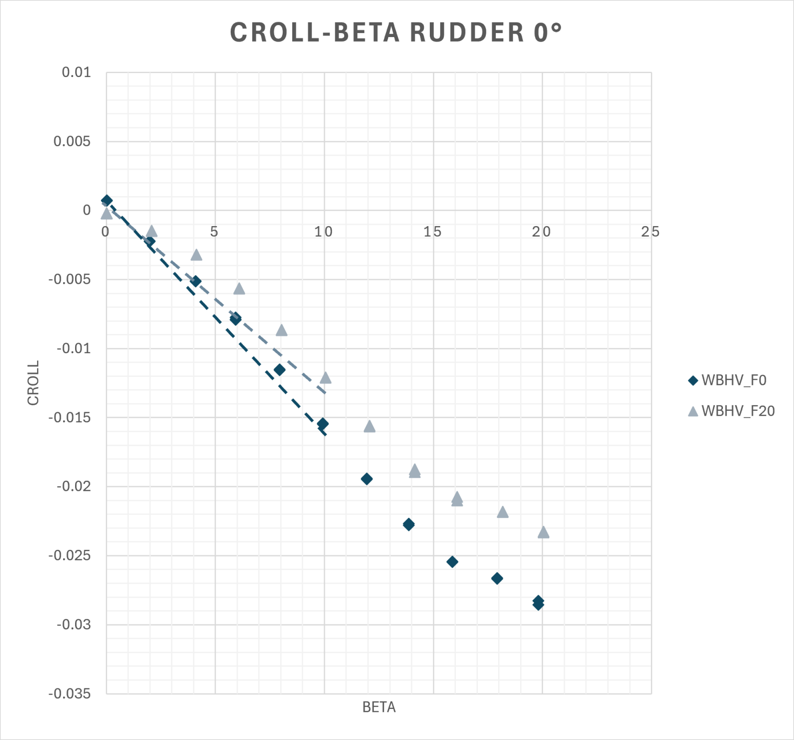

Figure 5.85: *Effects of flaps on the* $C_{\mathcal{L}} - \beta$ *curve*

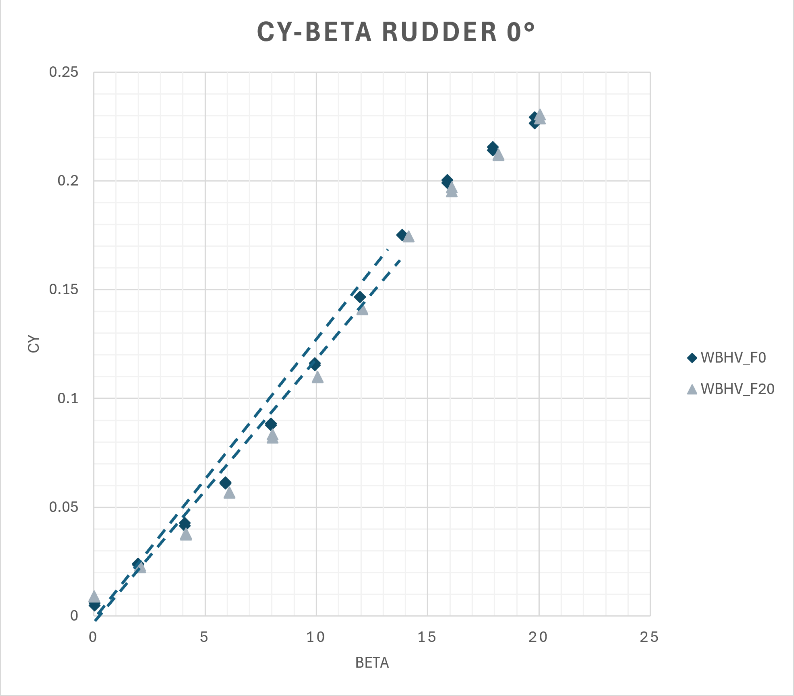

Figure 5.86: *Effects of flaps on the* $C_Y - \beta$ *curve*

	WBHV_F0	WBHV_F20
C_{Y_0}	0.0008	0.0023
C_{Y_β} $(1/deg)$	0.0110	0.0100
$C_{\mathcal{N}_0}$	0.0006	0.0005
$C_{\mathcal{N}_\beta}$ $(1/deg)$	0.0026	0.0021
$C_{\mathcal{L}_0}$	0.0011	0.0008
$C_{\mathcal{L}_\beta}$ $(1/deg)$	−0.0015	−0.0012

Table 5.16: *Effect of the flaps on lateral-directional derivatives and zero-intercepts*

The plots show a small decrease of yaw and roll stability, mainly caused by the tip vortex of the inner flap disturbing the root of the vertical stabilizer. This causes a slight reduction in lateral-directional authority, with a variation of -19% for $C_{\mathcal{N}_\beta}$ and -20% for $C_{\mathcal{L}_\beta}$. The side-force lost at the tail is almost compensated by the increased pressure difference between the two sides of the fuselage caused by the flaps, with a slight change of the C_Y slope, which shows $\%\Delta C_{Y_\beta} = -9.1\%$.

Rudder effect

The following is the core of the lateral-directional stability analysis, the rudder being the surface dedicated to directional control, with a relevant contribution to the yawing moment.

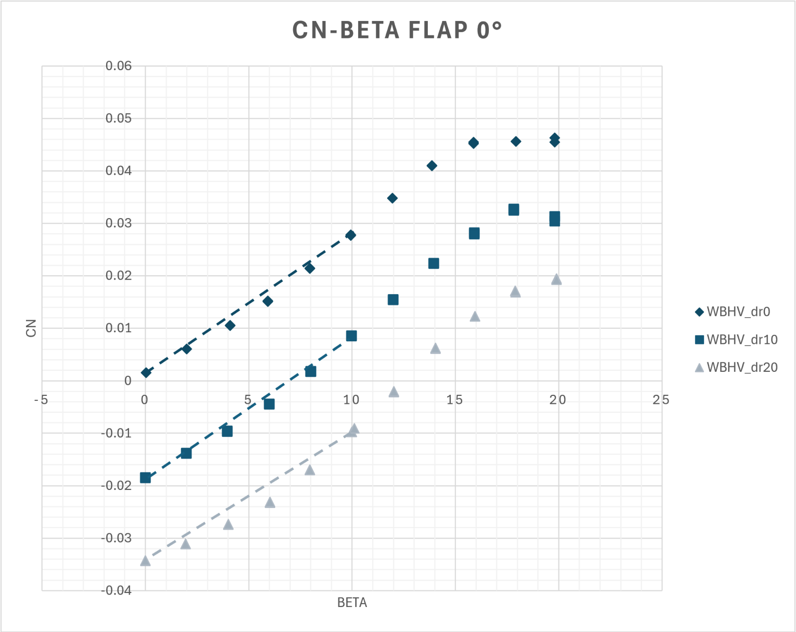

Figure 5.87: *Effects of the rudder on the $C_{\mathcal{N}} - \beta$ curve (flaps cruise)*

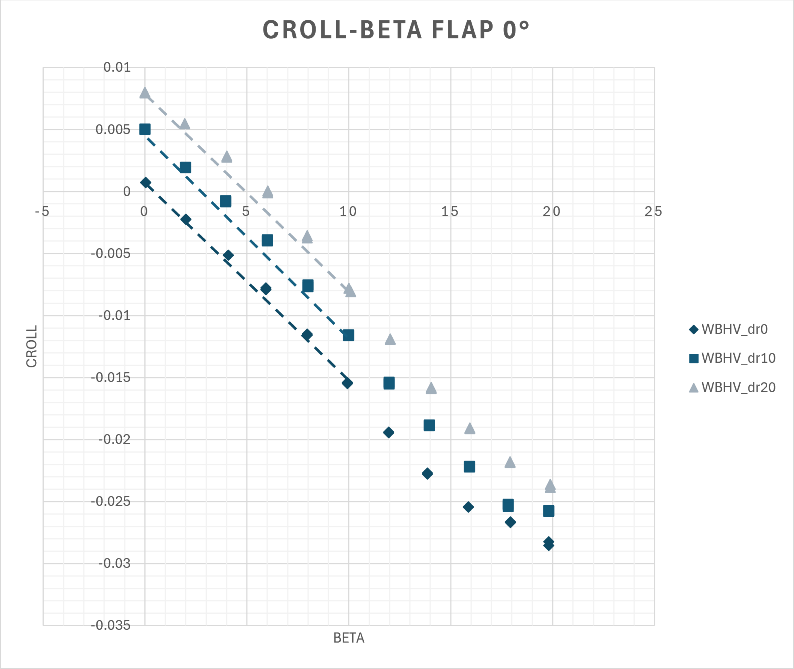

Figure 5.88: *Effects of the rudder on the* $C_{\mathcal{L}} - \beta$ *curve (flaps cruise)*

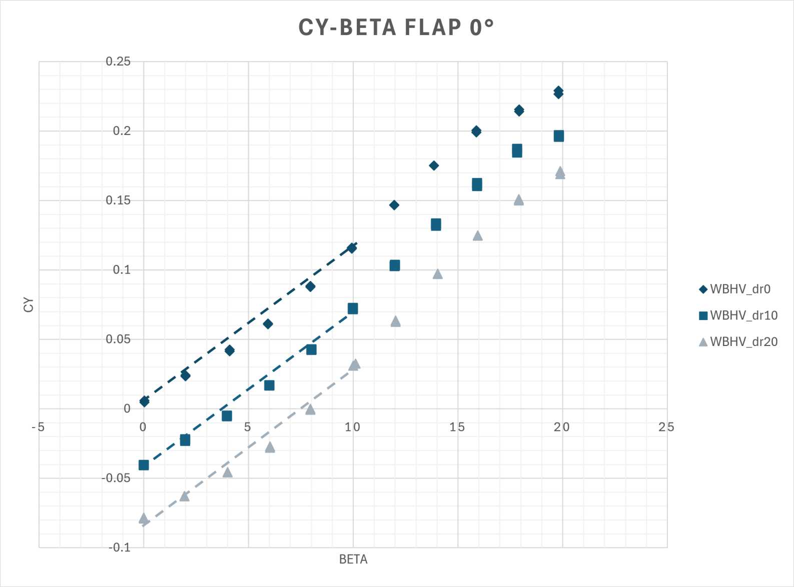

Figure 5.89: *Effects of the rudder on the* $C_Y - \beta$ *curve (flaps cruise)*

	WBHV_F0_dr0	**WBHV_F0_dr10**	**WBHV_F0_dr20**
C_{Y_0}	0.0008	-0.0453	-0.0833
C_{Y_β} $(1/deg)$	0.0110	0.0111	0.0104
$C_{Y_{\delta r}}$ $(1/deg)$	-	-0.0046	-0.0042
$C_{\mathcal{N}_0}$	0.0060	-0.0194	-0.0356
$C_{\mathcal{N}_\beta}$ $(1/deg)$	0.0026	0.0027	0.0023
$C_{\mathcal{N}_{\delta r}}$ $(1/deg)$	-	-0.0020	-0.0018
$C_{\mathcal{L}_0}$	0.0011	0.0054	0.0085
$C_{\mathcal{L}_\beta}$ $(1/deg)$	-0.0016	-0.0016	-0.0015
$C_{\mathcal{L}_{\delta r}}$ $(1/deg)$	-	0.0004	0.0004

Table 5.17: *Effect of the rudder on lateral-directional derivatives and zero-intercepts (flaps cruise)*

The tests investigate the contribution of the rudder in cruise conditions, where it can be actuated to adjust attitude and turn. It mainly alters not the slope, but the zero-intercept of the curves. The effect on the curves is sufficiently linear, with an almost constant offset due to successive 10° deflections. Deflecting the rudder allows trimming the aircraft at a maximum β of 12.5°, confirming the effectiveness of the vertical tail but settling it near the lower acceptable limit.

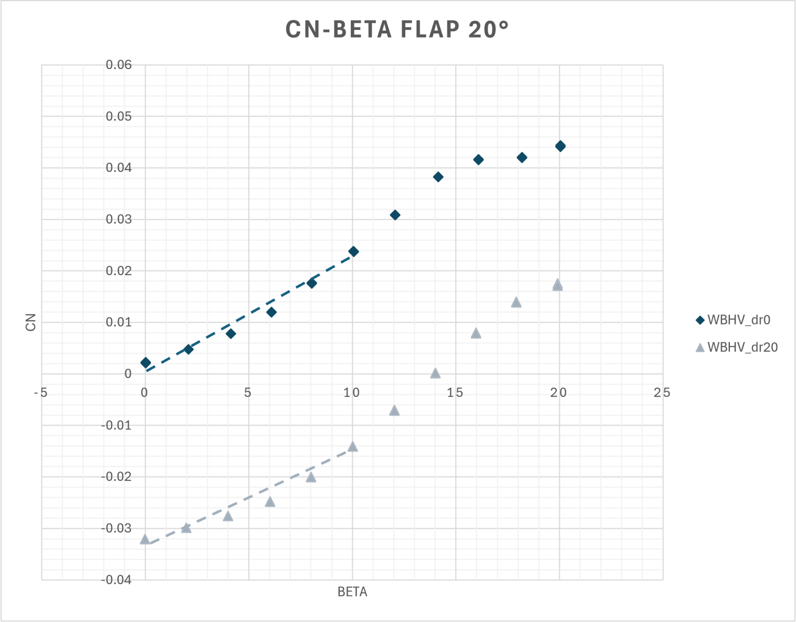

Figure 5.90: *Effects of the rudder on the $C_{\mathcal{N}} - \beta$ curve (flaps take-off)*

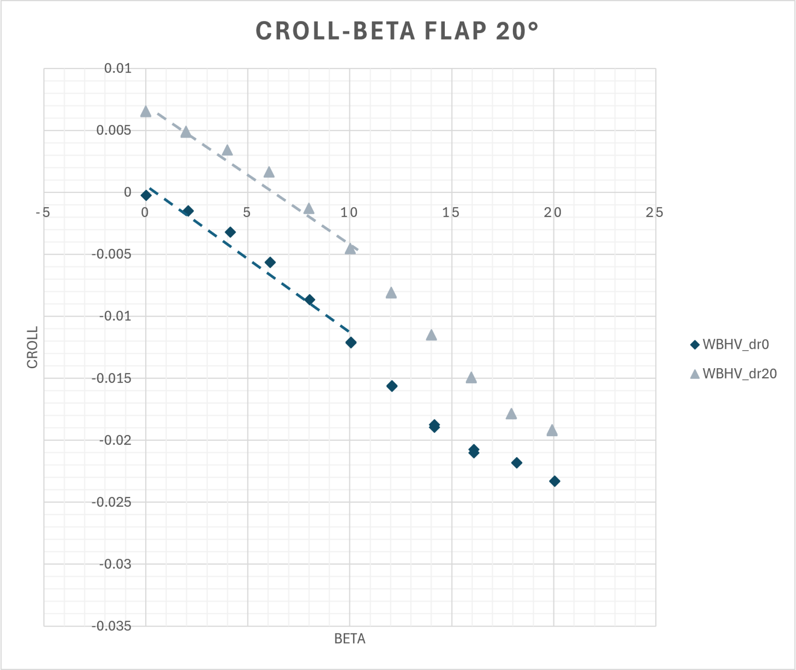

Figure 5.91: *Effects of the rudder on the* $C_{\mathcal{L}} - \beta$ *curve (flaps take-off)*

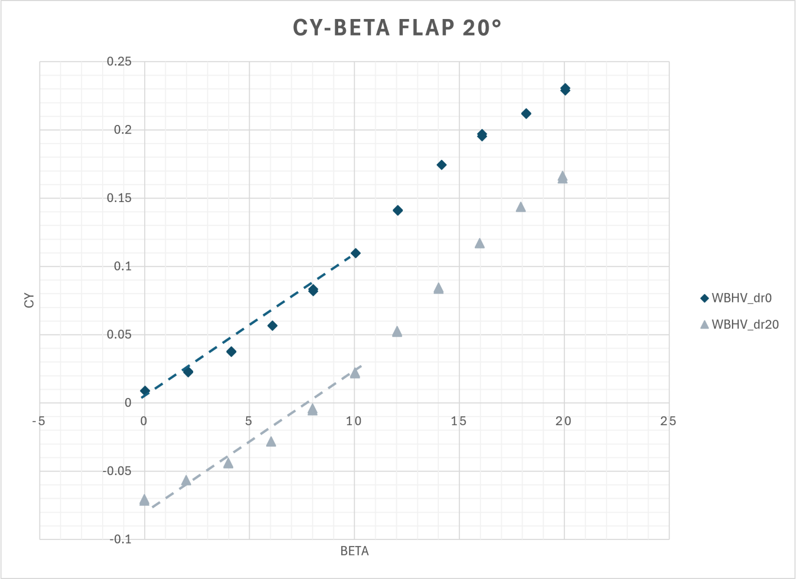

Figure 5.92: *Effects of the rudder on the* $C_Y - \beta$ *curve (flaps take-off)*

	WBHV_F20_dr0	**WBHV_F20_dr20**
C_{Y_0}	0.0023	-0.0756
C_{Y_β} $(1/deg)$	0.0100	0.0091
$C_{Y_{\delta r}}$ $(1/deg)$	-	-0.0039
$C_{\mathcal{N}_0}$	0.0005	-0.0334
$C_{\mathcal{N}_\beta}$ $(1/deg)$	0.0021	0.0017
$C_{\mathcal{N}_{\delta r}}$ $(1/deg)$	-	-0.0017
$C_{\mathcal{L}_0}$	0.0008	0.0072
$C_{\mathcal{L}_\beta}$ $(1/deg)$	-0.0012	-0.0011
$C_{\mathcal{L}_{\delta r}}$ $(1/deg)$	-	-0.0003

Table 5.18: *Effect of the rudder on lateral-directional derivatives and zero-intercepts (flaps take-off)*

A positive deflection of the rudder, generates a negative side-force, as the pressure on the right side decreases. This also affects the flow field during a positive sideslip, where the right side is the exposed one; here the high pressure due to sideslip is mitigated by the deflection of the rudder, which causes an acceleration of the air and reduction of the hinge moment. For the test model, the control derivative changes between the two flap configurations, again due to the flap vortex and wing wake disturbing the flow field around the root of the vertical tail, altering rudder effectiveness mainly by $C_{\mathcal{L}_{\delta r}}$, decreased by 13.5% in take-off. The aircraft is able to trim up to $\beta = 14°$.

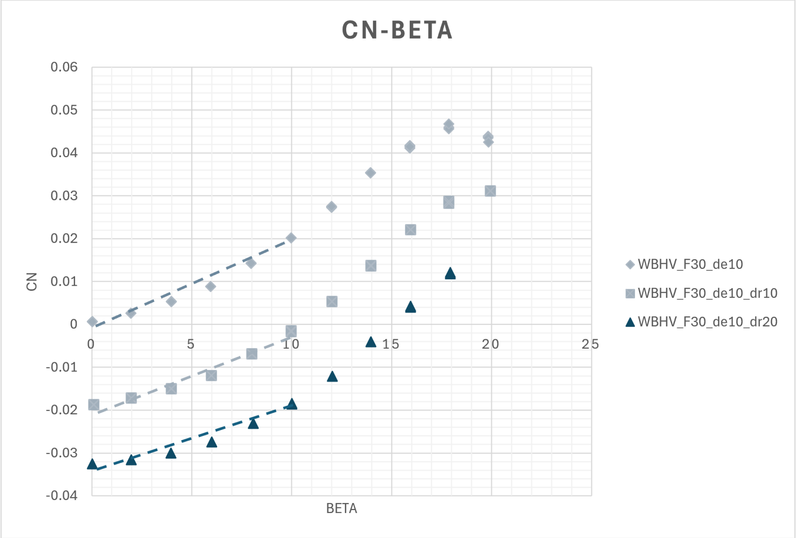

Figure 5.93: *Effects of the rudder on the $C_N - \beta$ curve (flaps landing, $\delta_e = -10°$)*

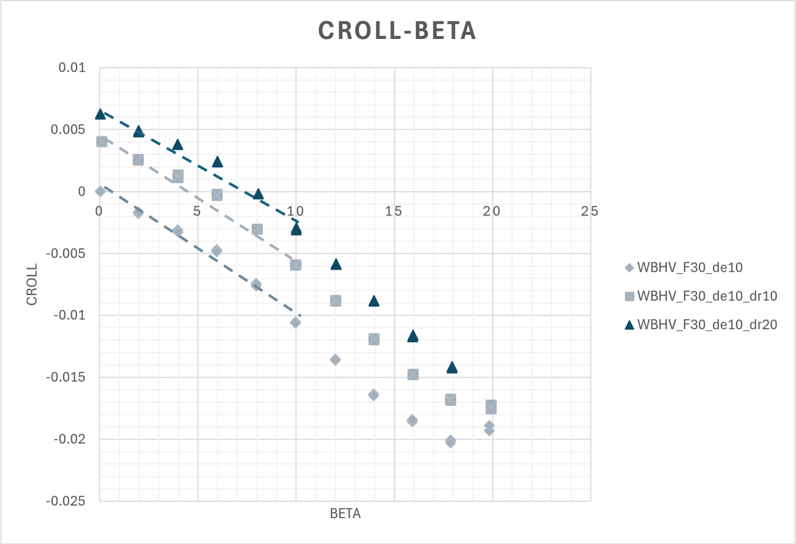

Figure 5.94: *Effects of the rudder on the* $C_{\mathcal{L}} - \beta$ *curve (flaps landing,* $\delta_e = -10°$*)*

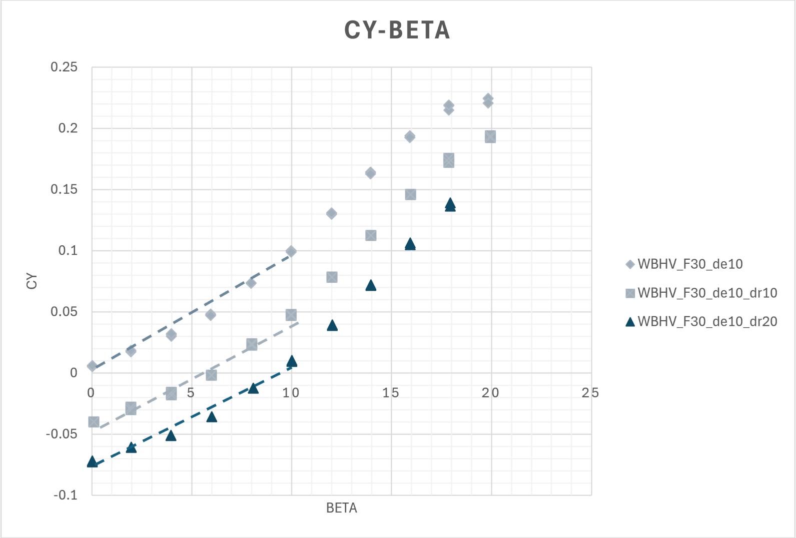

Figure 5.95: *Effects of the rudder on the* $C_Y - \beta$ *curve (flaps landing,* $\delta_e = -10°$*)*

	WBHV_F30_dr0	**WBHV_F30_dr10**	**WBHV_F30_dr20**
C_{Y_0}	-0.0005	-0.0465	-0.0776
C_{Y_β} $(1/deg)$	0.0093	0.0088	0.0081
$C_{Y_{\delta r}}$ $(1/deg)$	-	-0.0046	-0.0039
$C_{\mathcal{N}_0}$	-0.0001	-0.0205	-0.0342
$C_{\mathcal{N}_\beta}$ $(1/deg)$	0.0019	0.0017	0.0014
$C_{\mathcal{N}_{\delta r}}$ $(1/deg)$	-	-0.0020	-0.0017
$C_{\mathcal{L}_0}$	0.0005	0.0047	0.0069
$C_{\mathcal{L}_\beta}$ $(1/deg)$	-0.001	-0.001	-0.0009
$C_{\mathcal{L}_{\delta r}}$ $(1/deg)$	-	-0.0004	-0.0003

Table 5.19: *Effect of the rudder on lateral-directional derivatives and zero-intercepts (flaps landing, $\delta_e = -10°$)*

In windy days, OEI[2] or other conditions, the rudder can undergo large deflections even during take-off and landing. To simulate this, the test has been carried out with flaps in landing configuration and a negative deflection of the elevator of $-10°$. Having the flaps completely extended, the disturbance to the tail becomes non-negligible, with a stronger non-linear trend of the control derivatives. In fact, $C_{Y_{\delta r}}$ and $C_{\mathcal{N}_{\delta r}}$ are reduced by 15% at $\delta_r = 20°$ and $C_{\mathcal{L}_{\delta r}}$ by 25%. The rudder in this configuration can trim the aircraft at values of β up to 15°.

---

[2] One Engine Inoperative

Floats effect

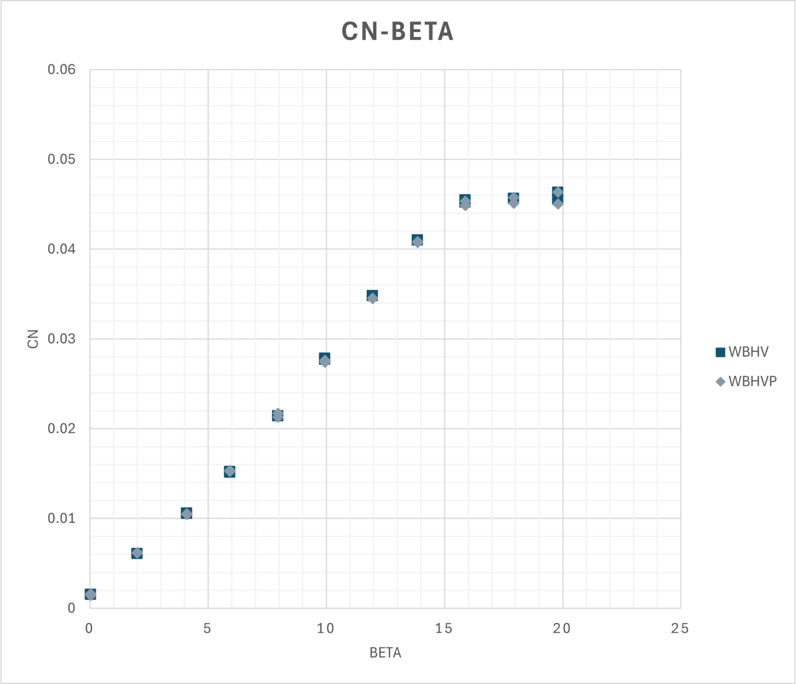

Figure 5.96: *Effects of the floats on the* $C_{\mathcal{N}} - \beta$ *curve*

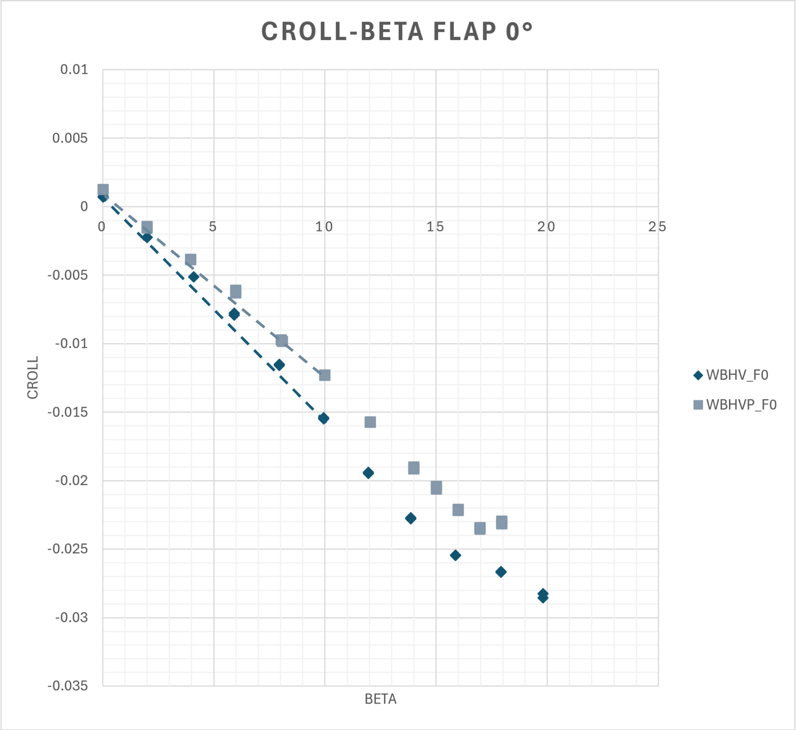

Figure 5.97: *Effects of the floats on the* $C_{\mathcal{L}} - \beta$ *curve*

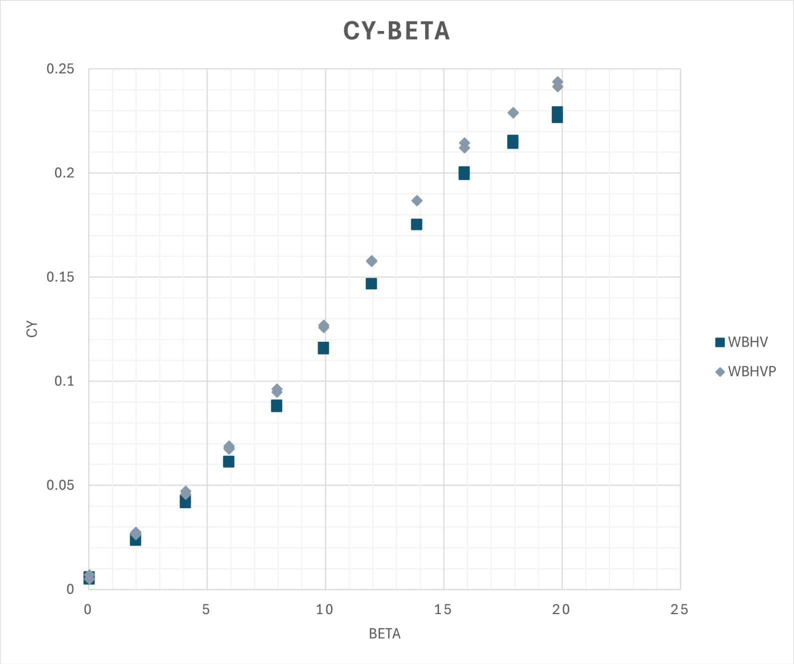

Figure 5.98: *Effects of the floats on the* $C_Y - \beta$ *curve*

	WBHV	WBHVP
C_{Y_0}	0.0008	0.0016
C_{Y_β} $(1/deg)$	0.0110	0.0119
$C_{\mathcal{N}_0}$	0.0006	0.0007
$C_{\mathcal{N}_\beta}$ $(1/deg)$	0.0026	0.0026
$C_{\mathcal{L}_0}$	0.0011	0.0010
$C_{\mathcal{L}_\beta}$ $(1/deg)$	−0.0016	−0.0015

Table 5.20: *Effects of the floats on lateral-directional derivatives and zero-intercepts (cruise)*

The floats have a slight impact on the lateral-directional behaviour, with variations on the maximum coefficients of side-force and roll of only 4% and 7%; derivatives are not particularly affected as well. The slightly increased values along the curves are due to the additional side-force acting on the floats and a disturbance to the dihedral effect of the wing.

5.3.2 Comparison with numerical methods

Following the path of the longitudinal analysis, results of the tests are compared to the available preliminary numerical data, considering flaps retracted. Lateral-directional physics is difficult to represent reliably for inviscid numerical methods, since the flow around the fuselage can change non-negligibly due to viscosity, mainly because of the cross-flow separation which modifies the position of the lateral center of pressure. Moreover, vortices and separation on the surfaces are complicated to handle for inviscid solvers, and their interaction with other surfaces are often treated poorly, over-estimating stability derivatives.

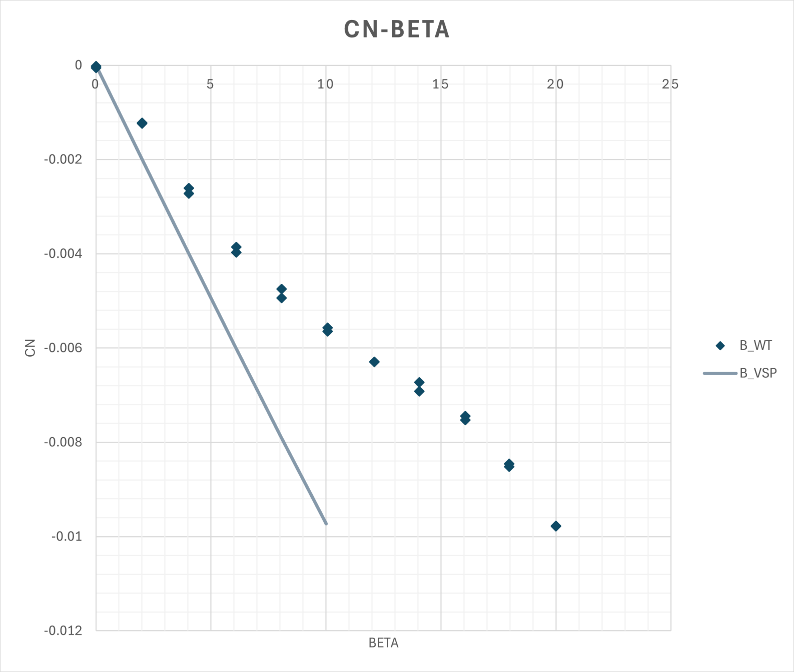

Figure 5.99: Comparison between numerical and experimental data of the fuselage $C_N - \beta$ curves

	$C_{N_\beta}(1/deg)$ (1/deg)
B_WT	-0.0006
B_VSP	-0.0010

Table 5.21: Comparison of the directional stability between numerical and experimental data of the fuselage

The isolated fuselage shows a 40% less unstable behaviour during the test. This is likely caused by the low pressure on the hidden side, which at the aft sections decreases the absolute yawing moment compared to VSPAero.

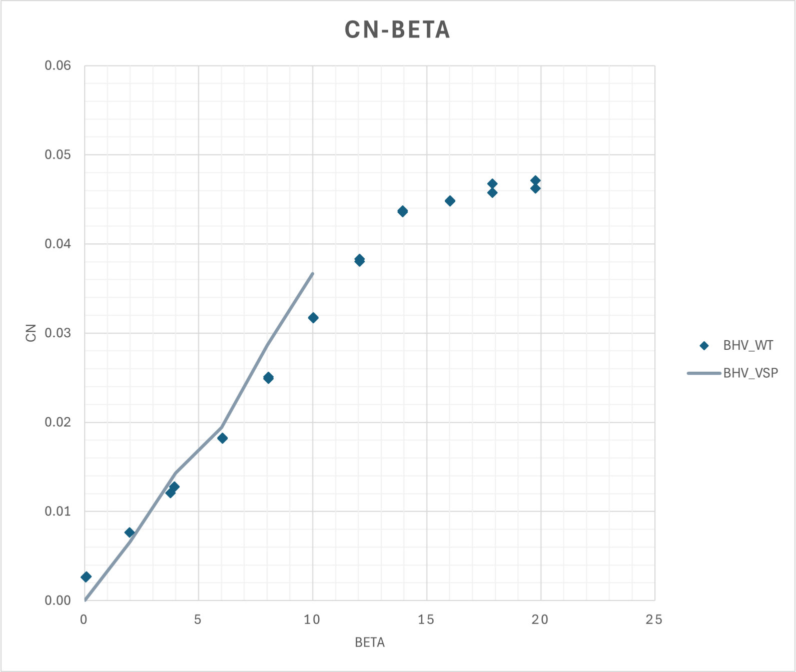

Figure 5.100: *Comparison between numerical and experimental data of the Body-Tail* $C_{\mathcal{N}} - \beta$ *curves*

	$C_{\mathcal{N}_\beta}(1/deg)$ (1/deg)
BHV_WT	0.0029
BHV_VSP	0.0036

Table 5.22: *Comparison of the directional stability between numerical and experimental data of the Body-Tail configuration*

Mounting the tail shows more correlation between the two sets of data. The curves share much similar trends, however the numerical prediction is slightly optimistic on the stability throughout the range of simulated β, considering a 24% increase of the $C_{\mathcal{N}_\beta}$.

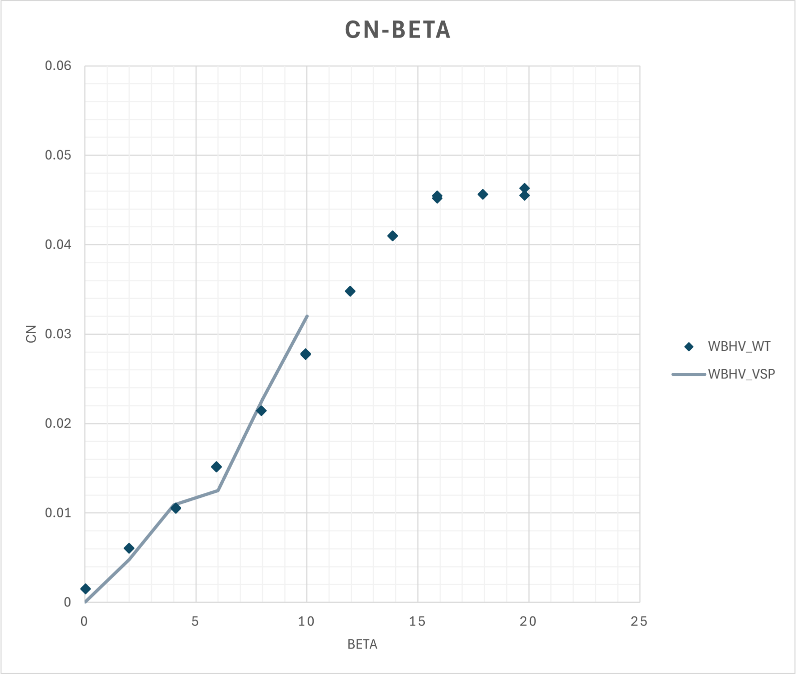

Figure 5.101: *Comparison between numerical and experimental data of the complete aircraft* $C_{\mathcal{N}} - \beta$ *curves*

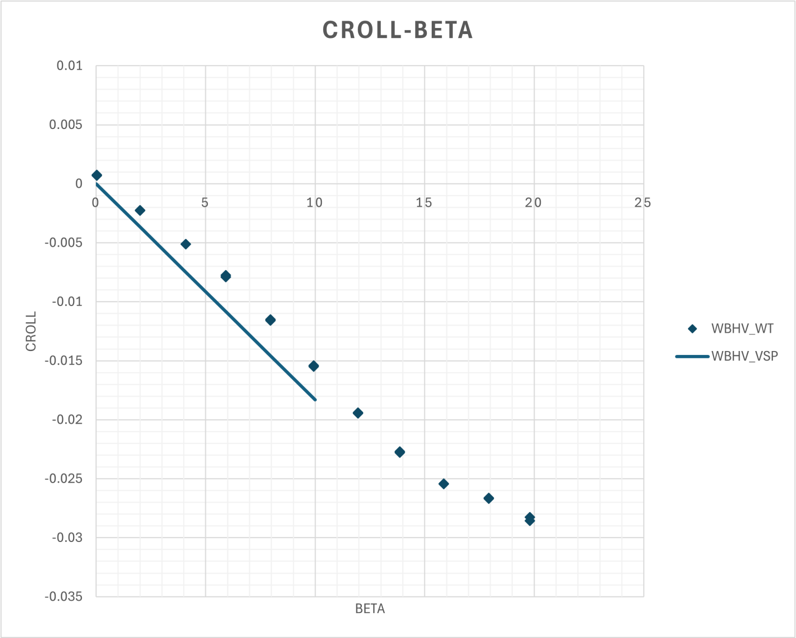

Figure 5.102: *Comparison between numerical and experimental data of the complete aircraft* $C_{\mathcal{L}} - \beta$ *curves*

The wing slightly reduces the stability, as previously explained, and VSP data is consistent with the behaviour observed in the wind tunnel. The prediction given by the solver is over-estimating both the lateral and directional stabilities.

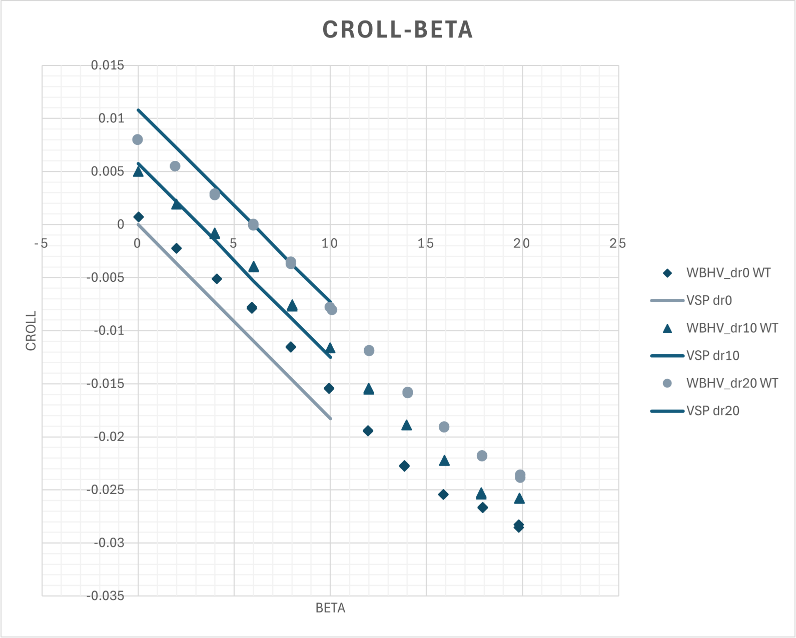

Figure 5.103: *Comparison between numerical and experimental data of the effect of the rudder on the* $C_{\mathcal{L}} - \beta$ *curves*

	$C_{\mathcal{L}_\beta}(1/deg)$ (1/deg)	$C_{\mathcal{L}_{\delta_r}}(1/deg)$
WBHV_dr0_WT	-0.0016	-
WBHV_dr0_VSP	0.0031	–
WBHV_dr10_WT	-0.0016	0.0004
WBHV_dr10_VSP	0.0034	0.0005
WBHV_dr20_WT	-0.0015	0.0004
WBHV_dr20_VSP	0.0035	0.0005

Table 5.23: *Comparison of the lateral stability between numerical and experimental data of the complete aircraft*

As shown by data including the rudder deflection, the previous trend is preserved. Furthermore the experimental control derivative is lower by 20% compared to the numerical one.

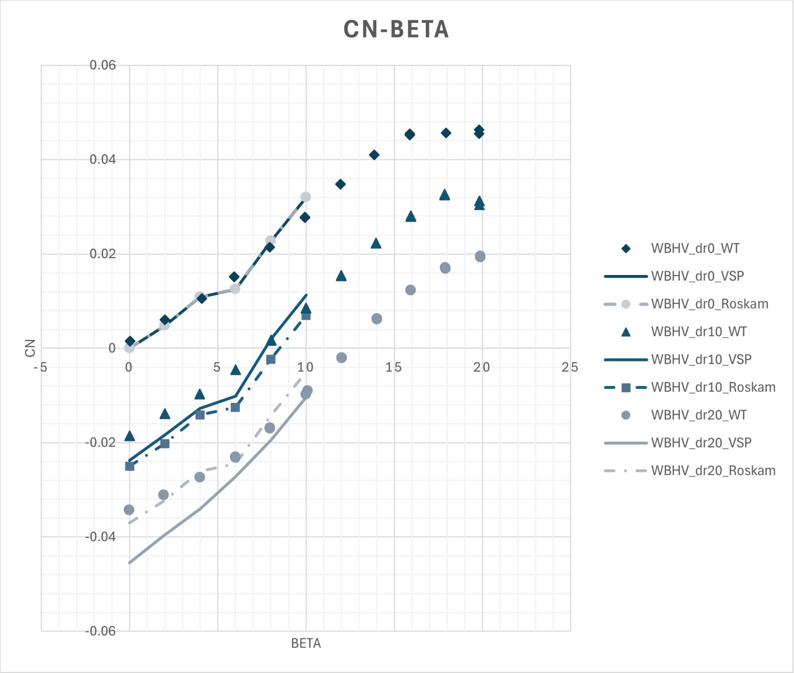

Figure 5.104: *Comparison between numerical and experimental data of the effect of the rudder on the $C_N - \beta$ curves*

	$C_{N_\beta}(1/deg)$	$C_{N_{\delta_r}}(1/deg)$
WBHV_dr0_WT	0.0026	-
WBHV_dr0_VSP	0.0031	–
WBHV_dr0_Roskam	0.0031	–
WBHV_dr10_WT	0.0027	−0.0020
WBHV_dr10_VSP	0.0034	−0.0024
WBHV_dr10_Roskam	0.0034	−0.0025
WBHV_dr20_WT	0.0023	−0.0018
WBHV_dr20_VSP	0.0035	−0.0023
WBHV_dr20_Roskam	0.0035	−0.0019

Table 5.24: *Comparison of the directional stability between numerical and experimental data of the complete aircraft*

If a comparison is made also considering the Roskam method, the control derivative appears to be over-estimated by the numerical methods, with the semi-empirical being more accurate than VSPAero with larger rudder deflections, even though this is the only condition in which one of the numerical methods gives a definitely closer prediction. As explained in the longitudinal comparison, the analyses were carried out with a full-scale model in real flight conditions, that is different Reynolds and Mach numbers. Given this and the inherent limitations of the numerical methods, having around 20% of variation between data can be considered sufficient for a preliminary prediction of stability, with fast and effective estimation of trends and expected results.

5.4 Reynolds effect and scaling

Reynolds number variations mainly affect the non-linear portion of the lift curve and the drag throughout the polar, as mentioned at the beginning of this chapter. The flow condition does not significantly impact longitudinal stability, which can therefore be easily estimated through wind tunnel testing, whereas directional parameters can show larger discrepancies compared to flight, particularly related to rudderlock [4], a condition in which a large β suddenly causes separation on the rudder and a strong suction on the low pressure side, leading to spontaneous rotation of the movable surface and unavailability of the directional control. During wind tunnel tests, the rudder appears to be less affected by this condition, whereas flight at the same sideslip angle can more easily lead to rudderlock. Lateral stability is usually well represented by tests, with small disagreement in control due to different wing structure and flexibility. The scaling is applied on the coefficients of the complete configuration, which is the most significant for the overall performance.

5.4.1 Maximum lift coefficient scaling

The effect of the flow regime is particularly relevant for the characteristics of the boundary layer, which impact the resistance to adverse pressure gradients. At lower Reynolds numbers the viscous region is thicker and the velocity profile has less energy, which increases displacement thickness and reduces effective camber since the boundary layer grows faster on the upper surface of the wing. This, paired with the stronger tendency to separate when facing positive pressure gradients, causes anticipation of stall and lowers $C_{L_{max}}$. A small reduction of C_{L_α} is to be expected due to the reduced camber at equal α, but it is considered negligible.

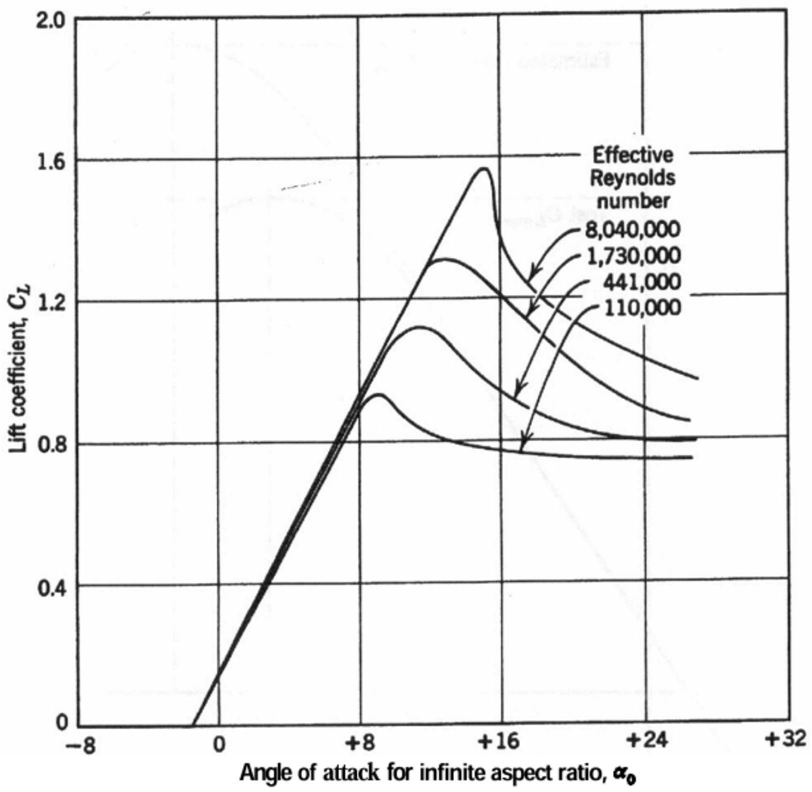

Figure 5.105: *Effect of the Reynolds number on the lift curve*

The procedure firstly requires the calculation of the Reynolds number of test and flight conditions, which are shown in Table 5.25.

	Test	**Flight**
h (m)	0	3000
ρ (kg/m^3)	1.225	0.9091
V (m/s)	35	98.58
L (m)	0.181	2.15
μ ($Pa\cdot s$)	$1.789 \cdot 10^{-5}$	$1.694 \cdot 10^{-5}$
a (m/s)	340.3	328.6
M	0.103	0.300
Re	433782.8	11385153.4

Table 5.25: *Comparison of test and flight parameters*

The maximum lift coefficient to scale has been extracted from the experimental curves. Knowing the wing geometry, the weights K_i associated with the airfoils of the root, kink and tip [3], were calculated and used to evaluate mean aerodynamic characteristics, particularly the leading edge sharpness parameter $\frac{\Delta y}{c}$, which is fundamental for the estimation of

---

[3] $K_i = \frac{2 \cdot S_i}{Sw}$, where S_i is the area influenced by the considered wing section

the maximum lift coefficient ratio between 3-D and 2-D, as well as the compressibility correction on the $C_{L_{max}}$.

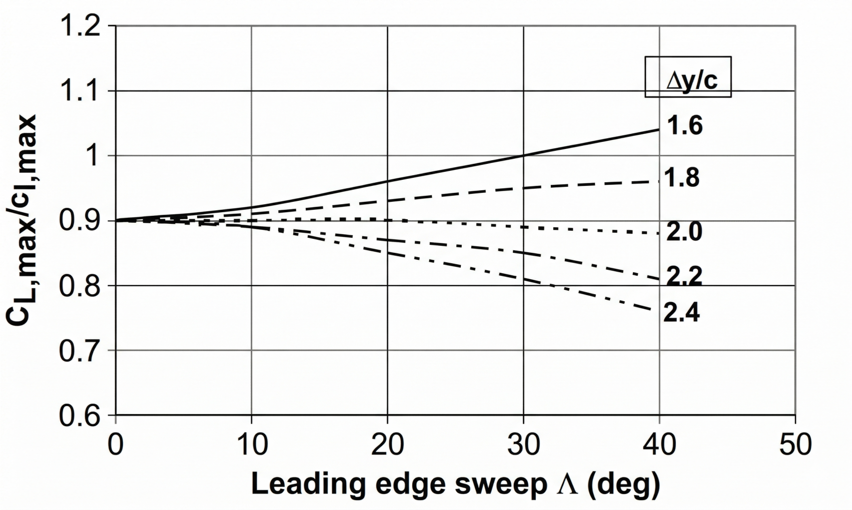

Figure 5.106: Lift coefficient ratio based on leading edge sharpness and wing sweep

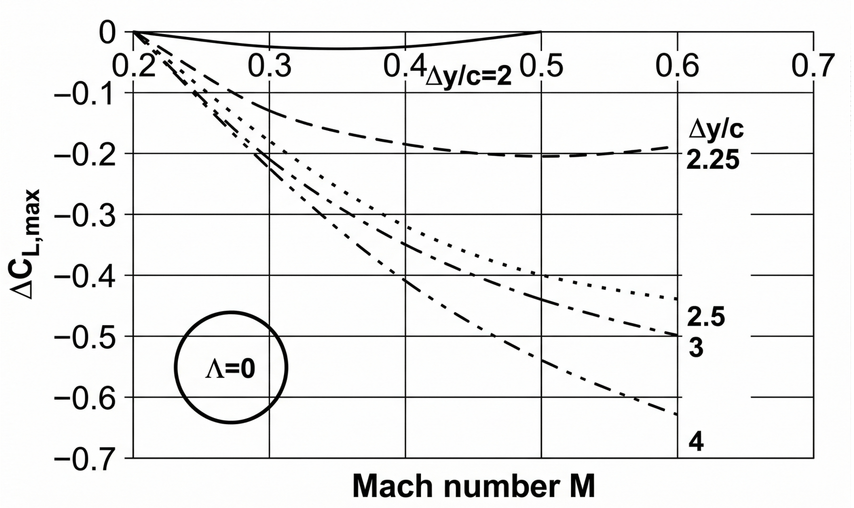

Figure 5.107: Lift coefficient correction based on Mach number

The semi-empirical calculation of the 2-D $C_{l_{max}}$ is:

$$C_{l_{max}} = \frac{C_{l_{max}}}{C_{L_{max}}}(C_{L_{max}} - \Delta C_{L_{max}}) \tag{5.6}$$

As the ΔRe and the airfoils used in the three sections are known[4], the effect on the $C_{l_{max}}$ due to Reynolds for each section was evaluated thanks to Tab. 5.26 and Fig. 5.108. The correction was then averaged using the same formula applied to evaluate $\frac{\Delta y}{c}$, that is:

$$\bar{x} = x_r \cdot K_a + x_k \cdot K_b + x_t \cdot K_c \tag{5.7}$$

---

[4] NACA 43018 for root and kink sections, NACA 43015 for the tip

Airfoil NACA	Stall Type	Airfoil NACA	Stall Type
0006	A	4412	C_4
0009	B_0	4415	D_4
0012	C_0	4418	E_4
0015	D_0	4421	E_5
0018	E_0	23006	A
0021	E_1	23009	C_2
0025	E_2	23012	D_2
0030	—	23015	D_2
2212	C_3	23018	E_2
2409	B_2	23021	E_2
2412	C_2	43012	D_4
2415	D_2	**43015**	D_4
2418	E_2	**43018**	E_4
4406	A_3	63012	D_6
4409	B_4	63018	E_7

Table 5.26: NACA Airfoil stall types

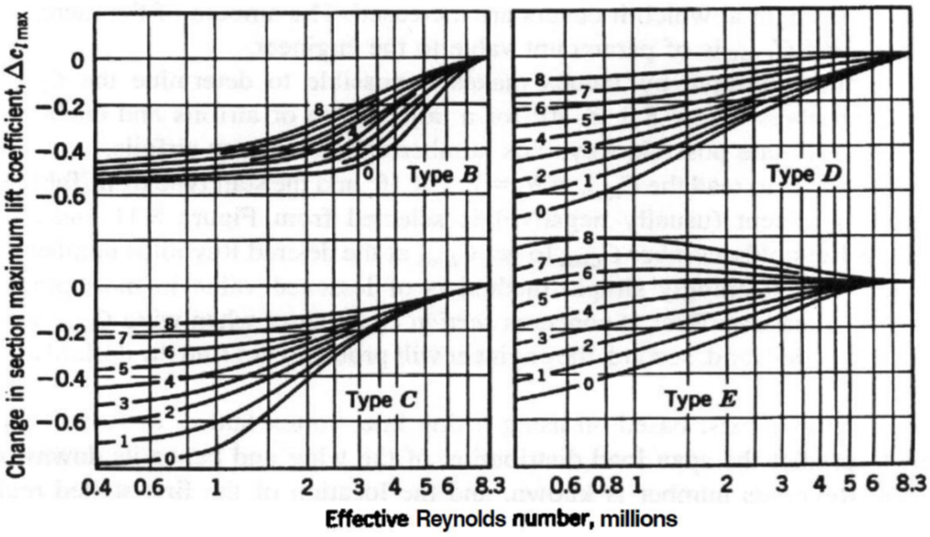

Figure 5.108: $C_{l_{max}}$ corrections based on Reynolds number and stall type

Once the 2-D maximum lift coefficient at high Reynolds had been calculated, the 3-D value was obtained reversing Eq.5.6. As suggested by [4], the curve in the non-linear range has been incremented by the difference between scaled and unscaled 3-D $C_{L_{max}}$ values and shifted to respect the tangency constraint with the linear section, whereas the latter has been extended to the new minimum non-linear value of the lift coefficient.

Ka	0.189	$\frac{C_{Lmax}}{C_{lmax}}$	0.9
Kb	0.557	$\Delta C_{L_{max_M}}$	−0.085
Kc	0.254	$\Delta C_{l_{max}}\vert_r$	0.19
$\frac{\Delta y}{c}\vert_r$	1.99	$\Delta C_{l_{max}}\vert_k$	0.19
$\frac{\Delta y}{c}\vert_k$	1.99	$\Delta C_{l_{max}}\vert_t$	0.38
$\frac{\Delta y}{c}\vert_t$	2.37	$\Delta C_{l_{max}}$	0.24
$\frac{\Delta y}{c}$	2.09		

Table 5.27: *Parameters for the $C_{L_{max}}$ correction*

The whole correction process has led to the values shown in Tab. 5.28 for the three flight conditions, from which the curves in Fig. 5.109 have been reconstructed.

	Cruise	Take-off	Landing
$C_{L_{max}}$ (Low Re)	1.60	2.07	2.23
$C_{l_{max}}$ (Low Re)	1.87	2.39	2.57
$C_{l_{max}}$ (High Re)	2.11	2.63	2.81
$C_{L_{max}}$ (High Re)	1.81	2.28	2.44

Table 5.28: *Correction of the $C_{L_{max}}$*

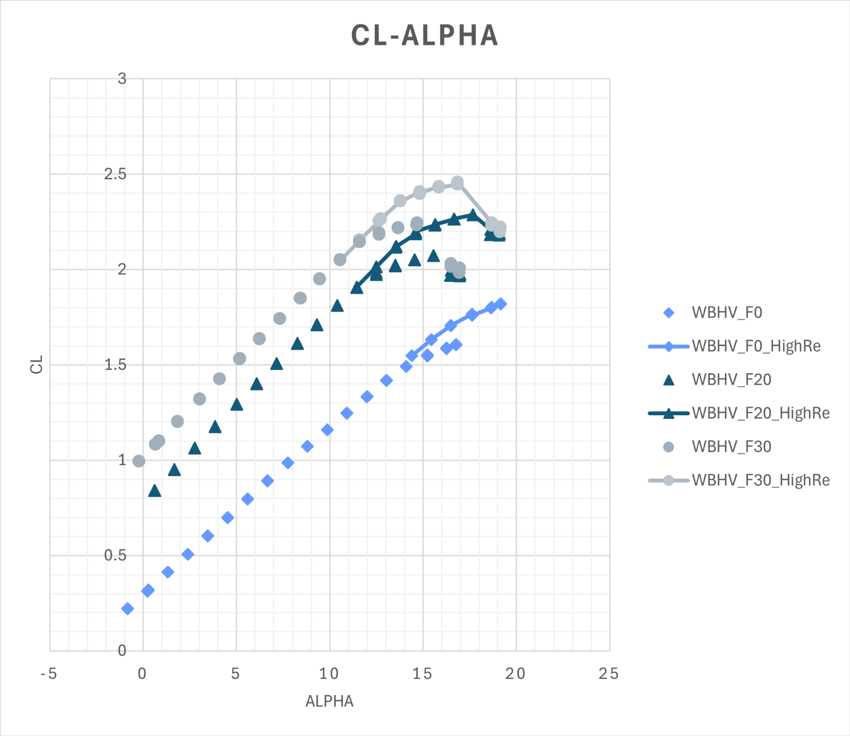

Figure 5.109: *Comparison of the lift curves between the test and flight Reynolds*

This method introduces some approximations, such as the shift of the non-linear section, which assumes that the stall happens the same way in both flow conditions, or the unchanging C_{L_α}. Furthermore, the correction is carried out on the airfoil and required the usage of a semi-empirical method to go back to the wing. Nevertheless, it allows to extract data which are closer to the real flight condition compared to the uncorrected ones, with an expected increase in maximum lift of 13.4% in cruise, 10.4% in take-off and 9.6% in landing configuration.

5.4.2 *Drag scaling*

Drag has been scaled for each flap configuration starting from the polar and removing the induced drag $\frac{C_L^2}{\pi \cdot AR}$. The C_{D_0} curve has been interpolated and extended to the $C_{L_{max}}$ at the flight Reynolds, using a sixth degree polynomial.

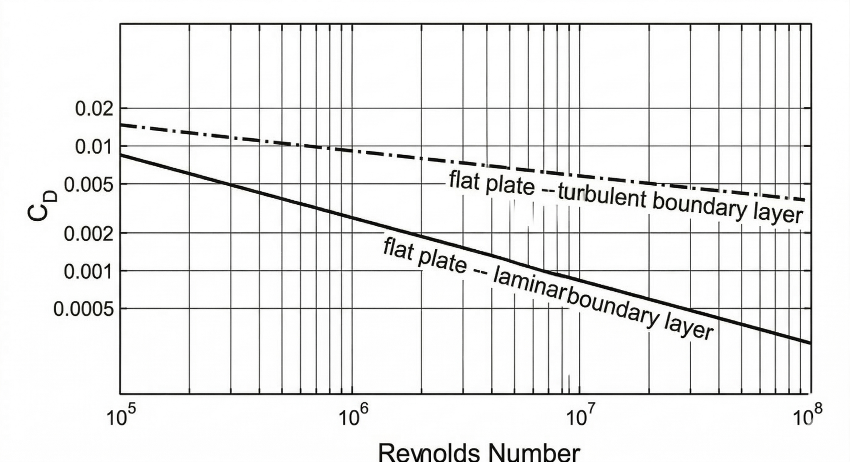

Figure 5.110: *Drag coefficient variation with Reynolds number on a flat plate*

The extrapolation allowed to obtain the complete curve, which has been successively scaled to the correct Reynolds number by subtracting the difference between the drag coefficient at test and flight conditions. In particular, for each flap deflection, the C_{D_0} has been divided by the ratio $\frac{S_{wet}}{S}$ to obtain the equivalent skin friction coefficient C_{f_e}. The C_f at low Reynolds has been extracted from Fig.5.110, considering that for a flat plate, $C_f = 0.5 \cdot C_D$. Then the scaling factor $\frac{C_{fe}}{C_f}$ was used to turn the skin friction coefficient relative to the high Reynolds to the updated C_{f_e}, which led to the scaled C_{D_0}. After the calculation of the induced drag in the extended range of lift coefficients, the complete scaled polar was reconstructed by adding parasite and induced contributions. The values for the three conditions are presented below.

	WBHV_F0	**WBHV_F20**	**WBHV_F30**
C_{D_0} **(Low Reynolds)**	0.0301	0.0538	0.0731
C_{f_e} **(Low Reynolds)**	0.00713	0.01275	0.01732
C_f **(Low Reynolds)**	0.005	0.005	0.005
$\frac{C_{f_e}}{C_f}$	1.43	2.55	3.46
C_f **(High Reynolds)**	0.003	0.003	0.003
C_{f_e} **(High Reynolds)**	0.00428	0.00765	0.01039
C_{D_0} **(High Reynolds)**	0.0181	0.0323	0.0439

Table 5.29: *Reference values for C_{D_0} scaling*

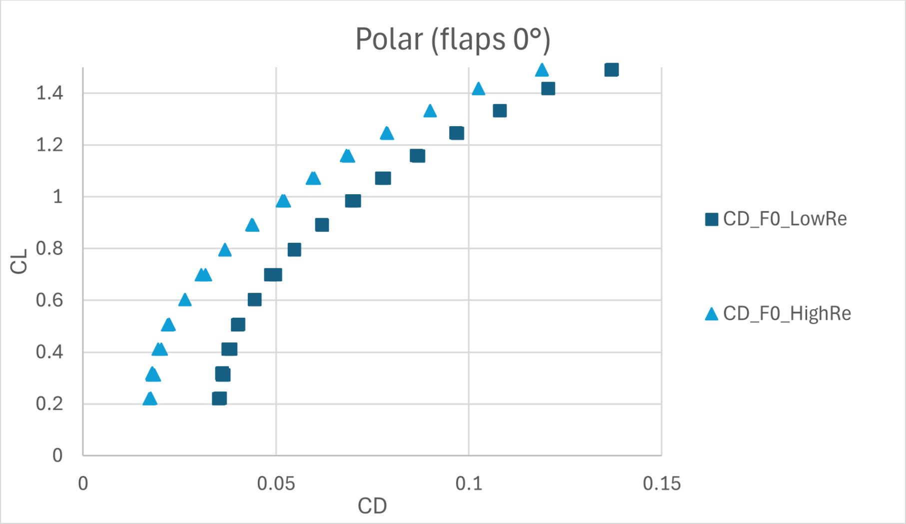

Figure 5.111: *Baseline and scaled polar curves in cruise condition*

Drag correction requires data interpolation and extrapolation based on the approximated $C_{L_{max}}$ and additionally uses flat plate scaling, whereas a more accurate approach would include a database for the variation of C_{D_0} with Reynolds number based on the specific model, to extrapolate with more accuracy. Just like the lift, this scaling is of utmost importance to the engineers as it provides a reference drag value for performance and fuel consumption estimation.

The variation between scaled and unscaled values, computed as an average of the ones calculated at each point of the baseline curve, is -12.0% in cruise, -6.0% in take-off and -4.2% in landing, since parasite drag progressively gives a less relevant contribution compared to pressure drag as the flaps are deflected.

Chapter 6

Conclusions and future perspectives

6.1 Summary of findings

The objective of this work was to carry out an experimental wind tunnel campaign on an innovative multi-role seaplane, aimed to analyze the aerodynamic performance of the aircraft, particularly the longitudinal and lateral-directional stability characteristics. Furthermore, interactions between the various components were evaluated to understand the effectiveness of the design choices and isolate their contribution to the aircraft stability, analyzing different configurations and visualizing flow behaviour, while changing flaps, elevator, and rudder deflections. The required corrections to apply on data coming from the acquisition system were carefully calculated, considering both wind tunnel and weight tare effects. A comprehensive database has been built to quantify derivatives and coefficients, related to both longitudinal and lateral-directional performances, as well as downwash determination. The lifting capabilities are coherent with the preliminary design estimations. Comparison with the numerical methods shows negligible differences (6%) on the C_{L_α}, while the evaluation of $C\mathcal{M}_\alpha$ shows a 30% increase in longitudinal stability in the wind tunnel. The stability and static margin are adequate for the considered aircraft during flight operations, with effective longitudinal control up until stall and with minimal loss in maximum lift with high deflections of the elevator. The $C_{L_{max}}$ increase due to flaps is in accordance with the preliminary design assumptions, with a gain of 30% in take-off and 40% during landing compared to cruise conditions. Directional stability is sufficient for this type of aircraft during flight, and lateral stability is ensured, in accordance with requirements. The rudder is effectively capable of trimming the aircraft however, given the operative scenarios this type of seaplane would be involved in, including both passenger transport and emergency response, and considering the safety and reliability required for certification, an increase in the authority of the directional control could be considered during design refinement. The horizontal tail, thanks to the endplate effect, gives a beneficial contribution to directional stability, increasing the latter by 10% as indicated in Tab. 5.15.

As shown by flow visualizations during cruise, landing, and take-off, flow reversal begins at the root of the wing and separation does not affect the wingtips, ensuring ailerons effectiveness at low speeds and safe lateral control. Longitudinal control is granted as well, with no deep stall phenomenon highlighted by visualizations and $C_{\mathcal{M}}$ curves.

6.2 Limitations of the work

Even if wind tunnel tests are a reliable method to evaluate aircraft aerodynamics, lacking of the approximations applied by numerical analyses and simulations, they have their inherent limitations.

As already mentioned in previous chapters, the main drawback is represented by the difficulty in matching the flight non-dimensional parameters such as Reynolds and Mach numbers. This leads to a more complex correlation of the results between the test and flight conditions, introducing approximations through the scaling process. Having the model inside a test chamber, surrounded by walls, also results in the need of boundary corrections, which lead to unavoidable errors in output data. Furthermore, turbulence intensity inside the wind tunnel is typically low to allow for the extraction of the coefficients of interest in almost stationary and replicable conditions, but in the operative scenarios its value can differ from tests, leading to different instantaneous values of the coefficients. Moreover, separation is a highly unsteady phenomenon, hence quantitative data should be considered as trends and not exact in-flight values. Reliability increases in the linear section of the curves, but data are always sampled discreetly, whereas flow evolves continuously around the aircraft.

The model has a different internal structure compared to the real aircraft, hence structural and aero-elastic phenomena have not been considered during tests, leading to different behaviours. Anyway, this is normal, as aero-elastic studies are more advanced analyses, which are eventually linked to the aerodynamic development. The numerical analyses which were carried out implement semi-empirical (Roskam) or inviscid (VSPAero) methods, so difference between experimental and computational results was widely expected, even though correlation is consistent considering their limitations and the purpose of a preliminary design, paired with their competitive speed in delivering results. Flow visualization was carried out with wool tufts, which directly impact the flow field, as tufts modify the displacement thickness and can cause early separation in regions with already strongly adverse pressure gradients. Nevertheless, tufts are a fast, straightforward and cost-effective method to gain a qualitative insight into the stream behaviour throughout the model. All this considered, wind tunnel tests remain a reliable, consistent, and effective method for aerodynamic investigation, offering a fast, versatile, and cost-effective solution to bridge the gap between simulations and full-scale flight tests.

Lastly, the aerodynamic analysis only represents a part of a seaplane operative envelope, considering that take-off, landing and scooping maneuvers imply aircraft-water interaction, hence a hydrodynamic investigation is necessary to completely characterize the flyingboat.

6.3 Future developments

Starting from the previous consideration, further development of the seaplane could involve hydrodynamic performance evaluation as well. In hydrodynamic tests, care should be taken regarding the Froude number, which strongly affects drag generation related to waves in water operations. Hydrodynamic behaviour investigation could be useful for evaluating the addition of other components, such as lateral spray strips, to avoid water ingestion by the engines and spray impact on tail and control surfaces, which could be detrimental for seaplane performances. Furthermore, both aerodynamic and hydrodynamic tests should be carried out with the inclusion of the propulsive system, to study the interaction between the slipstream coming from propellers and lifting surfaces as well as disturbances due to nacelles integration on the wing. Furthermore, ailerons effect on aerodynamics should be examined, in order to characterize their impact on lateral and directional control and equilibrium. To move forward in the aircraft development process, advanced computational simulations, such as RANS or other CFD methods, could be carried out, allowing an even more accurate prediction of the flow behaviour compared to preliminary numerical estimations.

Bibliography

[1] Ira H. Abbott and Albert E. Von Doenhoff. *Theory of Wing Sections, Including a Summary of Airfoil Data*. Dover Pubblications, 1959.

[2] John D. Anderson. *Fundamentals of Aerodynamics*. McGraw-Hill Education, 6th edition, 2016.

[3] ATI Industrial Automation. F/T Sensor: delta. `https://www.ati-ia.com/products/ft/ft_models.aspx?id=delta`. Accessed: 2026-02-04.

[4] Jewel B. Barlow, William H. Rae Jr., and Alan Pope. *Low-speed wind tunnel testing*. John Wiley & Sons Inc., 3rd edition, 1999.

[5] J. J. Bertin and R. M. Cummings. *Aerodynamics for engineers*. Pearson, 6th edition, 2013.

[6] Alan Canamar. Seaplane conceptual design and sizing. Master's thesis, University of Glasgow, 2012.

[7] Bruno Chanetz, Jean Délery, Patrick Gilliéron, Patrick Gnemmi, Erwin R. Gowree, and Philippe Perrier. *Experimental Aerodynamics: An Introductory Guide*. Springer, 2020.

[8] S. H. Chicken. *Conceptual Design Methodologies for Waterborne and Amphibious Aircraft*. Phd thesis, Cranfield University, United Kingdom, 1999.

[9] DAF Group. Daf main subsonic wind tunnel. `https://www.dii.unina.it/source/ricerca/lab/ingegneria-aerospaziale`, 2025. Accessed: 2025-07-24.

[10] Mark Drela. *Flight vehicle aerodynamics*. MIT Press, 2014.

[11] S. P. Govinda Raju. Role of wind tunnels in aircraft design. *Resonance*, 8(1):72–76, 2003.

[12] J.Roskam. *Airplane design*. DARcorporation, 1997.

[13] J. Katz and A. Plotkin. *Low Speed Aerodynamics*. Cambridge University Press, 2001.

[14] A. P. Sage M. Jamshidi. *System of systems engineering*. Wiley, 2011.

[15] D. McLean. *Understanding aerodynamics: arguing from the real physics*. John Wiley & Sons, 2012.

[16] Ministero dell'Interno. Canadair italiano dei vigili del fuoco vola in portogallo. `https://www.interno.gov.it/it/notizie/canadair-italiano-dei-vigili-fuoco-vola-portogallo`. Accessed: 2026-03-02.

[17] NASA. Openvsp and vspaero basics. `https://www.nasa.gov/reference/openvsp-vspaero-basics/`. Accessed:2026-03-12.

[18] NASA. Wing geometry definitions. `https://www.grc.nasa.gov/www/k-12/airplane/geom.html`, 2023. Accessed: 2024-01-01.

[19] Vincenzo Nugnes, Carmine Varriale, Patrick Ratei, Prajwal Shiva Prakasha, and Björn Nagel. A system of systems aircraft design framework: Demonstration using a seaplane transport network in the greek islands. In *Proceedings of the 34th Congress of the International Council of the Aeronautical Sciences (ICAS)*, Florence, Italy, September 2024.

[20] P. R. Owen and L. Klanfer. On the laminar boundary-layer separation from the leading edge of a thin aerofoil. Current Paper ARC CP-220, Aeronautical Research Council, 1953.

[21] Alan Pope. *Basic wing and airfoil theory*. McGraw-Hill, 1958.

[22] Prajwal Shiva Prakasha, Nabih Naeem, Kristian Amadori, Giuseppa Donelli, Jasamin Akbari, Fabrizio Nicolosi, Ludvig Knöös Franzén, Manuela Ruocco, Thierry Lefebvre, and Björn Nagel. Colossus eu project – collaborative sos exploration of aviation products, services and business models: Overview and approach. In *Proceedings of the 34th Congress of the International Council of the Aeronautical Sciences (ICAS)*, Florence, Italy, September 2024.

[23] H. Schlichting and K. Gersten. *Boundary-layer theory*. Springer, 9th edition, 2017.

[24] Pasquale M. Sforza. *Commercial Airplane Design Principles*. Elsevier, 2014.

[25] M. Tuccillo. *AMethodology for the Architecture Exploration and Optimization of Next GenerationMulti-Role Seaplanes*. Phd thesis, University of Naples Federico II, 2025.

[26] R. Vos and S. Farokhi. *Introduction to transonic aerodynamics*. Springer Science & Business Media, 2015.